Tuning Superconductivity and Competing Phases in an Iron-based Superconductor with Uniaxial Stress

Paul Malinowski

A dissertation

submitted in partial fulfillment of the

requirements for the degree of

Doctor of Philosophy

University of Washington

2022

Reading Committee:

Jiun-Haw Chu, Chair

David Cobden

Boris Spivak

Program Authorized to Offer Degree:

Physics

University of Washington

Abstract

Tuning Superconductivity and Competing Phases in an Iron-based Superconductor with Uniaxial Stress

Paul Malinowski

Chair of the Supervisory Committee:
Jiun-Haw Chu
Department of Physics

Unconventional superconductors exhibit strong electronic correlations, quantum criticality, and numerous broken-symmetry collectively ordered phases involving a complex combination of charge, spin, and lattice degrees of freedom that manifest in an intertwined phenomenology where different phases and their fluctuations both compete and cooperate with each other. Understanding the role of the competing phases and quantum critical phenomena in the formation of superconductivity is a central question in condensed matter physics.

In this thesis, I investigate the effect of uniaxial stress inducing strains in different symmetry channels on an unconventional Fe-based superconductor $Ba(Fe_{1-x}Co_x)_2As_2$. I will first show that anisotropic strain enhancing nematic order is extremely efficient in suppressing the high-temperature superconductivity, which provides evidence for the role of nematic fluctuations in the superconducting pairing. I will then show that non-symmetry breaking strain and chemical composition are remarkably equivalent tuning parameters for superconductivity, which strongly favors the scenario in which the formation of superconductivity is driven by a quantum critical point. Finally, I will present Hall effect measurements revealing a new large and strongly temperature dependent elastoresistivity coefficient which reflects an extreme sensitivity of the conduction electrons to a strain-induced enhancement of spin fluctuations.

Acknowledgements

My route to and through the PhD has been both challenging and extremely rewarding, and I have countless people to thank for helping me through. My path through physics was a winding one, and it took me awhile to land in experimental condensed matter physics. As an undergrad at UCSD, I was very focused on mathematics and the theoretical side of physics. However, near the end of college I ended up working in the lab of Eva-Maria Schoetz Collins, a biophysics lab focused on studying regenerative animals. There I studied planarian flatworms and helped develop a biomechanical model of how they perform fission, an asexual reproductive mode where the worms rip themselves into pieces which subsequently regenerate into new worms. I am very grateful for Eva's deep passion for science and the care she demonstrated for those working for her. She gave me my first exposure to how science is done in the real world, how to think about research problems, and how to write and present effectively. Through her guidance, I was able to publish as co-first author in *PNAS*, launching my career as a "real scientist." Thank you Eva and I hope you are doing well at your new lab.

Once I was accepted to UW for graduate school, I still had my mind set on being a theoretical physicist. To that end I skipped the core quantum mechanics courses, took all the quantum field theory courses, joined the particle theory journal club, and even did a reading course with Andreas Karch learning about conformal field theories. However, I began to become disillusioned with the prospects of a career in theoretical physics (this is in spite of the fact that Andreas is one of the best teachers I have ever had). Around that time, somewhat serendipitously, I met Jiun-Haw Chu at one of the department's "Friday Flings", a social where graduate students, postdocs, and faculty could drink, snack, and talk for a few hours. Jiun-Haw and I had a conversation and talked about superconductivity and other things, and he came across to me as an amicable and extremely intelligent person. A week or two later I got an email from him asking if I wanted to try out working in his lab, and I decided I should try it. Here I am 5 years later, and I don't regret that decision.

I am extremely grateful to Jiun-Haw for turning me to condensed matter experiment, and in the process likely changing my entire career path and life. Jiun-Haw has been a great boss and mentor, both scientifically and otherwise. He is patient and kind, and I cannot think of a single time where I harbored any negative feelings towards him. I have always been impressed by his

breadth of condensed matter physics knowledge, not only in the experimental arena but also in the theoretical aspects. Jiun-Haw has taught me how to be a good experimentalist and how to think about the big picture and decide which research questions to follow, as well as enumerable concepts in condensed matter. I am thankful for the opportunities he has given me to learn how to collaborate with others, how to be a mentor, how to write interesting papers, and how to give great presentations. He has also shown me that passion for science and physics can stay vibrant throughout your career. For all that, I count myself fortunate to have been able to work with him and I hope to be able to collaborate with him even after I leave.

The next group of people I cannot imagine having completed this PhD without are my lab mates, who are the people I have spent the most time throughout my time in Seattle: Joshua Mutch, Shua Sanchez, Qianni Jiang, Yue Shi, Xuetao Ma, Jonathon DeStefano, Zhaoyu Liu, Zhong Lin, Elliott Rosenberg, Joss Aryes-Sims, Dan Sokratov, Tiema Qian, Winnie Wang, and Ilham Zaky Wilson. This group of people were a great source of true friendships and made being in the lab fun and enjoyable. I have to give special thanks to Josh, Shua, and Qianni; we were the "original" group of Jiun-Haw's first graduate students and I have many good memories from the early days when the lab was still taking the form it is in now. Qianni is one of the smartest and hardworking people I have ever met, and her and I spent a lot of time together on trips to the High Magnetic Field Lab (Tallahassee and Los Alamos). We always had a lot of fun working and talking together and I really cherish those experiences. Josh and I shared a lot of beers and conversation together and I always admired his consistent work ethic. I also have to thank him for spending so much time and effort developing our Lab View sequencer that we still use to run our cryostats and instruments. Shua and I spent a lot of great times together, both in a scientific setting (such as very, very long nights at the Advanced Photon Source at Argonne National Labs) and also going to see local music in Seattle. My conversations with Shua about physics were always fun and illuminating, and I admire him for his passion for both physics, as well as politics and social issues. Everyone in the lab has impressed me with their intelligence and dedication to science and I cannot wait to see all the amazing things they all do in the future.

A number of others in the Physics Department at UW have been extremely helpful and supportive throughout my time here. Catherine Provost has shown me consistent support and kindness since my very first day, and I truly appreciate her efforts to improve the experiences of

the graduate students in the department. Huimei Wu was always a cheerful person to interact with and assisted in numerous bookings of lodging and flights for conference and national lab visits (she deserves special praise in light of the fact that many of these were requested at the unreasonably last minute) and I really appreciate her assistance. Alexis Hall in the front office was also always so helpful in all kinds of administrative issues and I thank her as well. I would also like to thank the members of my committee (David Cobden, Ting Cao, Boris Spivak, and Stephen Sharpe) for agreeing to be a part of my PhD experience. I took many classes over the years here at UW, and I would like to give a special thanks to Andreas Karch (quantum field theory), Stephen Sharpe (group theory), and Matthew Yankowitz (quantum hall physics) who were really fantastic teachers and taught in a way that allowed me to truly understand the subject matter. I am also grateful to Xiaodong Xu for always encouraging and supporting me and for being a great source of stimulating conversations.

I've been fortunate enough to be able to visit a number of national laboratories to do experiments, and those experiences really strengthened my abilities as an experimentalist. I am thankful to David Graf and Arkady Shekhter at the High Field Lab in Tallahassee, Johanna Palmstrom and John Singleton at the High Field Lab in Los Alamos, and Phil Ryan and Jong-Woo Kim at the Advanced Photon Source in Argonne National Labs for helping me with countless experiments and helping me to become a better scientist.

A number of funding sources have made it possible to be fully funded through research throughout my PhD, and I am grateful for that support: Moore Foundation, NSF MRSEC, Air Force Office of Scientific Research, and DOE Pro-QM EFRC.

As is typical for a graduate student, I have had many roommates over the years, and they all provided a much-needed source of support and friendship at home. When I first moved to Seattle, I lived with Erica Yuen, Lexi Vasbinder, and Alessandro Slamitz who were really my first friends in Seattle and made the transition of living in a brand-new city much easier and more enjoyable. Most of my PhD, I lived with other physics graduate students: Mike Smith, Tyler Blanton, Sean Gasiorowski, and Nick Ruof. These guys were tons of fun to live with and I have so many hilarious memories from our house in Fremont. I also lived briefly with Kevin Zhao, and that luckily turned into a great friendship. I am thankful to Kevin for introducing me to the pleasures of fancy cocktails and for all of the great obscure philosophical debates (e.g., Are

numbers real? Do aliens use math?) in the dark corners of bars. The final years of my PhD I have lived with David Bell, who has been a great roommate and friend. I am thankful to David for encouraging and motivating my new-found love for long distance running.

I am very thankful for my cohort of graduate students in the physics department, who were some of my first friends in Seattle and helped ease the pain of homework sets and exams in the first two years. I am also thankful to all of the friends I have made in Seattle who have made Seattle a true home and a fun place to live. Special shoutout to Hannah Binney, Amanda Manaster, Sebastian Alvis, Sam Kowash, and Sean Phillips.

I am lucky to have a big family, and they have all given me love and support throughout my PhD and life. I am eternally grateful to my parents (Tom, Patty, and Cathryn) for raising me and providing a warm and welcoming place to go home to. I could not imagine better parents, and I love you all so much. I am grateful to my 6 siblings (Kate, Nate, Crissy, Nicole, Alyssa, and Lauren) for being amazing people and giving me so much companionship throughout the years. I like to think that having such a big family taught me valuable lessons about collaboration and working in a group that serve me well in the scientific environment. Special thanks to Kate and Nicole, who have made me an uncle and given me three beautiful nieces and nephews, Jack, Penelope, and Leo. I love these tiny people so much and can't wait to see what life has in store for them.

Finally, I would like to acknowledge my partner, Lauren Pittis, with whom I have been with for almost my entire PhD. Lauren is one of the kindest, sweetest, most caring people I have ever met, and I am so lucky to have them in my life. They have provided me with so much love and support over the past 5 years, and I truly could not have made it through without them. Thank you Lauren for letting me forget about physics while we go on picnics, go to the zoo or the aquarium, or just hang out and do nothing. Thank you for being so understanding when I have been stressed or wasn't able to spend as much time together as we would have liked. I truly appreciate you more than you will ever know and am so grateful to have met you and to have been on the receiving end of your big heart and infectious kindness.

Dedication

To my amazing niece and nephews

Jack, Penelope, and Leo

Contents

List of Figures

List of Tables

1. Introduction

The past century has witnessed the ascendancy of the field of quantum materials[1–3], wherein quantum mechanical behavior of the constituent particles leads to fascinating collective phenomena. In spite of the fact that at the fundamental level the behaviors of these materials are all governed by the same many-body Schrödinger equation, the presence of a large number of particles (~10^{23}) leads to a situation where "more is different"[4]; the solid state environment with interacting degrees of freedom is capable of giving rise to a vast and complex array of phases such as magnetism, density waves, non-trivial topological states, spin liquids, Mott insulators, superconductivity, and more. Studying these compounds allows us to understand the interplay and consequences of broken symmetry, strong correlations, quantum entanglement, and classical and quantum fluctuations. Our understanding of these phases has not only allowed rapid technological progress by giving us the ability to harness and exploit their quantum properties, but also provides a rich test bed for uncovering new phases of matter, testing and developing our theoretical descriptions, and driving the development of novel experimental techniques.

One of the most intriguing aspects of these materials is the fact that often more than one of these collective phases is present and intertwined with each other. Unconventional superconductors[5–7] are perhaps the best example of this, with charge, spin, and lattice degrees of freedom strongly coupled. In addition to (often high-temperature) superconductivity, the phase diagrams of most unconventional superconductors host broken-symmetry states driven by correlations of the spin and charge degrees of freedom. Rather than acting as impediments or passive observers to the superconductivity, it has become clear that these proximate phases are intimately connected and in fact necessary for high-temperature superconductivity[8]. Furthermore, even the disordered normal state cannot be understood in terms of standard paradigms such as the weakly interacting Fermi liquid, but instead is deeply influenced by the strongly fluctuating remnants of the anisotropic ordered states. This includes both classical thermal fluctuations as well as quantum fluctuations emanating from quantum critical points that are ubiquitous in these materials. This leads to a still poorly-understood normal state exhibiting anomalous "strange metal" behavior[9–11] where the standard quasiparticle description of solids seems to break down. It is out of this enigmatic normal state that unconventional high-

temperature superconductivity emerges. We are presented with a system exhibiting "ineluctable complexity"[12]; to fully understand the superconducting state, we must elucidate the complex interactions and relationships between the proximate ordered phases and their fluctuations, quantum criticality, coupling to the conduction electrons, and ultimately the superconducting pairing mechanism.

The Fe-based superconductors are one class of unconventional superconductors that have proven to be a rich environment in which to probe these issues. In addition to high-temperature superconductivity, these compounds host both antiferromagnetism as well as an electronically driven rotational symmetry breaking nematic phase. In contrast to the cuprate family of unconventional superconductors, these proximate ordered phases are relatively well understood in terms of their basic identity and symmetry, which may make them a more ideal system for understanding the central issues discussed above. As an experimentalist, a powerful way to learn about materials and the physics within them is via external tuning parameters which allow one to couple to the ordered phases and their fluctuations. In this thesis, I will follow this conceptual framework using externally applied lattice deformations in the form of stresses and strains as tuning parameters in order to further understand the relationships between magnetic and electronic nematic order, quantum criticality, and superconductivity.

In this introduction, I begin with a brief history to put the Fe-based and other unconventional superconductors in a broader context. Then I outline the relevant background and existing literature on the Fe-based superconductors, focusing on $Ba(Fe_{1-x}Co_x)_2As_2$. A number of literature review articles have informed this section[13–16] as well as general reference materials on superconductivity[17,18]. I will also outline some general considerations regarding stresses and strains as experimental tuning parameters. Finally, I will motivate and outline the measurements and conclusions comprising this thesis.

1.1 (Un)conventional Superconductivity

Superconductivity was first observed experimentally in 1911 (Figure 1.1) by Heike Kamerlingh Onnes in a sample of mercury at 4K, enabled by his recent success in liquifying helium. The phenomenology of this superconducting state is characterized by three main experimental observations below the critical temperature T_c: vanishing of electrical resistance, expulsion of

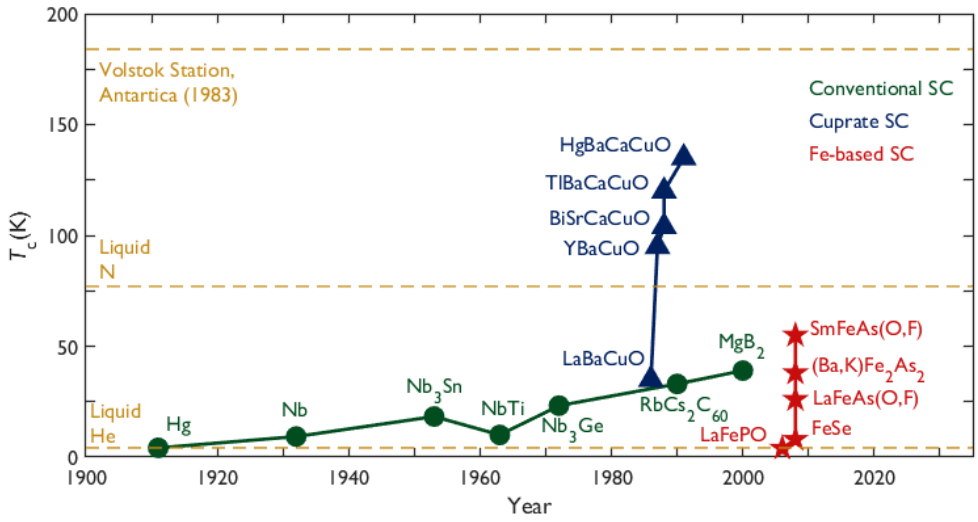

Figure 1.1. Superconducting T_c versus time for various superconductors[19]. Conventional BCS superconductors are shown in green, cuprate superconductors in blue, and Fe-based superconductors in red.

internal magnetic fields, and development of an energy gap for quasiparticle excitations. In the following years, many more elemental metals as well as intermetallic compounds were found to also exhibit superconductivity, all exhibiting a consistent experimental phenomenology. However, for many decades an explanatory theory was lacking.

This changed in the 1950's with the development of two paradigm-shifting theoretical ideas. The first was due to Landau and Ginzburg[20], following Landau's more general theory of continuous phase transitions, in which they laid out a phenomenological mean field theory describing the behavior of a symmetry-breaking superconducting order parameter ψ which measures the density of superconducting electrons. In this theory, the free energy is expanded in powers of the order parameter:

$$F = F_0 + a(T - T_c)|\psi|^2 + b|\psi|^4 + \frac{1}{2m^*}\left|\left(\frac{\hbar}{i}\nabla - \frac{e^*}{c}\vec{A}\right)\psi\right|^2 + \frac{h^2}{8\pi} \quad (1.1)$$

Here T_c is the superconducting critical temperature, ∇ and A are the gradient operator and vector potential respectively, and h is the magnetic field. This model is extremely useful for studying the macroscopic properties of superconductors and cases where the order parameter is spatially inhomogeneous, such as a type 2 superconductor in a magnetic field where vortices are present. Then in 1957, Bardeen, Cooper, Schrieffer detailed a comprehensive microscopic theory[21] explaining the mechanism driving superconductivity and deriving the macroscopic experimental consequences. Together these two theories were able to a large extent satisfactorily

account for the properties of all known superconductors up to that time. Gor'kov later showed[22] that these two theories were in fact equivalent by demonstrating that the Ginzburg-Landau formulation was derivable from the microscopic BCS theory as a limiting case where the temperature is near T_c and the spatial variations are slowly varying. This derivation also demonstrated that the order parameter ψ could be identified with the BCS gap function Δ which is described below.

The BCS theory explains that superconductivity is a collective phenomenon in which electrons in the presence of an effective attractive interaction are unstable towards pairing into composite objects called Cooper pairs which can be thought of as a bound state of two electrons at the Fermi level with equal and opposite momenta. The way that the electrons are able to overcome their repulsion and experience an effective attractive interaction is through coupling to the lattice, which provides a polarizable medium through which the electrons can communicate. The basic picture is that an electron will create a local region of increased positive charge which will then attract a secondary electron. A separation of electronic and lattice time scales combined with charge screening within the metal then allows this effective attractive interaction to overcome the Coulomb repulsion. At the microscopic level, this interaction can be thought of as being mediated by phonons, an exchange of the quantized vibrational excitations of the crystal lattice. It is the quasiparticles near the Fermi surface that participate in this process, and the presence of the filled Fermi sea is essential because it renders the phase space effectively two-dimensional which promotes the bound state formation.

These Cooper pairs then condense into a macroscopic condensate similar in spirit to a Bose-Einstein condensate (Cooper pairs are bosonic spin 1 objects) that behaves in some sense as having a macroscopic wave function ψ corresponding to the order parameter in the Ginzburg-Landau theory. This microscopic theory then allows us to understand the experimental phenomenology of the superconducting state. In particular, the development of the spectroscopic gap for quasiparticles reflects the binding energy of the Cooper pair. Furthermore, any current through the sample is carried by the coherent superconducting condensate and the presence of the quasiparticle gap implies there are no states for Cooper pairs to scatter into. Instead, scattering requires a perturbation of the entire condensate which requires a large amount of energy. Thus, the Cooper pairs are impervious to scattering from lattice defects and impurities resulting in a zero-resistance state.

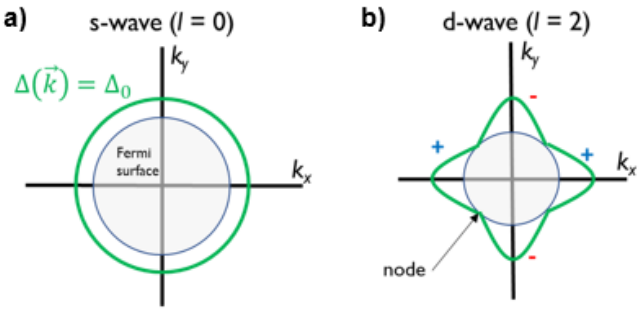

Figure 1.2. Superconducting pairing and order parameter symmetry. a) *s*-wave symmetry found in conventional superconductors. The gray circle represents the Fermi surface and the green circle the superconducting gap that forms in the superconducting state. In the *s*-wave state, the gap is rotationally isotropic in momentum space. b) *d*-wave symmetry (B_{1g} symmetry in a crystal with tetragonal symmetry) found in the cuprate superconductors. Here the gap varies in magnitude and sign with 4-fold symmetry as a function of angle. This leads to nodes along the Brillouin zone diagonals where the superconducting gap goes to zero.

The BCS solution followed from considering the following Hamiltonian:

$$H_{BCS} = \sum_{k,s} \xi_k c_{ks}^{\dagger} c_{ks} + \sum_{k,k'} V(k,k') c_{k\uparrow}^{\dagger} c_{-k\downarrow}^{\dagger} c_{-k'\downarrow} c_{k'\uparrow} \quad (1.2)$$

Here the *c*'s are fermionic creation and annihilation operators, ξ_k is the single-particle kinetic energy measured from the chemical potential, and V represents the pairing interaction, which in the original BCS formulation was constrained to only connect states with opposite momenta and opposite spin, and to be a point-like interaction that only occurs in a narrow energy window near the Fermi surface.

The solution to this Hamiltonian was obtained via a variational method with the following trial wave function:

$$|\psi_{groundstate}\rangle = \prod_k \left(u_k + v_k c_{k\uparrow}^{\dagger} c_{-k\downarrow}^{\dagger}\right)|\gamma\rangle \quad (1.3)$$

Here $|\gamma\rangle$ is the vacuum state, and the u_k, v_k are variational coefficients which correspond to the probabilities that a pair-state with a given k is either occupied or unoccupied. The result of the variational solution is that the u_k, v_k have a fixed phase relation that is independent of k, resulting in a macroscopic quantum superposition (the superconducting state). The energy gap that falls out of this solution is as follows:

$$\Delta_k = -\frac{1}{2} \sum_l \frac{\Delta_l}{\left(\Delta_l^2 + \xi_l^2\right)^{1/2}} V(k,l) \quad (1.4)$$

This is the minimum energy for quasiparticle excitations, and also corresponds to the order parameter in the phenomenological Ginzburg-Landau theory. This equation must be solved

self-consistently. One trivial solution is $\Delta = 0$, which is the normal, non-superconducting state. However, for a negative (attractive) V, this equation will also have a non-trivial solution where Δ is non-zero. This corresponds to a symmetry-broken superconducting state with a critical temperature T_c that is related to the magnitude of Δ.

The symmetry of the gap and pair wavefunction are important features of the superconducting state and can provide clues to the underlying pairing mechanism. Because the constituent particles making up the Cooper pair are fermions, the pair wavefunction and thus the gap function must be anti-symmetric upon exchange of particles and the pairing symmetries of superconductors can be classified subject to this constraint. The spatial component of the wavefunction can either be symmetric, in an even angular momentum channel ($l = 0$ (*s*-wave), $l = 2$ (*d*-wave)…) or antisymmetric, in an odd angular momentum channel ($l = 1$ (*p*-wave), $l = 3$ (*f*-wave),*…)*. In order for the full wavefunction to be antisymmetric, the spin component of the wave function must be antisymmetric (spin singlet) in the former case and symmetric (spin triplet) in the latter. The choice of the pairing interaction V in the original BCS formulation only allows for the spin singlet *s*-wave case, but for more general pairing interactions, other gap symmetries are possible. This classification is only strictly accurate in free space; within the crystal environment, the pairing symmetry will be classified according to the irreducible representations of the underlying crystal point group symmetry. Phonon-mediated BCS superconductors have the simplest possibility in which the gap opens isotropically on the Fermi surface (Figure 1.2a). This stems from the fact that the electron-phonon interaction is essentially a point interaction and rotationally symmetric.

In the original BCS formulation, the superconducting critical temperature is given by the following expression:

$$T_c \sim \hbar\omega_D \exp\left(-1/gv\right) \quad (1.5)$$

Here, ω_D is the Debye frequency and $\hbar\omega_D$ is the relevant phonon energy scale, g is the strength of the electron-phonon interaction, and v is the density of states at the Fermi level. A more detailed treatment of the electron-phonon interaction and Coulomb repulsion due to McMillan[23] gives the following more accurate form:

$$T_c \sim \hbar\omega_D \exp\left(-\frac{1.04(1+\lambda)}{\lambda-\mu^*(1+0.62\lambda)}\right) \quad (1.6)$$

Here λ is the electron-phonon coupling constant which is calculated from the electronic matrix elements and phonon frequency spectrum, and μ^* is the Coulomb pseudopotential which is the bare Coulomb interaction renormalized by screening and the effects of the different time scales of electronic repulsion and phonon attraction. A few interesting consequences follow from this expression. One is that, somewhat counter-intuitively, materials that are extremely good conductors in the normal state, indicating weak scattering from phonons and thus a small electron-phonon coupling, are expected to be poor superconductors. This is borne out experimentally in that none of the noble metals (Cu, Ag, Au) have been found to be superconducting. A second consequence of this expression is that it predicts a "maximum T_c" for a given class of materials. This arises because if we imagine tuning the phonon spectrum, maximizing the pre-factor and exponential factor require a maximization and minimization of the phonon frequency respectively, creating a competitive situation with a maximum T_c at an optimal compromise. Although the McMillan formula is not completely general, it does suggest that phonon-mediated superconductivity is subject to constraints limiting the critical temperature. This is consistent with the fact that nearly all phonon-mediated superconductors have $T_c < \sim 30$K. There are a few notable exceptions with idiosyncratic circumstances. For example[24], the compound MgB_2 has $T_c \sim 39$K which is achieved via a combination of its multiband Fermi surface with different superconducting gaps and a strong coupling of the electronic states to specific phonon modes. Another example is certain compounds under very high hydrostatic pressure[25] which induces an enhancement of the phonon energy scale.

In summary, three key features of the original BCS superconductors, also referred to as "conventional" superconductors, are as follows: the attractive interaction is mediated by electron-phonon coupling, the superconducting gap exhibits an isotropic *s*-wave ($l = 0$) symmetry, and the critical temperature T_c is fundamentally limited to relatively low temperatures by the electron-phonon coupling strength and realistic material parameters (with some exceptions). Another key feature is that these materials have relatively weak electronic

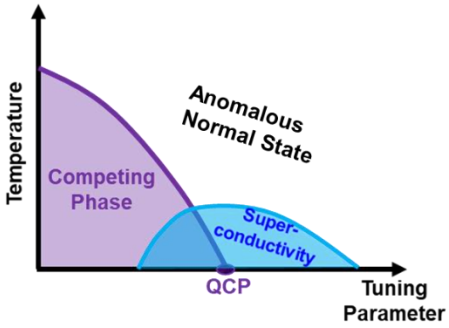

Figure 1.3. Generic phase diagram of unconventional superconductors as a function of temperature and some non-thermal tuning parameter. A symmetry breaking phase (purple) is suppressed by the tuning parameter and ends in a putative quantum critical point (QCP). A dome of superconductivity (blue) emerges centered near the QCP. The normal state typically exhibits anomalous properties not well described by standard paradigms, such as the Fermi Liquid.

correlations, with normal state properties that are well understood within the Fermi liquid paradigm.

In 1986, the era of "unconventional" superconductors was brought into the forefront of condensed matter physics research with the discovery of the cuprate superconductors by Bednorz and Muller[26] with an unbelievably (at the time) high T_c of 35K. Within a few years, an intense flurry of experimental research efforts raised the T_c of cuprates above liquid nitrogen temperature, and the current record stands at T_c = 138K in the compound $Hg_{0.8}Tl_{0.2}Ba_2Ca_2Cu_3O_{8+\delta}$[27]. These high T_cs were clearly incredibly exciting from the technological use perspective. However, the high T_c of these compounds is arguably one of the least interesting things about them; the complexity of the many-body phenomena responsible for and intertwined with the superconducting state is really what has driven many of the developments of condensed matter physics on both theoretical and experimental fronts over the past decades. In some sense, these materials are the last place one would naively look for superconductivity, let alone at high temperatures. The parent compounds are brittle ceramics with strong Coulomb electron-electron interactions and host an antiferromagnetic Mott insulating electronic state and only upon doping the system with charge carriers does superconductivity emerge. As the name "unconventional superconductors" suggests, they are defined precisely by what they are not; the superconducting pairing mechanism or "glue" that allows Cooper pair formation is not due to phonons and the pairing symmetry and gap do not have *s*-wave symmetry.

By now there is overwhelming evidence that the cuprates have a *d*-wave superconducting order parameter, more specifically $d_{x^2-y^2}$, which is in the B_{1g} irreducible representation of the tetragonal symmetry point group. In contrast to a fully gapped *s*-wave superconductor, the *d*-wave (Figure 1.2b) breaks the tetragonal symmetry and oscillates as a function of the in-plane angle. This leads to certain *k* points where the gap goes to zero (these are referred to as "nodes") meaning there are quasiparticle excitations arbitrarily close to the Fermi level. The *d*-wave nature affects the thermodynamic properties such as specific heat or thermal conductivity at low temperatures and can be inferred from those signatures. However, the most convincing "smoking gun" evidence is from phase-sensitive measurements such as the tri-corner superconducting rings experiments[28] where a half magnetic flux quantum is observed at the 3-junction ring, which is only expected to occur in the case of a *d*-wave symmetry order parameter.

In the present day, the library of families of unconventional superconductors has grown, including heavy fermion compounds, organic conductors, uranium-based compounds, kagome metals, two-dimensional moiré heterostructures, and the Fe-based superconductors. In spite of these materials often exhibiting quite different microscopic physics, there are also many unifying characteristics. These materials tend to be quasi-low-dimensional and have bands near the Fermi energy built from *d* or *f* orbitals. Relatedly, these materials also exhibit strong correlations resulting from strong electron-electron interactions. These interactions often drive the formation of collective broken symmetry phases such as antiferromagnetism, charge density wave, and electronic nematic order.

The presence of strong electronic correlations implies that a superconducting state in such a system will be unlikely to be of the BCS-like phonon mediated, *s*-wave symmetry sort. This is because the *s*-wave pairing wave function maximizes the probability of the pairing particles to be at the same location, which is possible in materials that are conventional superconductors because of the weak electron-electron interactions and highly efficient screening. For unconventional superconductors, this type of pairing will be highly unlikely or impossible, and the dominant pairing interactions will be those that allow the pair participants to avoid each other. This in turn often implies interactions that are peaked at a non-zero momentum transfer and will lead to pairing symmetries that are not the isotropic *s*-wave, such as the *d*-wave pairing of the cuprates.

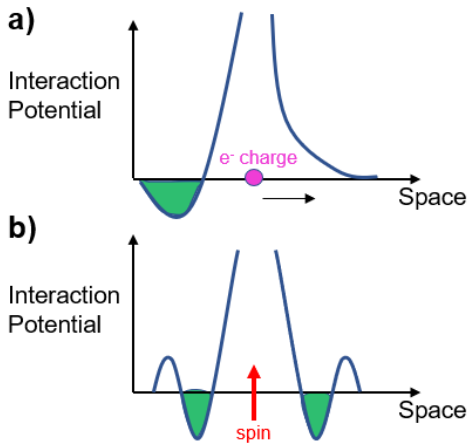

Figure 1.4. Interaction potentials leading to superconducting pairing[5]. a) Phonon-mediated pairing. An electron moving through the ionic lattice background creates an interaction potential (blue line) which includes an attractive region (green). b) Magnetic fluctuation mediated pairing. The spin of an electron within the environment of the spins of all other electrons with a dominant antiferromagnetic interaction creates an oscillating interaction potential that also can create attractive regions.

If the point-like electron-phonon interaction is not mediating the superconducting pairing, then there must be some other pairing "glue" present in these systems. A clue to what that might be is given by considering that the phase diagrams many of these materials demonstrate a very similar phenomenology in which as a function of some tuning parameter like pressure or chemical substitution, an ordered magnetic phase is suppressed towards zero temperature, and the superconductivity emerges as a "dome" near a putative quantum critical point associated with the magnetic phases (Figure 1.3). Near this region, the magnetic phase is competing for the conduction electrons less, and its fluctuations are very strong. This naturally leads one to suppose that it is the spin fluctuations associated with the proximate ordered phases that are mediating the superconducting pairing.

An intuitive way to understand how this might occur is to go back to the original BCS picture. There, the background ionic lattice provides a polarizable medium which allows the interaction potential between electrons to have an attractive region (Figure 1.4a). Analogously, the spin degrees of freedom can behave as a polarizable medium, for example a background of disordered spins with antiferromagnetic interactions, which can also have attractive components (Figure 1.4b). The strength of this interaction will be roughly proportional to a generalized susceptibility χ associated with the ordered phase, which becomes very large near the magnetic phase boundary and putative quantum critical point which is often where superconductivity is found to be the strongest. Such "spin-fluctuation mediated" theories have been investigated for

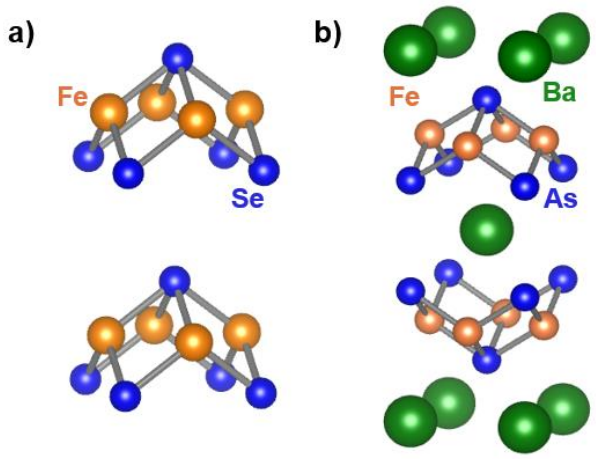

Figure 1.5. Crystal structure of Fe-based superconductors. a) FeSe b) $BaFe_2As_2$

the cuprates, heavy fermion compounds, and the Fe-based superconductors. However, the question of superconducting pairing in these systems is far from settled both experimentally and theoretically. This is largely due to the complicated normal state out of which superconductivity emerges, the complications of a quantum critical point coupled to itinerant fermions, and the fact that it is questionable whether or not the superconducting pairing can even be understood in a BCS-like way where the electrons can be separated from the bosonic excitations mediating the pairing. It may be that such a separation is not possible, as the electrons themselves are ultimately the degrees of freedom forming the pairing interaction, unlike the case of phonons in the original BCS picture. This situation would preclude the sort of controlled diagrammatic perturbative expansion that has led to such detailed understanding of the conventional BCS superconductor.

1.2 Fe-based Superconductors

The cuprate superconductors were discovered in 1986 and for two decades, they stood alone as high T_c unconventional superconductors. This changed in 2008 with the discovery that the compound $LaFeAsO_{1-x}F_x$ could host superconductivity at T = 26K[29]. As with the cuprates, these materials were perhaps not the most natural place to look for superconductivity. The magnetic moment of the Fe ions was thought to be antagonistic to superconductivity according to "traditional" wisdom. In addition to the exciting fact that the cuprates were not a lone anomaly,

in many respects these compounds were a much more attractive system for trying to understand unconventional superconductivity. In contrast to the cuprates, the parent compounds of Fe-based superconductors are metals of which large, high-quality single crystals can be grown through relatively simple techniques like solution flux growth. Furthermore, superconductivity can be induced through a variety of different tuning parameters. Lastly, the phase diagram of the Fe-based superconductors, although still complex, is considerably simpler than the cuprates with phase boundaries that are precisely known and relatively well understood (the "pseudogap" phase of the cuprates has been notoriously difficult to understand).

Two notable differences between the cuprates and the Fe-based superconductors are: (1) the former are single-band while the latter are multi-band, which leads to quite different specific behaviors in the magnetic structure and superconducting gap symmetry, for example. (2) The electronic correlations are much stronger in the cuprates and are driven by the Hubbard U energy scale, while in the Fe based superconductors (relatively weaker) correlations are a result of the Hund's coupling J_H energy scale. In spite of all the differences, the cuprates and Fe-based compounds do hint that high T_c superconductivity should be looked for in materials with quasi two-dimensional crystal structures/Fermi surfaces and interaction strengths that are close to magnetic instabilities.

In the following sections I outline the relevant physical properties and background information of Fe-based compounds to motivate the research that makes up this thesis.

1.3 Crystal and Electronic Structure

Although there are a number of different families of Fe-based superconductors, they share many basic features. From a purely structural perspective, all of the families are layered materials built around a common structural motif of two-dimensional planes of Fe tetrahedrally coordinated by either chalcogenide (S, Se, Te) or pnictide (P, As) atoms. These layers are then stacked along with different types of spacer layers to form the full crystal structure which exhibits four-fold tetragonal symmetry. Two examples are the iron chalcogenide FeSe which exhibits the simplest crystal structure with no spacer layers and a space group $P4/nmm$ (Figure 1.5a), and the "122" iron pnictide $BaFe_2As_2$, the focus of this thesis, which has alkali-earth atoms of Ba as a spacer layer and space group $I4/mmm$ (Figure 1.5b).

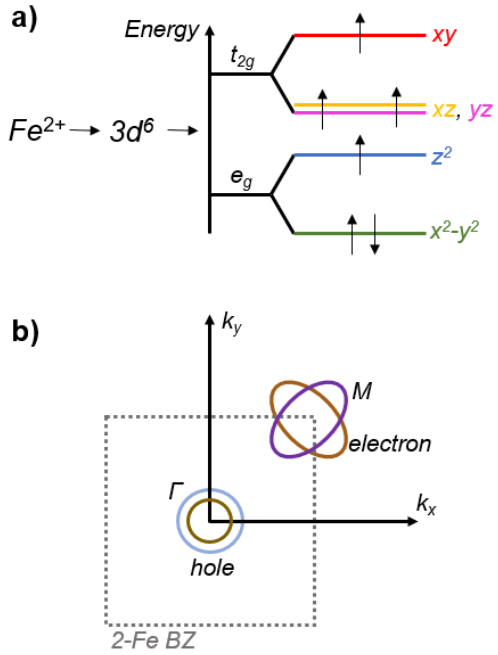

Figure 1.6. Electronic structure of Fe-based superconductors. a) Energy levels within the crystal environment of Fe-based superconductors. The degeneracy of the *d* orbitals is split by the crystal field. The electrons fill these levels in a high spin configuration due to the intraatomic Hund's coupling. b) Generic Fermi surface of Fe-based superconductors in the 2-Fe Brillouin zone with multiple circular hole pockets at the *Γ* point and multiple elliptical electron pockets at the *M* point.

This crystal structure informs many of the main features of the electronic structure, which is dominated by the 3*d* orbitals of the Fe ions. From the atomic orbital point of view, in this crystal environment the Fe atoms have a valence of 2+ corresponding to a $3d^6$ electronic configuration. The quasi-tetrahedral crystal field environment breaks the degeneracy of the *d* orbitals into approximate t_g and e_{2g} orbitals which are further split from deviations from perfect tetragonality (Figure 1.6a). Density functional theory calculations predict that the electronic states at the Fermi level are dominated by these five (d_{xy}, d_{xz}, d_{yz}, d_z^2, and $d_{x^2-y^2}$) Fe orbitals with some amount of hybridization with the pnictogen/chalcogen atomic states and result in, for the parent compound, compensated multi-band semimetals with a Fermi surface consisting of multiple hole pockets at the *Γ* point and multiple electron pockets at the *M* point (in the 2-Fe unit cell Brillouin zone) (Figure 1.6b). The orbital content of these bands varies as a function of momentum, and the bands actually crossing the Fermi energy are a combination of d_{xy}, d_{xz}, and d_{yz} character. The quasi-2D crystal structure causes the bands to disperse only weakly along the out of plane *c* lattice direction, and thus the Fermi pockets are roughly cylindrical. These features have largely been confirmed experimentally through ARPES[30] and quantum oscillation[31]

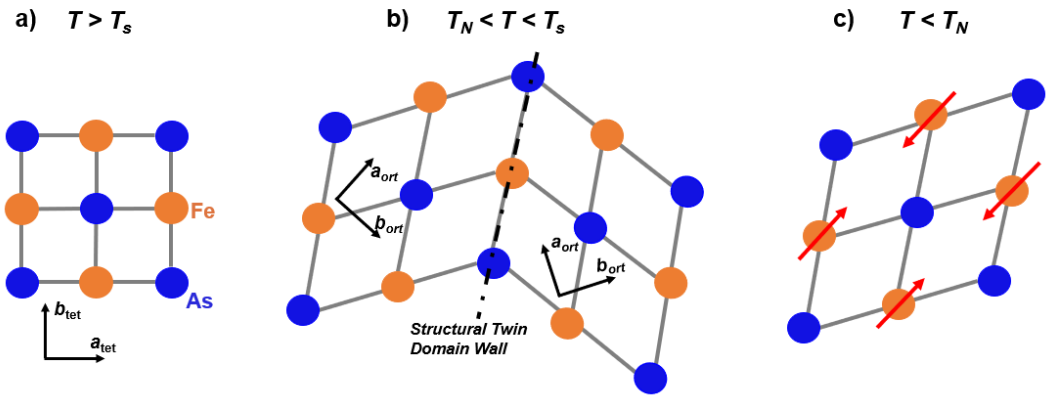

Figure 1.7. Symmetry breaking phase transitions in Fe-based superconductors. a) In the fully symmetric normal state, the crystal has D_{4h} point group symmetry. The FeAs plane is a square with paramagnetic Fe spins. b) At T_s, the crystal undergoes a structural transition where the FeAs square distorts into a diagonal along the Fe-Fe direction ([110] or [1-1 0]) which lowers the point group symmetry from tetragonal to orthorhombic. Below T_s, structural twin domains and domain walls form. c) At T_N, the Fe spins order antiferromagnetically in a stripe pattern with a $\boldsymbol{q} = (\pi, \pi)$ wave vector.

measurements, although the experimentally observed band widths are lower and effective masses are higher than those calculated from first-principles. These renormalizations have been taken to be a sign of the presence of electronic correlations[32] that vary in strength across different compounds (for $Ba(Fe_{1-x}Co_x)_2As_2$ this mass enhancement is ~2 but can be much larger in other families or for hole doping). In contrast to the cuprates where strong correlations arise due to the Hubbard U energy scale from strong Coulomb electron-electron interactions or the heavy fermions where correlations arise from the Kondo coupling between the conduction electrons and localized 4f electrons, in the Fe-based superconductors it has become well established that electronic correlations can be traced to the Hund's coupling J_H.

The Hund's coupling is an intra-atomic exchange interaction which favors the high-spin atomic configuration and is central here because of the multiorbital nature of the Fe-based superconductors. This interaction affects the metallic ground state in subtle yet dramatic ways, marking these materials as "Hund's Metals"[33–35]. In particular, it induces a charge/spin dichotomy where the spin degrees of freedom are localized in spite of charge itinerancy and suppresses the energy scale for the formation of a Fermi liquid[36], leading to "bad metal" phenomenology. Some examples of these bad metal signatures are large values of the dc resistivity and incoherent charge dynamics seen in optical conductivity measurements[37]. Additionally, the Hund's coupling promotes orbital differentiation in which different orbitals experience different amounts of correlation. In the most extreme case, this can lead to an orbital

selective Mott phase[38], where one orbital becomes localized while others remain itinerant. Experimental evidence of such a phase has been found in the iron chalcogenides[39].

1.4 Broken Symmetry: Magnetic, Nematic, and Superconducting Order

Looking to the doping-temperature phase diagram of $Ba(Fe_{1-x}Co_x)_2As_2$, we can identify the presence of three different symmetry-broken electronic phases: magnetism, nematic order, and superconductivity (Figure 1.7). The body of work contained in this thesis involves using uniaxial stress to tune and probe the interplay of these different intertwined phases. Here I outline the relevant background for each of these symmetry-broken states.

1.4.1 Magnetism

First principle calculations indicate a complex array of competing spin fluctuation tendencies in these compounds, including $\boldsymbol{q}$ = 0 Stoner ferromagnetism behavior, nearest-neighbor antiferromagnetic superexchange, and $\boldsymbol{q}$ = (π, π) Fermi surface nesting driven fluctuations between the hole pockets at gamma and the electron pockets at *M*[40]. Experimentally, the parent compound $BaFe_2As_2$ is found to undergo long-range antiferromagnetic order at a temperature of *T* ~135 K to a state where the Fe spins order into a stripe configuration where the spins are parallel along one Fe-Fe direction and anti-parallel along the other (Figure 1.7c). This magnetic structure can be seen directly in neutron scattering experiments[41] and also manifests indirectly through electrical transport and heat capacity. The fact that these compounds are metallic and the ordering vector $\boldsymbol{q}$ = (π,π) matches the Fermi surface nesting vector suggests that this state is an itinerant spin density wave, a scenario which is supported by the quantum oscillation measurements which found that the reconstructed Fermi surface is consistent with the band-folding that such a state would imply. In this itinerant weak-coupling picture, the ordering can be understood by considering the noninteracting Lindhard susceptibility:

$$\chi_0(q) = \frac{f(\epsilon_k) - f(\epsilon_{k+q})}{\epsilon_k - \epsilon_{k+q}} \quad (1.7)$$

Because of the nesting between the hole and electron Fermi pockets, this noninteracting susceptibility will become large for $\boldsymbol{q}$ = (π,π) which potentially could induce the spin density wave instability after considering the renormalized susceptibility in the random phase approximation (RPA):

$$\chi_{RPA}(q) = \frac{\chi_0(q)}{1-J(q)\chi_0(q)} \quad (1.8)$$

However, it is also clear that the magnetism in Fe-based superconductors cannot be fully understood in itinerant terms. For example, while the ordered moment is small, consistent with an itinerant scenario, the fluctuating local moment is much larger, suggestive of local moment behavior. Furthermore, neutron scattering experiments have observed spin waves up to high energies inconsistent with itinerant magnetism, and some compounds exhibit magnetic ground states that cannot be understood in terms of Fermi surface nesting. These features suggest that a local, strong-coupling point of view is the appropriate starting point. In this scenario, the model would be a Heisenberg J_1-J_2 Hamiltonian that treats the superexchange interactions between nearest neighbors and next nearest neighbors:

$$H = J_1 \sum_{neigh.}^{near.} s_i \cdot s_j + J_2 \sum_{neigh.}^{next.\ near.} s_i \cdot s_j \quad (1.9)$$

This model also predicts the observed magnetic structure when $J_2 > |J_1|/2$. Thus, it seems that the Fe-based compounds are in a regime intermediate between strong-coupling local moments and weak-coupling itinerant magnetism. This dichotomy is still a matter of considerable debate[41,42] and is extremely important given that the fluctuating magnetism is likely central in the superconducting pairing mechanism.

Regardless of the microscopic mechanism of the magnetism, it can be described phenomenologically by a Landau free energy as follows:

$$F_{magnetic} = F_0 + \chi_{mag}^{-1}(\Delta_X^2 + \Delta_Y^2) + b(\Delta_X^4 + \Delta_Y^4) + c\Delta_X^2\Delta_Y^2 + d(\Delta_x \cdot \Delta_x)^2 \quad (1.10)$$

Here F_0 represents the non-magnetic contributions to the free energy and the Δ_X and Δ_Y are the two possible order parameters, corresponding to the two possible stripe directions. Only one of these will be nonzero within a single magnetic domain below the phase transition. This phase transition is triggered when the second term changes sign, reflecting a divergence of the magnetic susceptibility at the wave vector $\boldsymbol{q} = (\pi,\pi)$:

$$\chi_{mag}\big(q = (\pi,\pi)\big) = \frac{A}{T-T_N} \quad (1.11)$$

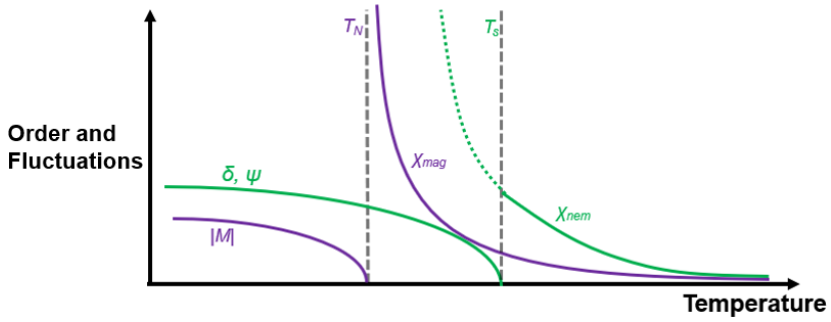

Figure 1.8. Order parameters and fluctuations for the magnetic (purple) and nematic (green) phases. The magnetic and nematic susceptibilities diverge towards their respective phase transitions. The nematic susceptibility diverges towards the bare transition temperature T^* and is cut off (green dashed line) by the actual transition temperature T_s. Below the phase transitions, the associated order parameters grow. For magnetism this is the sub-lattice magnetization ($|M|$) and for nematicity these are the structural (δ) and electronic (ψ) rotational symmetry breaking.

This diverging magnetic susceptibility (Figure 1.8, purple) can be observed in neutron scattering as well as NMR experiments, and the interband interactions associated with these $\boldsymbol{q} = (\pi,\pi)$ spin fluctuations seem to be the dominant interaction between quasi-particles.

Upon chemical substitution or applying pressure, this magnetic order is rapidly suppressed to lower temperatures. However, even the paramagnetic doped compounds host strong temperature dependent $\boldsymbol{q} = (\pi,\pi)$ spin fluctuations seen by NMR and neutron scattering. This is also true in materials with no static magnetic order such as LiFeAs and FeSe, and in lightly doped FeTe in spite of the double-stripe magnetic ground state of the parent compound. It is clear that $\boldsymbol{q} = (\pi,\pi)$ stripe-type spin fluctuations are present across the phase diagrams of most if not all families of Fe-based superconductors.

1.4.2 Electronic Nematicity

The stripe-type magnetic order described in the previous section breaks time-reversal symmetry as well as both spin rotational symmetry and rotational symmetry of the tetragonal lattice. In the parent compound $BaFe_2As_2$, the magnetic transition is first order and is accompanied by an orthorhombic structural distortion (Figure 1.7a-b) in which the FeAs planes distort along the $[110]_{tet}$ direction, distorting the square lattice into a diamond and leading to inequivalent a, b in-plane lattice constants. This structural transition is in the B_{2g} symmetry channel of the D_{4h} point group of the tetragonal structure, lowering the symmetry from D_{4h} (tetragonal) to D_{2h} (orthorhombic). Depending on the tuning parameter, this structural transition can remain tied to the magnetic transition (as occurs with pressure or phosphorous doping,

among others) or it can split away from the magnetic transition and become second order, which is the case for $Ba(Fe_{1-x}Co_x)_2As_2$. This then implies a nonzero temperature window in which time-reversal and translational symmetry are preserved, but rotational symmetry is broken within a broken symmetry phase distinct from static magnetic order. In contrast to a pure ferro-elastic transition where a structural transition is triggered by a softening phonon instability, an abundance of evidence has accumulated showing that this is not the case in the Fe-based superconductors. Instead, the rotational symmetry breaking is driven by the electronic degrees of freedom, in a phase referred to as "electronic nematic"[43], which is language borrowed from the field of phase transitions in liquid crystals. In such a phase, the order parameter is a "director", which specifies the direction along which the symmetry breaking occurs. In contrast to liquid crystals where the director can point in any direction, coupling with the crystal lattice forces the nematic director to point along the crystal axes, leading to two inequivalent choices for the order parameter. This is referred to as "Ising nematic". Below the nematic phase transition, structural twin domains form corresponding to these two inequivalent choices of which direction to distort along. The presence of these domains masks anisotropies in macroscopic physical properties that can only be accessed by detwinning the sample which can be achieved applying uniaxial stress.

By symmetry, a distortion of the crystal lattice will automatically be accompanied by anisotropies in all physical properties of the crystal. One indication that the nematic transition is driven by electronic degrees of freedom is that the electronic anisotropies are much larger than the structural ones; for example, $Ba(Fe_{1-x}Co_x)_2As_2$ with $x = 0.045$ has a spontaneous orthorhombic distortion of $\delta = (a + b)/(a - b) \sim 0.15\%$[44], whereas the corresponding resistivity anisotropy $(\rho_a - \rho_b)/ (\rho_a + \rho_b)$ is ~33%, more than two orders of magnitude larger[45]. Additionally, whereas the orthorhombic distortion evolves monotonically as a function of doping, the electronic anisotropy has a non-trivial composition dependence peaking near $x = 0.03$. Large electronic anisotropies have also been observed in other quantities such as the in-plane magnetic susceptibility[46] and the d_{xz}, d_{yz} orbital energies and occupations. However, the strongest evidence for an electronically driven phase transition comes by measuring the fluctuations in the disordered phase above the transition. In particular, the resistivity anisotropy induced by anisotropic strain (elastoresistivity) which is a proxy for the nematic susceptibility was shown to diverge above the phase transition[47]. Analysis of a Landau mean field free energy demonstrates that this will only occur when anisotropic strain is acting as a conjugate field, coupled to a

primary electronic order parameter which actually drives the instability. The divergence of the nematic susceptibility has also been measured by thermodynamic probes such as the elastocaloric effect[48] and shear modulus[49] measurements and charge sensitive probes such as Raman spectroscopy[50]. These diverging nematic fluctuations are quite generally observed across all families of Fe-based superconductors[51].

The basic features of the nematic order can be elucidated by considering the free energy within the Landau paradigm of continuous phase transitions, assuming the instability is driven by the electronic degrees of freedom:

$$F = \frac{a(T-T^*)}{2}\psi^2 + \frac{b}{4}\psi^4 + \frac{C_{66}^0}{2}\epsilon^2 + \frac{d}{4}\epsilon^4 - \lambda\psi\epsilon + h\epsilon \quad (1.12)$$

Here T^* is the bare nematic transition temperature, ψ is the nematic order parameter, C_{66}^0 is the bare shear modulus, ϵ is the strain in the B_{2g} symmetry channel which acts as the conjugate field for the nematic order, λ is the nemato-elasto coupling constant, and h is uniaxial stress in the B_{2g} symmetry channel. Minimization of this free energy yields the following relations:

$$T_s = T^* + \frac{\lambda^2}{aC_{66}^0} \quad (1.13)$$

$$\frac{d\psi}{d\epsilon} = \frac{\lambda}{a(T-T^*)} \quad (T > T_s) \quad (1.14)$$

$$C_{66} = C_{66}^0 - \frac{\lambda^2}{a(T-T^*)} \quad (T > T_s) \quad (1.15)$$

$$\psi = \sqrt{\frac{a}{b}(T_s - T)} \quad (T < T_s) \quad (1.16)$$

Equation (1.13) demonstrates that the coupling to the lattice raises the transition temperature compared to its bare value T^*. Equation (1.14) gives the Curie-Weiss form for the nematic susceptibility, which diverges towards the bare transition temperature (Figure 1.8, green). Equation (1.15) reflects that fact that even though the lattice degrees of freedom are not driving the instability, coupling to the nematic order causes the shear modulus to go to zero at T_s. Equation (1.16) gives the mean-field behavior for the temperature dependence of the nematic order parameter below the transition. Importantly, it has been shown that the nematic phase transition is described quite accurately by this mean field free energy both above and below the

transition, and the resistivity anisotropy is a faithful proxy for the nematic order parameter[52,53]. The resistivity anisotropy is given by:

$$\frac{\rho_{xx}-\rho_{yy}}{\rho_{xx}+\rho_{yy}} = 2m_{66}\epsilon_{B2g} \propto \chi_{nem}\epsilon_{B2g} \quad (1.17)$$

where $2m_{66}$ is a coefficient of the elastoresistivity tensor $m_{ij,kl}$ given by[54]:

$$m_{ij,kl} = \left.\frac{\partial\left(\Delta\rho/\rho\right)_{ij}}{\partial\epsilon_{kl}}\right|_{\epsilon=0} \quad (1.18)$$

After establishing that the nematic phase is electronically driven, the question remains of which microscopic degrees of freedom are responsible[55]. Either the charge (orbital) or spin degrees of freedom associated with the electrons could be driving the transition. In the former case, such a transition would reflect divergent charge fluctuations towards an ordered state where the occupations and energies of the d_{xz} and d_{yz} Fe *3d* orbitals became inequivalent. In the latter case, diverging magnetic fluctuations are responsible, ordering towards a phase where the magnetic susceptibility along the two in-plane directions becomes inequivalent. This second scenario can be viewed as a "vestigial" order[56] associated with the subsequent magnetic phase transition, where the magnetic stripe phase first melts into a nematic phase with broken rotational symmetry and anisotropic magnetic fluctuations before reverting to the fully symmetric phase at higher temperatures. In this view, the nematic order parameter can be written in terms of the magnetic order parameters contained in the magnetic free energy from Section 1.4.1:

$$\psi = < \Delta_X^2 - \Delta_Y^2 > \quad (1.19)$$

Here <…> denotes a thermodynamic average. The normal state (above both T_N and T_s) is then described by $<\Delta_X> = <\Delta_Y> = 0$ and $<\Delta^2_X> = <\Delta^2_Y>$, implying that $\psi = 0$ and time-reversal, spin rotation, and the D_{4h} point group symmetry are all preserved. The nematic phase below T_s corresponds to $<\Delta_X> = <\Delta_Y> = 0$, but $<\Delta^2_X> \neq <\Delta^2_Y>$ which gives $\psi \neq 0$, breaking rotational symmetry but preserving time reversal and spin rotation symmetry. Finally, the magnetic phase below T_N is given by $<\Delta_X> \neq 0$ and $<\Delta_Y> = 0$ (or the reverse) and $<\Delta^2_X> \neq <\Delta^2_Y>$, breaking all three symmetries.

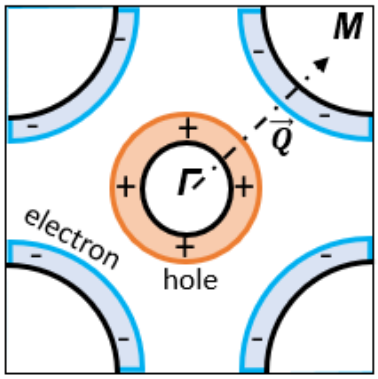

Figure 1.9. s^{+-} superconducting gap symmetry, found in many Fe-based superconductors. This is an unconventional *s*-wave state where the sign of the gap changes sign moving from the hole pockets to the electron pockets.

At least in the iron pnictides, most evidence points to the latter scenario of spin-driven nematicity. For example, the experimental observation that the nematic transition line closely tracks the magnetic transition line as a function of tuning parameters is easily explained if the nematic order is a melting of the stripe-type magnetism, whereas this behavior is difficult to explain in the case that nematic order is driven by charge fluctuations with no direct connection to the magnetic order. Additionally, the lattice fluctuations measured by shear modulus experiments and spin fluctuations measured by NMR exhibit a scaling relation that can be naturally explained within the spin-nematic scenario[57]. Finally, as will be discussed further in the next section, the spin-nematic scenario implies a repulsive inter-pocket interaction between electrons which would be expected to favor a $s^{\pm}$ symmetry for the pairing interaction and superconducting gap, and the $s^{\pm}$ gap is the most likely candidate based on experimental evidence. However, the situation may be different in the iron chalcogenides[58] where nematic order occurs in the absence of static magnetic order.

Nematic order is not only found in the Fe-based superconductors. Experimental evidence consistent with a nematic phase has been found in the cuprate superconductors[59,60], quantum hall systems[61,62], the metamagnetic $Sr_3Ru_2O_7$[63], and more recently has been suggested to manifest in superconducting two-dimensional moiré heterostructures[64] and in kagome metals[65] exhibiting charge density waves and superconductivity. The diversity of these materials and the microscopic physics that they host suggests that nematicity may be a generic feature of strongly correlated systems and/or unconventional superconductivity, and thus it is essential to understand which phenomenon are intimately tied to the presence of the nematic order.

1.4.3 Superconductivity

Both the magnetic and nematic transition temperatures are tuned towards zero temperature as a function of a tuning parameter such as pressure and chemical substitution, and eventually superconductivity appears as a dome with a maximum T_c that varies between material families (the maximum T_c in Fe-based superconductors thus far is 55K in the compound $SmO_{1-x}F_xFeAs$[66]). Depending on the material family, superconductivity may coexist with antiferromagnetism and nematicity which is the case for $Ba(Fe_{1-x}Co_x)_2As_2$. In this case, the order parameters of the other symmetry broken phases (the ordered magnetic moment and orthorhombic structural distortion for antiferromagnetism and nematicity respectively) have been found to be reduced[67,68] below T_c demonstrating that these phases are directly competing with superconductivity.

A variety of experimental probes and theoretical considerations have shed light on the pairing mechanism and gap structure. NMR measurements[69] below T_c have demonstrated a drop in the Knight shift which is a measure of the static spin susceptibility, consistent with a spin singlet pairing state and thus an even parity spatial component of the pairing wavefunction. Drawing on inspirations from the cuprates and heavy fermion superconductors, theoretical calculations[40,70–74] have favored a situation in which superconductivity is mediated through exchange of the $\boldsymbol{q} = (\pi,\pi)$ spin fluctuations associated with the antiferromagnetism. In this scenario, a "s^{+-} wave" symmetry paring state is expected where the superconducting gap is rotationally symmetric but changes sign between the Fermi pockets at the center and corners of the Brillouin zone (Figure 1.9). This sign change allows for an attractive pairing state in spite of the repulsive interaction induced by the spin fluctuations. The multiband nature of the Fe-based compounds is essential here, in contrast to the single band cuprates where such a spin-fluctuation exchange pairing can only be attractive with a *d*-wave pairing symmetry where the gap changes sign as you rotate around the single Fermi pocket.

The most conclusive experimental evidence for the s^{+-} symmetry pairing state comes from inelastic neutron scattering. In these measurements, signatures of a resonant magnetic excitation appear only below the superconducting T_c, localized in both energy and momentum.

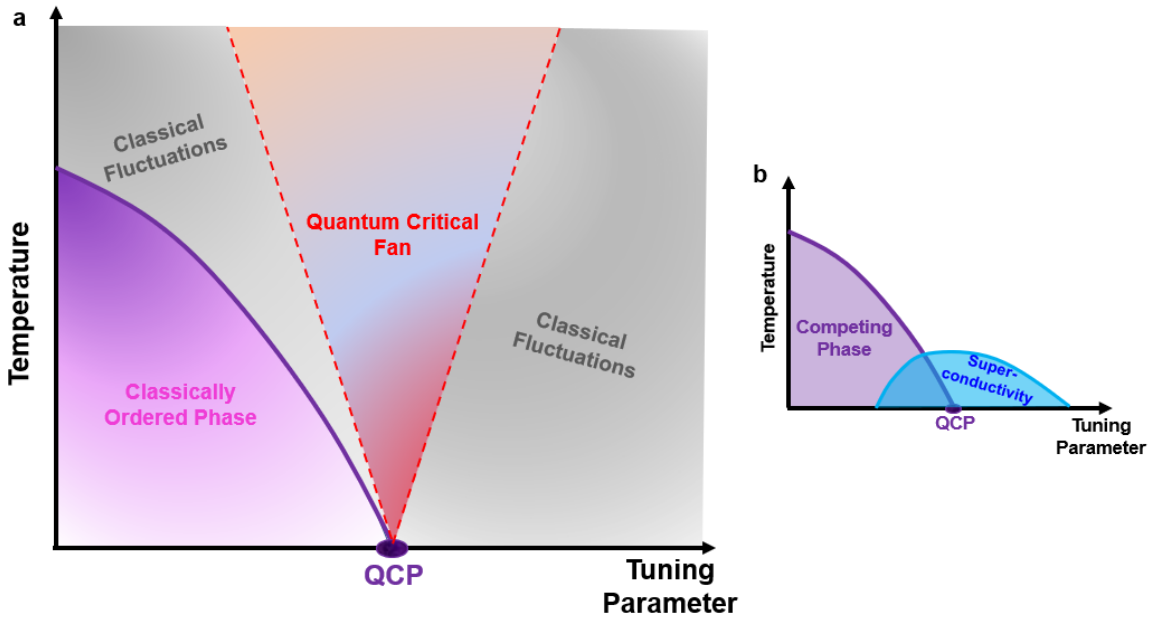

Figure 1.10. Quantum critical phase diagram. a) Generic quantum critical phase diagram as a function of temperature and tuning parameter. The solid purple line marks a symmetry breaking phase that ends in a quantum critical point. The gray regions are areas where classical (thermal) fluctuations are excited and dominate the behavior of the system. Within the multi-colored fan region, quantum fluctuations associated with the QCP are excited. b) Generic phase diagram of unconventional superconductors. A superconducting dome (blue) forms around the QCP associated with the competing phase (purple).

The momentum peak agrees with the (π, π) spin fluctuation wave vector and the energy scale is on the order of the superconducting gap[75]. Such a resonance is also observed in the cuprates and heavy fermions and is strong evidence for a spin-fluctuation mediated pairing mechanism. Furthermore, the momentum space structure of the excitation supports the s^{+-} gap structure. Additionally, NMR measurements of the spin-lattice relaxation rate $^1/T_1T$ in the normal state have demonstrated that the strength of the $\boldsymbol{q}$ = (π,π) spin fluctuations correlates with the strength of the superconducting T_c[76].

Thermodynamic probes such as heat capacity, penetration depth, and thermal conductivity can provide information about the low-lying excitations in the superconducting state, and thus about the superconducting gap structure. For example, in a fully gapped superconductor, these quantities will exhibit exponential temperature dependence below T_c. Measurements in the Fe-based superconductors have been somewhat confounding, in that some indicate fully gapped behavior, expected for the simplest version of the s^{+-} gap, while others imply point or line nodes. It is entirely possible that different compounds have different symmetry order parameters. It is also important to note that even for an s^{+-} pairing state, nodes

are possible depending on the Fermi surface and interaction structure. Overall, most measurements are at least consistent with an s^{+-} pairing state (especially in $Ba(Fe_{1-x}Co_x)_2As_2$)[77–80] with the possible presence of small gaps or deep minima especially in overdoped samples. This is also supported by angle resolved photo emission experiments[81,82].

1.4.4 Quantum Criticality

A key concept in the Fe-based superconductors and quantum materials more generally is the idea of quantum criticality[83–85]. A quantum critical point (QCP) (Figure 1.10a) occurs when a finite temperature continuous phase transition is tuned to occur at zero temperature. At such a point, the transition ceases to be driven by classical thermal fluctuations, and instead is driven by quantum zero-point fluctuations. Exactly at the critical point, the characteristic energy of the ordered phase goes to zero, the spatial and temporal correlation lengths diverge, and the microscopic description of the material ceases to be able to be described in terms of the degrees of freedom of the phases on either side of the QCP. Instead, the microscopic states are complex quantum superpositions that fluctuate at all length scales. This leads to remarkable behavior, even at temperatures above the $T = 0$ critical point in a broad "quantum critical" regime. The rough idea is that the highly entangled critical form of the microscopic states only emerges for length scales smaller than the correlation length ξ. When ξ is less than the thermal de Broglie length scale $\hbar c/k_B T$, thermal fluctuations excite the non-quantum critical fluctuations. However, when $\xi > \hbar c/k_B T$, the quantum critical fluctuations are thermally excited, and since ξ diverges on approach to the QCP, the quantum critical region has a characteristic fan shape where the effects of quantum criticality are accessed for wider and wider ranges of the tuning parameter as the temperature is increased.

Understanding quantum criticality and its consequences for physical observables has remained a formidable challenge. This is particularly true in metallic systems where the added complexity of coupling to the low energy electronic degrees of freedom on the Fermi surface must be considered. In the Fe-based superconductors, there is even further complexity since both the magnetic and nematic transition phase boundaries are suppressed to zero temperature, possibly leading to both a magnetic and nematic quantum critical point[86] beneath the superconducting dome.

Evidence for a quantum critical point and its effects on finite temperature properties has been observed in a wide variety of Fe-based superconductors. For example, measurements of the doping dependence of the spin lattice relaxation rate $^1/T_1T$ and nematic susceptibility χ_{nem} have shown that both T_N and T^* appear to cross through zero near optimal doping. The most clear-cut case[87] is the isovalent-substituted $BaFe_2(As_{1-x}P_x)_2$ which is an extremely clean system, evidenced by observation of quantum oscillations across a broad range of composition[88,89]. These measurements reveal enhancement of the quasiparticle mass on approach to a doping level ~ x = 0.3, consistent with a quantum critical point at that location. Such a mass enhancement has also been argued for based on specific heat[90] and London penetration depth[91] measurements. This mass enhancement is a result of the increasingly strong fluctuation strength inducing increasingly strong electronic correlations upon approach to the critical point and is a hallmark signature of a QCP in metallic systems which has also been observed in the cuprate and heavy fermion superconductors.

Another hallmark of quantum criticality in itinerant systems is the so-called "strange metal" phase[92–96]. This phase is characterized by non-Fermi liquid behavior in electronic transport, in particular a linear-in-temperature resistivity that is observed over multiple decades down to low temperature. This phenomenology suggests a universal dissipative timescale $\tau \sim \hbar/k_BT$ which is expected when temperature is the only relevant energy scale and has been suggested to be a universal bound on scattering/dissipation (it is often referred to as "Planckian dissipation" or the "Planckian limit")[10]. Such behavior has been observed in multiple families of iron pnictide and iron chalcogenide superconductors.

There is an intimate connection between quantum criticality and the superconductivity. Circumstantial, yet fairly universal, evidence of this is that for many unconventional superconductors, the superconductivity as a function of tuning parameter appears as a "dome", where the maximum or "optimal" T_c is found in the vicinity of a QCP associated with a proximate, usually magnetic phase (Figure 1.10b). This suggests that the fluctuations of the proximate phase, either quantum or classical, are potentially responsible for the superconducting pairing. For the Fe-based superconductors, there have been multiple theoretical works demonstrating that a metallic system tuned through an Ising nematic QCP can induce both a superconducting dome and non-Fermi liquid behavior in the normal state[97,98]. In this case, the

nematic fluctuations are not necessarily themselves the "original" bosons responsible for pairing. Instead, due to their $\boldsymbol{q} = 0$ nature they are able to enhance the T_c of any existing pairing mechanism, regardless of its symmetry. This is similar to the case where superconductivity can be enhanced in the vicinity of a purely structural transition, and pairing is enhanced by the associated softening phonon. One piece of experimental evidence for the role of the nematic QCP in the superconductivity is that most optimally doped samples for a wide variety of materials families show a diverging nematic susceptibility with $T^* \sim 0$[51].

One confounding theoretical idea is that it has been suggested[99] that when one includes the effects of the nemato-elasto coupling λ which represents the coupling strength between the electronic nematic order parameter and the lattice strain of the same symmetry, the quantum critical fluctuations and their effects are washed out by the noncritical lattice shear modes. This would seem to preclude the scenario where nematic quantum criticality has any role in the superconductivity or non-Fermi liquid behavior in the normal state. However, analysis of the doping and temperature dependence of the elastocaloric effect[48] compared to elastoresistivity and Raman scattering suggests that the nemato-elasto coupling decreases markedly upon approach to the nematic quantum critical point, while the coupling between nematic fluctuations and the conduction electrons increase dramatically. This revives the possibility that quantum critical nematic fluctuations are not washed out and may be involved in the superconductivity.

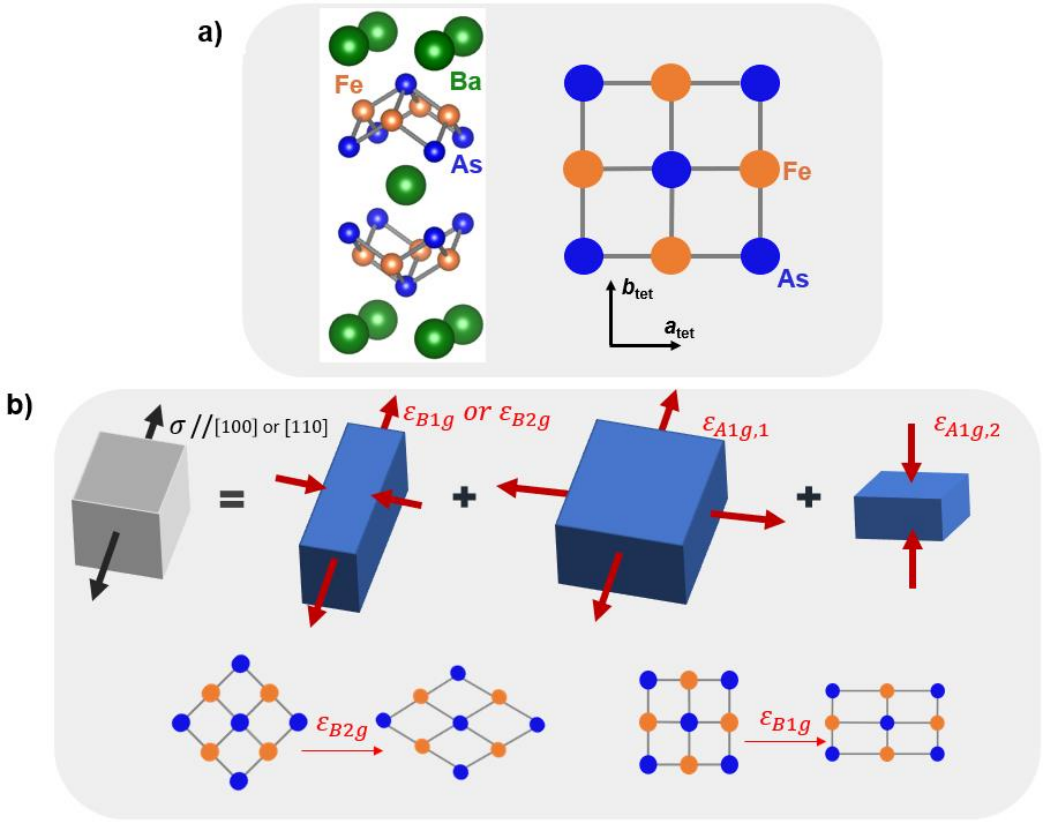

Figure 1.11. a) Crystal structure of $Ba(Fe_{1-x}Co_x)_2As_2$ b) Irreducible strain components induced by uniaxial stress along either [100] or [110].

1.5 Stress and Strain as Tuning Parameters

General concepts about symmetry and group theory used in this section were taken from Lax[100]. Externally applied stresses and strains are particularly attractive tuning parameters in that they keep variables such as disorder constant while also allowing for precise *in-situ* and symmetry-specific tunability. In a crystalline solid, the relation between stress and strain is given by the elasticity tensor C or its inverse the compliance tensor S:

$$\sigma_{ij} = C_{ijkl}\epsilon_{kl} \quad (1.20)$$

$$S = C^{-1} \quad (1.21)$$

Here σ and ϵ are the stress and strain tensors respectively. C also determines the elastic contribution to the free energy:

$$F_{elastic} = \frac{1}{2}\sum_{ijkl} C_{ijkl}\epsilon_{ij}\epsilon_{kl} \quad (1.22)$$

Because the strain tensor is symmetric ($\epsilon_{ij} = \epsilon_{ji}$) and the free energy is symmetric upon exchange of the pairs *ij* and *kl*, the 81 coefficients of the elasticity tensor are reduced to 21 even for a crystal of arbitrary symmetry (In fact, even three of these can be set to zero by a choice of a non-generic set of axes). This reduction allows one to express the stress and strain tensors in "Voigt notation", where stress and strain are written as vectors with 6 components, and the elasticity tensor is a 6 x 6 matrix with 21 independent coefficients:

$$\begin{pmatrix}\sigma_{xx}\\ \sigma_{yy}\\ \sigma_{zz}\\ \sigma_{yz}\\ \sigma_{xz}\\ \sigma_{xy}\end{pmatrix} = \begin{pmatrix}C_{11} & C_{12} & C_{13} & C_{14} & C_{15} & C_{16}\\ C_{12} & C_{22} & C_{23} & C_{24} & C_{25} & C_{26}\\ C_{13} & C_{23} & C_{33} & C_{34} & C_{35} & C_{36}\\ C_{14} & C_{24} & C_{34} & C_{44} & C_{45} & C_{46}\\ C_{15} & C_{25} & C_{35} & C_{45} & C_{55} & C_{56}\\ C_{16} & C_{26} & C_{36} & C_{46} & C_{56} & C_{66}\end{pmatrix}\begin{pmatrix}\epsilon_{xx}\\ \epsilon_{yy}\\ \epsilon_{zz}\\ 2\epsilon_{yz}\\ 2\epsilon_{xz}\\ 2\epsilon_{xy}\end{pmatrix} \quad (1.23)$$

The point group symmetry of a particular material will further constrain the coefficients of the elasticity tensor. For example, $Ba(Fe_{1-x}Co_x)_2As_2$ crystalizes in the space group *I4/mmm* and has tetragonal D_{4h} point group symmetry. In this case we have (choosing the *x* and *y* axes to be along the [100] and [010] crystallographic axes):

$$C = \begin{pmatrix}C_{11} & C_{12} & C_{13} & 0 & 0 & 0\\ C_{12} & C_{11} & C_{13} & 0 & 0 & 0\\ C_{13} & C_{13} & C_{33} & 0 & 0 & 0\\ 0 & 0 & 0 & C_{44} & 0 & 0\\ 0 & 0 & 0 & 0 & C_{44} & 0\\ 0 & 0 & 0 & 0 & 0 & C_{66}\end{pmatrix} \quad (1.24)$$

The use of group theory is extremely useful in order to decompose the strain tensor into components corresponding to the irreducible representations (Γ_i) of the point group. For D_{4h}, this decomposition gives (Figure 1.11):

$$\Gamma_\epsilon = 2A_{1g} \oplus B_{1g} \oplus B_{2g} \oplus E_g \quad (1.25)$$

These strain components do not mix under the symmetry operations of the D_{4h} group. Strains in the A_{1g} symmetry channel are in the trivial representation and thus do not break any symmetries, while strains in all of the other symmetry channels break some subset of the D_{4h} symmetries. E_g is a two-dimensional irreducible representation while all of the others are one-dimensional. The explicit coordinate representation of these components are as follows:

$$\epsilon_{B1g} = \frac{1}{2}\left(\epsilon_{xx} - \epsilon_{yy}\right) \quad (1.26)$$

$$\epsilon_{B2g} = \epsilon_{xy}$$

$$\epsilon_{A1g,1} = \frac{1}{2}\left(\epsilon_{xx} + \epsilon_{yy}\right)$$

$$\epsilon_{A1g,2} = \epsilon_{zz}$$

$$\epsilon_{Eg} = \begin{pmatrix}\epsilon_{xz} \\ \epsilon_{yz}\end{pmatrix}$$

ϵ_{B1g} and ϵ_{B2g} are both symmetry breaking strains that distort the square lattice into a rectangle and diamond respectively and lead to inequivalent *a* and *b* lattice constants. ϵ_{B2g} is in the same symmetry channel as the nematic order parameter in Fe-based superconductors, and acts as the conjugate field to nematic order (see the free energy in Section 1.4.2). $\epsilon_{\mathrm{A1g,1}}$ and $\epsilon_{\mathrm{A1g,2}}$ are both symmetry preserving strains, the former of which induces isotropic in-plane compression or expansion, and the latter induces strain purely along the [001] (*c* lattice) direction. The ϵ_{Eg} component is also symmetry breaking and is composed of out-of-plane shear strains.

Expressions for the Poisson ratios of a material can be written in terms of the elastic constants. The Poisson ratio corresponding to extension along direction *n* and transverse direction *m* is given by:

$$\nu_{n,m} = \frac{-S_{ij\alpha\beta} n_i n_j m_\alpha m_\beta}{S_{ij\alpha\beta} n_i n_j n_\alpha n_\beta} \quad (1.27)$$

with repeated indices summed. In this thesis we will find useful the following four Poisson ratios:

$$\nu_{[100],[010]} = \frac{C_{13}^2 - C_{12}C_{33}}{C_{13}^2 - C_{11}C_{33}}$$

$$\nu_{[100],[001]} = \frac{(C_{12} - C_{11})C_{33}}{C_{13}^2 - C_{11}C_{33}}$$

$$\nu_{[110],[1-10]} = \frac{C_{33}(C_{11} + C_{12} - 2C_{66}) - 2C_{13}^2}{C_{33}(C_{11} + C_{12} + 2C_{66}) - 2C_{13}^2}$$

$$\nu_{[110],[001]} = \frac{4C_{13}C_{66}}{C_{33}(C_{11} + C_{12} + 2C_{66}) - 2C_{13}^2}$$

Due to strongly coupled lattice, electronic, and magnetic degrees of freedom, the Fe-based superconductors are especially amenable to strain-tuning. As described in Section 1.4.2, the strain induced anisotropies in the B_{2g} symmetry channel above the nematic phase transition probe the diverging nematic fluctuations. Another powerful use of externally applied stress in this symmetry channel is to align the nematic domains in order to probe the intrinsic anisotropy of the ordered phase below the phase transition. This idea has been employed to study the intrinsic anisotropies of resistivity, magnetism, and electronic orbital energetics[45,52,101–103]. Strain has also been used to directly tune the ordering temperatures and associated ordering parameters. Resistivity and elastocaloric measurements under uniaxial stress[104–106] have demonstrated the tuning of both T_s and T_N with ϵ_{B1g} and ϵ_{A1g}. Additionally, NMR measurements[107] and neutron scattering experiments[108] under uniaxial stress show an enhancement of T_N and associated magnetic fluctuations above the magnetic ordering temperature for ϵ_{B2g}.

Symmetry is also very powerful for understanding how a physical property responds to applied strains. The idea is that the symmetry content (the irreducible representation) must match on either side of an equal sign. For example, the superconducting T_c is a scalar, and thus must lie in the trivial A_{1g} representation and transform identically under all symmetry operations. This then dictates the following functional form:

$$T_c(\epsilon) = T_c^0\left(1 + a\epsilon_{A1g,1} + b\epsilon_{A1g,2} + c\epsilon_{B1g}^2 + d\epsilon_{B1g}^2\right) + O(\epsilon_{A1g}^2, \epsilon_{B1g\ or\ B2g}^4) \quad (1.28)$$

Here T_c^0 is the zero-strain transition temperature and $O(\ldots)$ are higher order contributions.

Another example is the in-plane resistivity anisotropy, which lies in the B_{2g} representation and thus we have:

$$\frac{\Delta\rho_{xx} - \Delta\rho_{yy}}{\rho_0} \propto \epsilon_{B2g} + O(\epsilon_{B2g}^3) \quad (1.29)$$

We will use this symmetry dictated response concept throughout this thesis.

1.6 Motivation and Thesis Overview

In spite of 15 years of intensive research utilizing a diverse array of experimental and theoretical methods, a number of central questions remain relevant not just to the Fe-based superconductors, but to unconventional superconductivity and quantum materials more broadly. A few of these questions are as follows:

1. What is the role of nematic fluctuations in the superconducting pairing?
2. To what extent is superconductivity driven by quantum criticality?
3. How do nematicity and fluctuating magnetism affect the electronic environment outside the superconducting state?

Additionally, although (see Section 1.5) there have been numerous experimental works using stress and strain to probe nematic fluctuations, study intrinsic anisotropies, and tune the nematic and magnetic phase transition temperatures, the effect of strain on the superconductivity has remained largely unexplored. In this thesis, I will investigate how strain in different symmetry channels affects both the superconductivity and the normal state above T_c in order to shed light on the questions listed above.

In Chapter 2, I will outline the experimental methodology of the measurements. In Chapter 3, I will show that anisotropic strain enhancing nematic order has a drastic effect on the superconductivity near the nematic QCP. This provides realization of a strain-tuned superconductor to metal quantum phase transition as well as provides evidence for the importance of nematic fluctuations for the superconducting pairing. In Chapter 4, I will demonstrate a close quantitative equivalence and scaling relation between symmetric strain and composition as tuning parameters for superconductivity that extends over the majority of the superconducting dome, which is evidence for the quantum critical-driven superconductivity scenario. Finally, in Chapter 5 I will present measurements of the resistivity and Hall coefficient under uniaxial stress which reveal a new elastoresistivity coefficient that probes the sensitivity of the conduction electrons to diverging spin fluctuations. In Chapter 6, I will conclude and summarize and give an outlook to future work to be done building on the results of this thesis.

2. Experimental Methodology

2.1 Crystal Growth and Sample Preparation

The hypotheses and measurements involved in this thesis required large, high-quality single crystals of $Ba(Fe_{1-x}Co_x)_2As_2$ with a dense series of doping levels x across the phase diagram. Single crystals were grown utilizing an FeAs self-flux method as described previously[109–111] (Figure 2.1). First, the FeAs precursor was synthesized using iron powder and arsenic pieces combined in a ratio of 1.05:1.00. The excess iron ensures that there is no unreacted arsenic left at the end of the growth. The starting materials were loaded into alumina crucibles (ACP-CCS Canfield Crucible Set, LSP Industrial Ceramics) and sealed within quartz ampoules using a hydrogen/oxygen torch and insulated by quartz wool under a low-pressure argon atmosphere. The sealed ampoules were then loaded into high-temperature furnaces and heated slowly to 550° C and kept there for 12 hours. This step is necessary to ensure reaction between the iron and arsenic in order to prevent a buildup of partial pressure of arsenic vapor which sublimes at ~600° C. The temperature was then raised to 900° C and kept there for 12 hours after which the ampoules were allowed to cool slowly to room temperature. Additional precautions to prevent exposure to arsenic vapor in case of explosion of the ampoule included enclosing the ampoules within a steel box inside the furnace and placing the furnace within a fume hood during growth. The FeAs precursor was then ground and mixed with variable amounts of cobalt and loaded along with small pieces of barium into new crucibles in a 1:4 (Ba:FeAs) ratio. The barium pieces were washed and rinsed in a heptane bath prior to loading in order to remove the oxidative surface from the material. The crucibles with the (Ba, FeAs, Co) mixture were then loaded and sealed into quartz ampoules as described previously, and heated to 1180° C over 24 hours, kept for 24 hours, and then cooled to 1000° C over 36 hours. The excess FeAs flux was then separated from the single crystal yield by centrifuging the ampoule directly from the furnace at 1000° C. All of the synthesis steps were performed within a low-moisture and low-oxygen glovebox except for the last step of sealing the ampoule.

The synthesis process described above yielded large single crystal $Ba(Fe_{1-x}Co_x)_2As_2$ with a plate-like morphology and mirror-like surfaces along the c-lattice. Precise determination of the

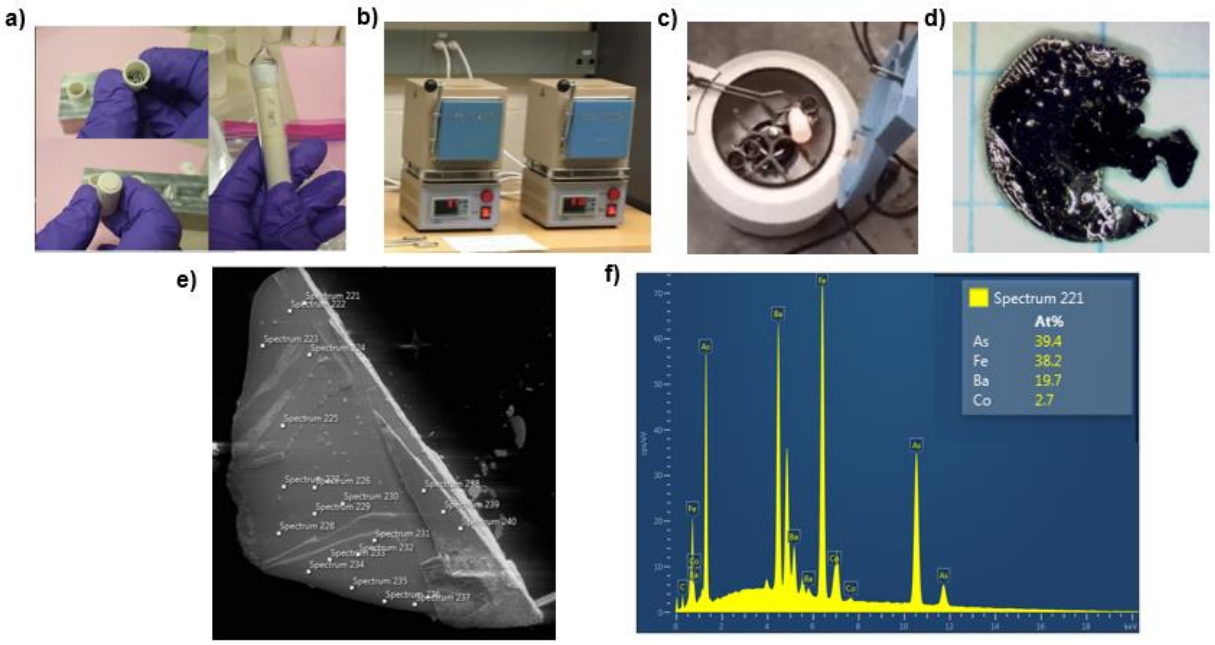

Figure 2.1. Crystal growth of $Ba(Fe_{1-x}Co_x)_2As_2$. a) Materials loaded into alumina crucibles and quartz ampoules. b) High-temperature furnaces and c) centrifuge. d) Single crystal yield of $Ba(Fe_{1-x}Co_x)_2As_2$. The crystal growth is crucible-sized limited and results in platelets with mirror-like surface along the crystal *c*-lattice direction. Grid lines are 5 cm. e) Scanning electron microscope image of a crystallite. White squares indicate the locations where energy dispersive spectroscopy spectra were obtained. f) Example EDS spectra.

composition of the growths was performed using a scanning electron microscope and energy dispersive spectroscopy (Sirion XL30 SEM, Oxford Instruments). Spectra were obtained at 20 distinct locations on the sample; the compositions reported throughout are the mean values of these spectra and the error bars represent one standard deviation of variability. These data are tabulated in Table 1.

2.2 Phase Diagram

All of the grown compositions were characterized through electrical transport measurements as described in the next section. The locations of the various phase transitions (antiferromagnetic, nematic, and superconducting) were identified through features in the resistivity versus temperature curves (Figure 2.2a) using methods described previously[104,110]. T_s and T_N are defined through extremums in the first and second temperature derivatives, and T_c is defined by the 50% normal state resistivity criterion. Using these values, I construct the temperature-composition (*T*-*x*) phase diagram (Figure 2.2b) which matches well with previous reports.

Growth ID	Composition *x*	Growth ID	Composition *x*
JC 703	0	JC 1148	0.0744 ± 0.0027
JC 322	0	JC1794	0.0747 ± 0.0050
JC 69	0.0269 ± 0.0028	JC1795	0.0753 ± 0.0060
JC 783	0.0356 ± 0.0025	JC 1113	0.0796 ± 0.0031
JC 799	0.0395 ± 0.0018	JC 1149	0.0813 ± 0.0036
JC 64	0.0407 ± 0.0023	JC 578	0.0841 ± 0.0032
JC 800	0.0424 ± 0.0018	JC 1150	0.0959 ± 0.0029
JC 67	0.0548 ± 0.0033	JC 810	0.1049 ± 0.0028
JC 148	0.0593 ± 0.0026	JC 1151	0.1059 ± 0.0028
JC 149	0.0633 ± 0.0035	JC 1152	0.1082 ± 0.0026
JC 1147	0.0656 ± 0.0022	JC 1209	0.1227 ± 0.0027
JC 628	0.0677 ± 0.0038	JC 1210	0.1440 ± 0.0080
JC1793	0.0718 ± 0.0050	JC 1211	0.2043 ± 0.0060

Table 2.1. Summary of growths of $Ba(Fe_{1-x}Co_x)_2As_2$.

2.3 Electrical Transport

Electrical transport measurements were performed using a standard 4, 5, or 6 contact point configuration. Electrical contacts were made to the sample by first sputtering the contact pattern with gold using a hand-made paper mask and gold sputterer with argon atmosphere (108 Manual Sputter Coater, Cressington Scientific Instruments). Electrical leads in the form of 25-micron diameter gold wire were attached to the pre-patterned contacts by hand using silver epoxy (H20E Epo-Tek, Epoxy Technology) following a curing schedule of heating the sample on a hot plate at 175° C for ~15-30 minutes. Typical 2-point contact resistances measured via multimeter were 1-5Ω. All measurements were made using lock-in techniques (SRS 830/860 Lock-In Amplifier, Standard Research Systems) with a preamplifier to reduce noise (SR554 Transformer Preamplifier, Standard Research Systems) under a constant excitation current of 1 mA and frequency ~ 110 Hz (CS580 Voltage Controlled Current Source, Standard Research

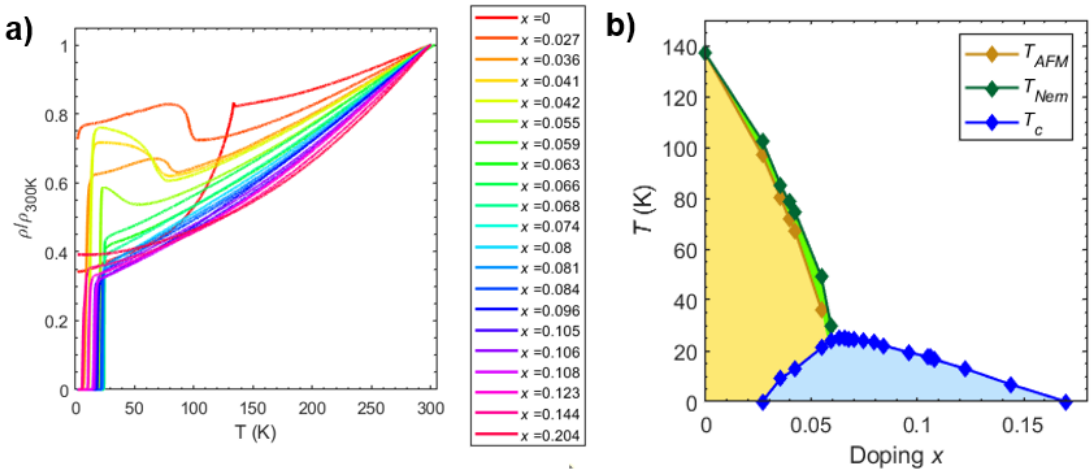

Figure 2.2 a) Resistivity as a function of temperature, normalized by the room temperature value, for all compositions of $Ba(Fe_{1-x}Co_x)_2As_2$ b) Temperature-composition phase diagram derived from the transport data in (a) and marking the phase boundaries of nematicity (green), antiferromagnetism (yellow), and superconductivity (blue).

Systems) using a PPMS Dynacool (Quantum Design) allowing for continuous temperature control between ~2K and 300K.

2.4 Application of Stress and Strain

2.4.1 Uniaxial Stress Device

Uniaxial stress was applied using home-built devices following previous designs[112]. This type of device (Figure 2.3) consists of a titanium bridge and backing piece attached to three piezo-electric actuators (3 x 3 x 9mm PICMA Stack P-883.11, Physik Instrumente). The piezo-electric actuators were driven with a high voltage source (Keithley 2400, Tektronix). The sample is glued (Loctite Stycast 2850FT) across the gap in the titanium bridge, and uniaxial stress is applied to the sample by driving the piezo-electric actuators and modulating the size of the gap.

This type of design offers a number of practical advantages. The piezo-electrics naturally expand along their poling axis as they cool, which would result in a large thermally induced strain if the sample were affixed directly to the surface of the piezo. The symmetric arrangement of the piezo stacks in the uniaxial stress cell design eliminates this thermal strain because all the piezo stacks expand equally, displacing the entire bridge piece. However, there is still a thermal strain that results from the differential thermal contraction between the titanium and the sample. This effect is relatively small and can be easily compensated within the voltage ranges tolerated

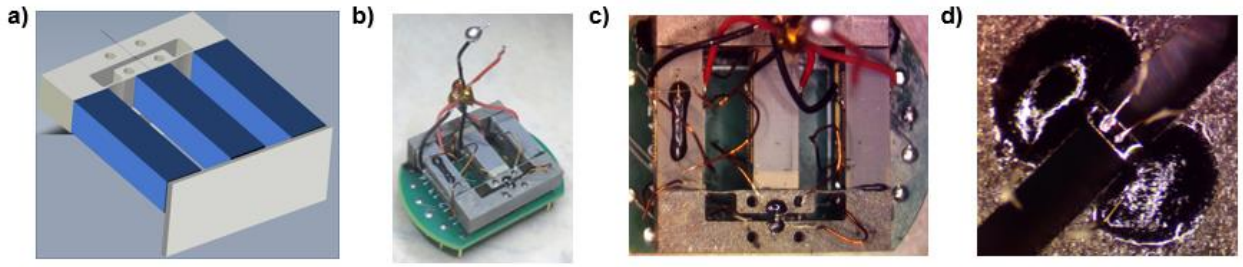

Figure 2.3. Uniaxial stress cell. a) Uniaxial stress cell schematic. Blue prisms are the piezoelectric stacks, and the gray pieces are the components of the body and bridge piece. b) Image of the actual device mounted on a PPMS chip c) Top view of the actual device d) Image of the sample mounted across the gap with electrical leads attached.

by the piezo stacks. This is facilitated by another advantage of the present setup; the full displacement of the piezo stacks is delivered to the sample, resulting in a mechanical advantage factor of the length of the piezo divided by the gap length that amplifies the strain applied to the sample. This allows for both compressive and tensile applied strains >1% even at cryogenic temperatures.

The applied strain is monitored via a four-point measurement on silicon resistive strain gauges (SS-150-124-15PB, Micron Instruments) affixed to the back of the piezo stacks. These strain gauges are extremely sensitive but have a temperature dependent gauge factor (strain-induced change of resistance) which was calibrated by comparing to strain gauges with a temperature independent gauge factor (SGD-10/350-LY11, Omega). The silicon gauge factor as a function of temperature is given by $gf = 165.4 - 0.32T$, with temperature measured in Kelvin. Determination of the change of the gap size is not sufficient to determine the applied strain to the sample due to both imperfect strain transmission and the differential thermal strain. The former is estimated either by finite element analysis[113] or is left as a strain transmission factor. The latter requires an independent determination of the zero-strain point. For $Ba(Fe_{1-x}Co_x)_2As_2$, this is easily achievable because the resistivity is extremely sensitive to strain. Before any measurement on the stress cell, the full temperature dependence of the "freestanding" (zero-strain) resistivity was measured. Once on the stress cell, the zero-strain point was then determined by sweeping the piezo-stack voltage until the resistance matches the freestanding value at a given temperature. Then, the applied strain was determined as follows:

$$\epsilon_{applied}(V) = 2 * \mu * \frac{L_{piezo}}{L_{gap}} * \frac{R_{SG}(V) - R^1_{SG}}{R^0_{SG} * SG_{gf}} \quad (2.1)$$

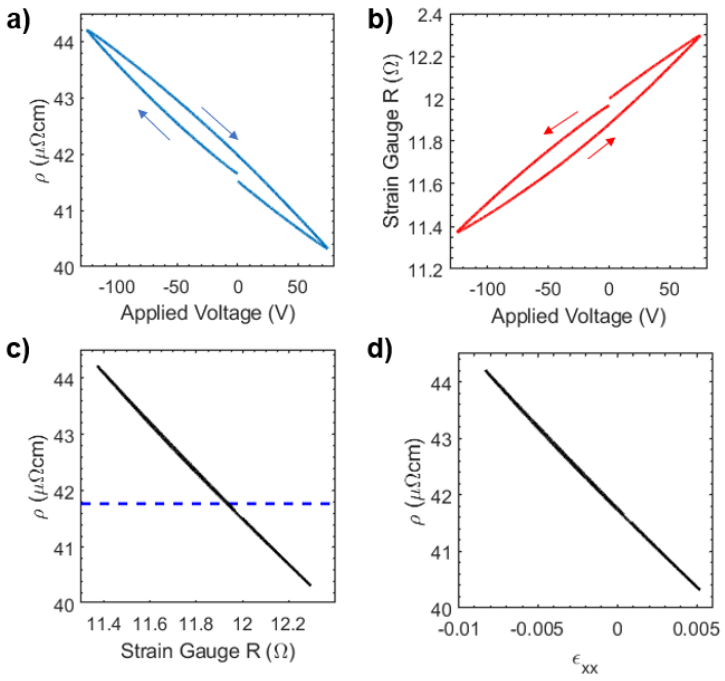

Figure 2.4. Determination of applied strain. a) Sample resistivity and b) strain gauge resistance as a function of piezo stack voltage. Arrows indicate the direction of the voltage sweep. c) Sample resistivity as a function of the strain gauge resistance, which eliminates the hysteresis of the piezo stacks as a function of voltage. The blue dotted line indicates the value of the freestanding sample resistivity which determines the zero-strain point. d) Sample resistivity versus the calculated applied strain.

Here μ is the strain transmission factor, L_{piezo} and L_{gap} are the lengths of the piezo (9 mm) and the gap when the sample is glued (500-600 μm) respectively, $R_{SG}(V)$ is the strain gauge resistivity as a function of voltage, R_{SG}^{1} is the strain gauge resistivity at the zero-strain point, R_{SG}^{0} is the freestanding strain gauge resistivity, and SG_{gf} is the strain gauge factor. An example of this procedure is demonstrated in Figure 2.4.

The samples were cleaved and shaped by hand using a scalpel. $Ba(Fe_{1-x}Co_x)_2As_2$ naturally breaks along the [100] and [010] crystallographic directions when cleaved, which allows the sample to be shaped by eye into a bar shape with the long direction either along [100] or [110], appropriate for applying uniaxial stress along each of these directions.

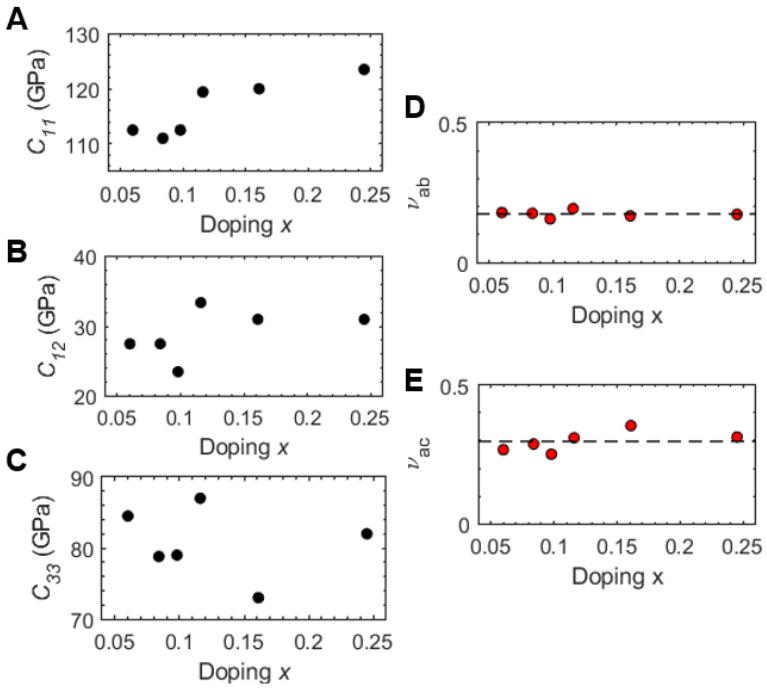

Figure 2.5. Doping dependence of elastic constants in $Ba(Fe_{1-x}Co_x)_2As_2$ A-C) Elastic constants C_{11}, C_{12}, C_{33} at T = 30K versus doping[114] x D, E) Poisson ratios ν_{ab}, ν_{ab} calculated from the data in (A-C). Horizontal lines show the values are relatively doping independent.

2.4.2 Irreducible Components of Strain

With the application of uniaxial stress, multiple irreducible strain components are induced dictated by the Poisson ratios of the materials (see also Section 1.5). For uniaxial stress along [100], both A_{1g} and B_{1g} strain are induced, while for stress along [110], A_{1g} and B_{2g} strains are induced. We can write the irreducible components in terms of the strain measured along the direction of applied stress (ϵ_{xx}):

$$\epsilon_{B1g/B2g} = \frac{1}{2}(\epsilon_{xx} - \epsilon_{yy}) = \frac{1}{2}(1 + \nu_{ab})\epsilon_{xx} \quad (2.2)$$

$$\epsilon_{A1g,1} = \frac{1}{2}(\epsilon_{xx} + \epsilon_{yy}) = \frac{1}{2}(1 - \nu_{ab})\epsilon_{xx}$$

$$\epsilon_{A1g,2} = \epsilon_{zz} = -\nu_{ac}\epsilon_{xx}$$

For the Poisson ratios relevant for uniaxial stress along [100], the contributing elastic constants are largely temperature independent, allowing for the calculation of these Poisson ratios easily from published elastic constant data[114]. These are shown in Figure 2.5 and are seen

to be relatively doping independent. For stress along [110], the strong temperature dependence of the elastic constant C_{66} due to the nematic instability prevents such a simple comparison. Thus, in the following Chapters we will either calculate these at a given temperature or the Poisson ratio will be left as a temperature dependent factor.

2.5 X-ray Diffraction

The x-ray diffraction measurements presented in Chapter 3 were performed at Beamline 6-ID-B of the Advanced Photon Source at Argonne National Laboratories using high energy synchrotron x-rays with energy 11.215 keV and a wavelength of 1.10552 Å. The uniaxial stress cell (here the commercial version was used, Razorbill CS100) was mounted on the cold finger of a closed cycle cryostat allowing for temperature control between 300K and ~7K with a beryllium window cap allowing for transmission of x-rays. Electrical leads mounted on the underside of the sample were made to facilitate electrical transport without blocking the path of the x-rays. Overall, this sample environment allows for simultaneous electrical transport and x-ray diffraction as a function of uniaxial stress.

The x-ray beam spot illuminated a ~500 μm x 500 μm spot on the sample encompassing the central part of the sample across the gap. By monitoring three different Bragg peaks referenced to the tetragonal lattice, the full set of lattice constants as a function of strain were determined through Gaussian fits to the intensity versus θ scans.

3. Suppressing Superconductivity with Anisotropic Strain

3.1 Introduction and Motivation

In this chapter I present electrical transport, magnetic susceptibility, and x-ray diffraction measurements of $Ba(Fe_{1-x}Co_x)_2As_2$ as a function of uniaxial stress inducing strain in the same symmetry channel as the electronic nematic order and will demonstrate that this type of strain has a drastic effect on the superconductivity. For an underdoped sample where nematic and magnetic order are present at zero applied strain and coexist with superconductivity, T_c can be tuned all the way to zero through a strain-tuned superconductor to metal transition. Near optimal doping, T_c is reduced nearly fivefold from its original value of 25K with applied strains on the order of 1%. The implications of these results are twofold. First, they are strong evidence for the importance of nematic fluctuations in the formation of the high T_c unconventional superconductivity in this compound. Second, they reveal a remarkable sensitivity of superconductivity to mechanical deformation which has potential technological implications independent of the microscopic physical mechanism. The results presented in this chapter are published previously[113].

As discussed in Chapter 1, unconventional superconductivity is often found when a competing symmetry broken phase is suppressed towards zero temperature via an external tuning parameter, which suggests that the fluctuations of the competing phase are involved in or responsible for the superconducting pairing. A more direct verification of this scenario is to directly tune the competing order in a single sample by applying the conjugate field to the competing order. This will suppress the fluctuations, and by observing how the superconducting T_c responds, one can infer how the superconductivity and the fluctuations of the competing order are related. However, most examples of the competing order, namely antiferromagnetic states, break translational symmetry which implies a conjugate field that varies spatially on microscopic scales which is difficult or impossible to implement experimentally. Electronic nematic order is unique in this regard in that it is a wave-vector $\boldsymbol{q} = 0$ collective state and only breaks rotational symmetry. Due to symmetry and electron-lattice coupling, the nematic transition triggers an orthorhombic distortion of B_{2g} symmetry as a secondary order parameter. Importantly, x-ray diffraction measurements demonstrated that the orthorhombicity is reduced below T_c[67], direct

evidence for competition between superconductivity and static nematic order. Above the transition, applied strain in this symmetry channel acts as the conjugate field to nematic order, linearly coupling to nematicity. Thus, the applied strain enhances the nematic order parameter and all associated anisotropies, and also suppresses nematic fluctuations. In particular, measurement of the resistivity anisotropy induced by anisotropic strain allows one to measure the diverging nematic fluctuations, which have been found to be ubiquitously present and large near optimal doping for a variety of families of Fe-based superconductors[51], suggesting that strong nematic fluctuations may be somehow responsible or involved in the high T_c superconducting pairing.

This hypothesis also has support from a variety of theoretical considerations. In particular, quantum Monte Carlo simulations have demonstrated that an Ising-like nematic order tuned through a quantum critical point generates a superconducting dome around the QCP[98]. An important feature of this scenario is that due to its $\boldsymbol{q} = 0$ nature, the fluctuations of nematic order enhance the superconducting pairing strength in all symmetry channels[97]. Thus, even if the pairing mechanism originates from exchange of spin fluctuations or some other form of attraction, it is possible that nematic fluctuations play a key role in boosting the strength of the pairing to higher temperatures. An explicit experimental realization[115] of this was demonstrated in the system $Ba_{1-x}Sr_xNi_2As_2$, a nickel-based analogue of the Fe-based superconductors which exhibits no ordered magnetic states but has long-range charge density wave order and low temperature conventional superconductivity. In this system, it was found that diverging nematic fluctuations are present, possibly arising from charge fluctuations associated with the tetragonal-symmetry breaking charge density wave, and that there is a six-fold enhancement of the superconducting T_c upon tuning the system through a nematic quantum critical point.

Motivated by these ideas, the purpose of the measurements in this chapter is to investigate how the superconductivity in $Ba(Fe_{1-x}Co_x)_2As_2$ responds to uniaxial stress that induces the symmetry-breaking strain ϵ_{B2g} which directly couples to and enhances nematic order and suppresses nematic fluctuations. Details on the uniaxial stress device, strain determination, and electrical transport measurements are described in Chapter 2. In this chapter, ϵ_{disp} refers to the strain along the direction of applied stress, which in this case is $[110]_{tet}$, where the 'tet' subscript designates that the Miller indices are referenced to the normal state tetragonal lattice.

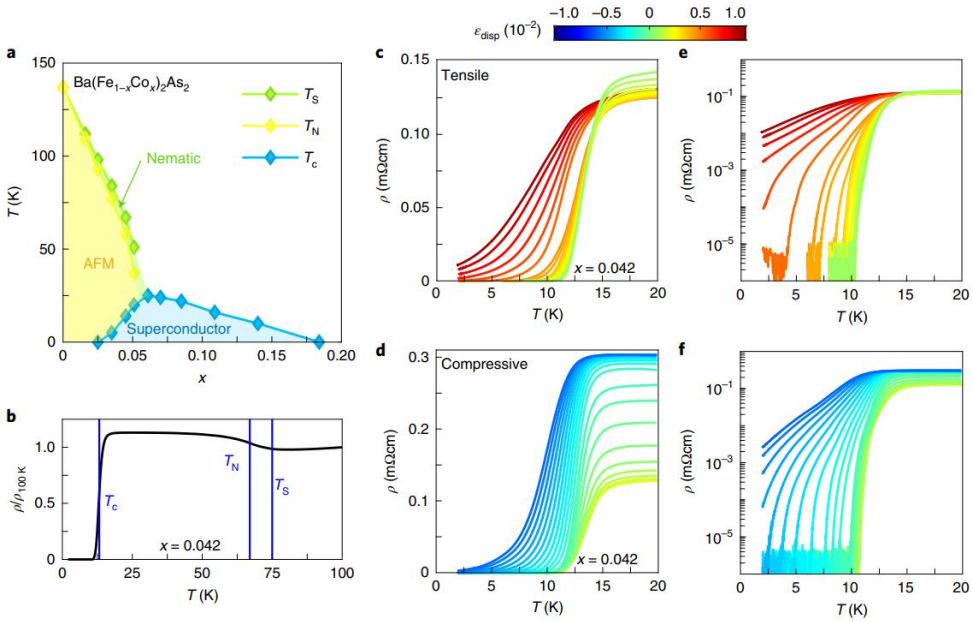

Figure 3.1. Superconducting transition in $Ba(Fe_{0.958}Co_{0.042})_2As_2$ under uniaxial stress along $[110]_{tet}$ a) Composition-temperature phase diagram of $Ba(Fe_{1-x}Co_x)_2As_2$. Green, yellow, and blue regions are the nematic, antiferromagnetic, and superconducting phases respectively. b) Temperature dependence of the resistivity of the $x = 0.042$ composition. Blue vertical lines indicate the location of the phase transitions described in a. b, c) Resistivity versus temperature through the superconducting transition for fixed amounts of applied positive (c) and negative (d) uniaxial stress. Corresponding value of ϵ_{disp} is indicated by the color bar. e, f) Same data as c, d with resistivity plotted on a logarithmic scale.

3.2 Strain-Tuned Superconductor-Metal Transition

I begin with an underdoped composition of $Ba(Fe_{1-x}Co_x)_2As_2$ with $x = 0.042$. According to the x-T phase diagram (Figure 3.1a), this sample undergoes both the nematic and magnetic phase transitions before entering the superconducting state. These transitions are identifiable by signatures in the temperature dependence of the resistivity (Figure 3.1b) which gives $T_s \sim 74$K, $T_N \sim 67$K, and $T_c \sim 13$K. This implies that application of uniaxial stress along $[110]_{tet}$ will enhance nematic order and orthorhombic distortion that are already present in the zero-strain state.

Figure 3.1c-d shows the resistivity of the sample as a function of temperature for different amounts of fixed uniaxial stress. By applying both positive and negative stress, both tensile and compressive strains can be induced. For small values of strain (green curves), the superconducting transition is relatively unaffected while the resistivity above the transition is modulated by a

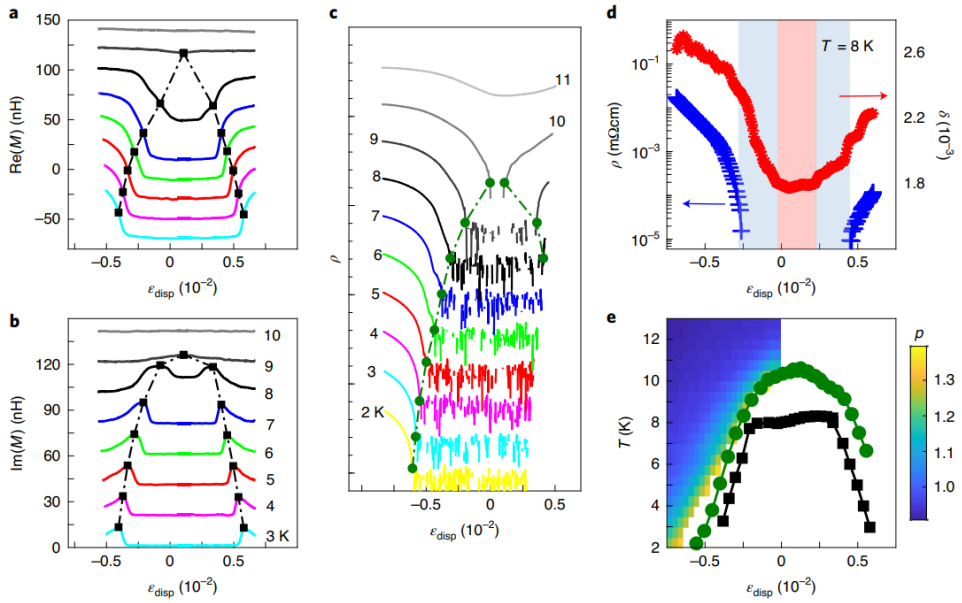

Figure 3.2 Strain-tuned superconductor to metal transition in $Ba(Fe_{0.958}Co_{0.042})_2As_2$. a) Real and b) imaginary components of the susceptometer coil signal as a function of applied strain at different temperatures. Data at different temperatures are offset for clarity. Black squares demarcate the thermodynamic signature of the superconductor-metal transition. c) Resistivity on a logarithmic scale as a function of variable strain at different temperatures offset for clarity. Green circles demarcate the onset of finite resistivity. d) Resistivity (blue, left) and structural orthorhombicity (red, right) at T = 8K as a function of variable strain. e) Strain-temperature phase diagram for $Ba(Fe_{0.958}Co_{0.042})_2As_2$. Color bar gives the power law dependence of the I-V relation $V \sim I^p$.

large factor. Due to the presence of static nematic order, structural twin domains are present near zero strain and applied stress acts to reorient these domains while leaving each individual domain unstrained. These domains mask anisotropies at zero-strain and are only fully developed when all structural domains are oriented in the same way. Thus, we can understand the variation of the resistivity that is observed as a development of the large resistivity anisotropy induced by nematic order[45], becoming more prominent as the domain imbalance increases. These domain dynamics as a function of uniaxial stress will be verified by x-ray diffraction and discussed below.

For higher values of strain (red and blue curves), the resistivity varies much less rapidly, indicating that the structural domains have fully oriented, and any additional applied stress causes true microscopic structural distortion. At these values of strain, the superconducting transition is rapidly suppressed to lower temperatures for both compressive and tensile strain. Strikingly, for the largest values of strain, a non-zero resistivity is observed for the lowest accessible temperatures ~2K, which is readily seen by plotting the resistivity on a log scale

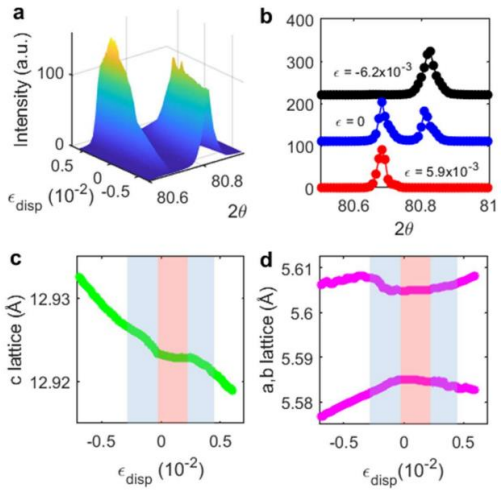

Figure 3.3. X-ray diffraction measurements under uniaxial stress in the x = 0.042 composition at T = 8K. a) Scattering intensity near the $(2\ 2\ 12)_{tet}$ Bragg peak versus applied strain. b) 2θ scan of the $(2\ 2\ 12)_{tet}$ peak under compressive (black), zero (blue), and tensile (red) strain. c) c-lattice constant and d), a, b -lattice constants as a function of applied strain. Red region indicates values of strain where structural detwinning is occurring and the lattice constants are unchanged. Blue region indicates the additional strain necessary to induce a finite resistivity.

(Figure 3.1e-f). An important feature of the resistivity temperature dependence is that the transition exhibits significant broadening for non-zero strains. Inspection of the curves in Figure 3.1 shows that the temperature where the sample reaches zero resistivity is much more sensitive to the applied strain compared to the onset of the transition which raises the question of how to properly define the phase boundary of the superconducting state.

To investigate where the bulk thermodynamic superconducting transition occurs, I now present magnetic susceptibility measurements as a function of uniaxial stress (these measurements follow previous methods used for Sr_2RuO_4[116]). A bulk superconductor exhibits the Meissner effect where an applied magnetic field is expelled from the interior of the sample, which is reflected in the magnetic susceptibility, $\chi = \chi' + i\chi''$, where the primed and unprimed terms are the real and imaginary components of the susceptibility. Figure 3.2a-b shows the real and imaginary components of the susceptometer coil signal in response to a ~5 Oe 100 Hz oscillating applied field at different fixed temperatures and variable amounts of compressive and tensile strain. At T = 10K, both the real and imaginary components of the signal are nearly zero and unchanged with applied strain, indicating the sample is above the bulk superconducting transition for all values of strain. At lower temperatures, the real component develops a negative value near zero-strain, consistent with a diamagnetic superconducting Meisner screening state.

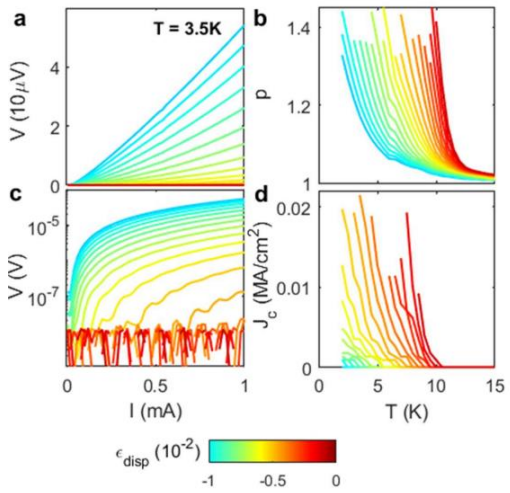

Figure 3.4. Nonlinear *I-V* characteristics and critical currents as a function of strain for the $x = 0.042$ composition. a) Characteristic set of *I-V* curves showing nonlinear behavior near the $\rho = 0$ phase boundary. b) Temperature and power dependence of the power p defined as $V \sim I^p$. c) Same as a) with voltage on a log scale demonstrating suppression of the critical current with increasing strain. d) Temperature and strain dependence of the superconducting critical current density.

This diamagnetism is suppressed via the application of both tensile and compressive strain with a temperature dependent amount of strain required, and the midpoint of this transition is accompanied by a sharp peak in the imaginary component of the signal which is a dissipative signature of the superconducting transition. In contrast to resistivity, this is a thermodynamic, more bulk-sensitive measurement, and thus strong evidence that we are truly suppressing the bulk superconductivity with applied strain. This behavior is mirrored in the resistivity as a function of variable strains for fixed temperatures (Figure 3.2c) where a resistive onset is induced by both compressive and tensile strain. Additionally, a strain-induced suppression of the critical currents and nonlinear *I-V* characteristics to lower temperatures are observed (Figure 3.4) providing further evidence of the sensitivity of the superconductivity to the applied strain.

In order to directly track the strain induced structural changes microscopically, x-ray diffraction measurements were performed at Beamline 6-ID-B in the Advanced Photon Source at Argonne National Laboratory utilizing a sample environment allowing for simultaneous electrical transport, x-ray diffraction, and application of uniaxial stress (see Experimental Methodology, Chapter 2 and also[52]). The presence of the structural twin domains manifest as a splitting of the (*H K L*) tetragonal Bragg peaks for nonzero *H*, *K*. By tracking three different Bragg peaks ($(2\ 2\ 12)_{tet}$, $(-1\ 1\ 14)_{tet}$, and $(0\ 0\ 14)_{tet}$), both the in-plane orthorhombic *a*, *b* lattice constants and the out-of-plane *c* lattice constant were determined as a function of the applied

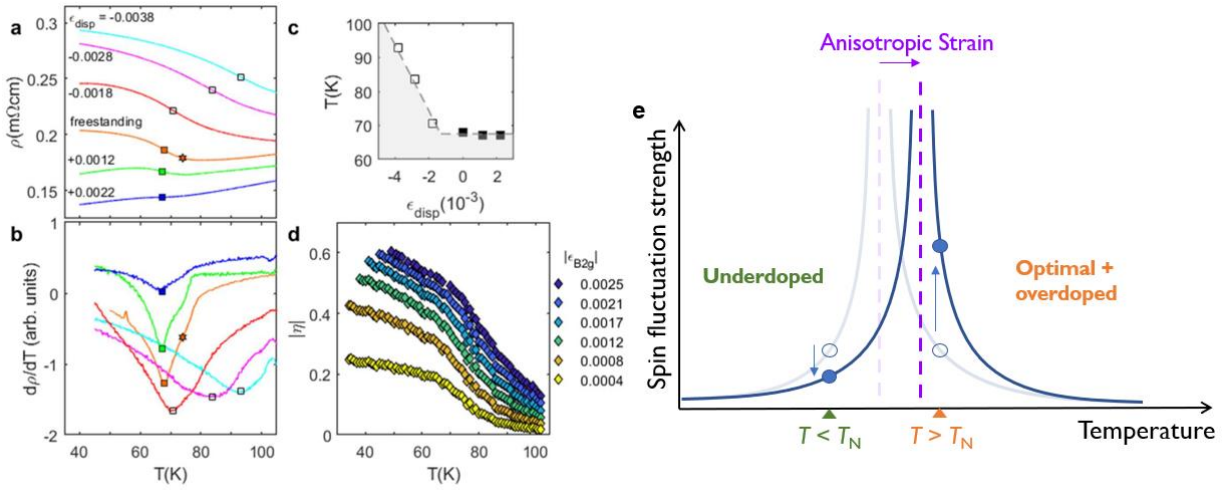

Figure 3.5. Effect of strain on nematic and magnetic order. a) Resistivity of the x = 0.042 composition as a function of temperature under different applied strains. Squares demarcate the location of the magnetic transition temperature identified through the temperature derivative shown in b) Orange star marks the zero-strain nematic transition temperature. c) Extracted T_N as a function of applied strain. d) Resistivity anisotropy η which is a proxy for the nematic order parameter as a function of temperature and the anisotropic strain ϵ_{B2g}. e) Schematic of the effect of anisotropic strain on the spin fluctuation spectrum (blue line). The magnetic transition temperature (purple dashed line) is enhanced by strain. The blue circles indicate the strength of spin fluctuations which is increased (decreased) at temperatures above (below) the zero-strain T_N.

stress. Figure 3.3a shows that the splitting of the $(2\ 2\ 12)_{tet}$ peak is controlled by the applied strain, with each of the different domain types being favored by either compressive or tensile strain, and with sufficient strain the domains are oriented completely resulting in a single peak. Within the detwinning region, the lattice constants are unchanged, but once a monodomain is achieved the lattice begins to distort (Figure 3.3c-d). By tracking the strain dependence of the lattice constants, the strain dependence of the structural orthorhombicity ($\delta = (a + b)/(a - b)$) is determined. As discussed previously, this quantity can be viewed as a secondary order parameter of the nematic phase. In Figure 3.2d I show both δ and the resistivity as a function of strain, demonstrating that the onset of nonzero resistivity is correlated with the enhancement of δ, and thus of nematic order, under uniaxial stress. These diffraction measurements also reveal that the width of the Bragg peaks is comparable for zero strain and applied strain (Figure 3.3b), attesting to high strain homogeneity within the sample region we are probing. This suggests that the smeared transition observed in the resistivity is not attributable to macroscopic strain inhomogeneity, but in fact has an intrinsic origin.

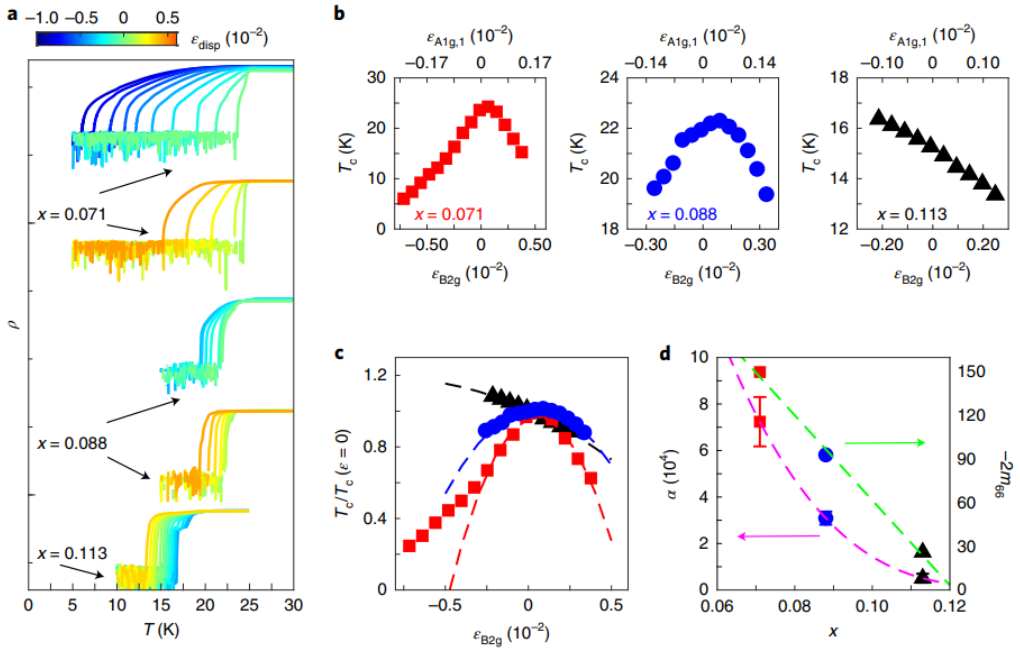

Figure 3.6. Superconducting transition under uniaxial stress along $[110]_{tet}$ for optimal and overdoped compositions. a) Resistivity on a logarithmic scale as a function of temperature with the value of applied strain given by the color bar. Curves for different compositions and the curves under tensile and compressive strain for the x = 0.071 and x = 0.088 are offset for clarity. b) Extracted T_c given by the zero-resistivity criterion as a function of the calculated irreducible strain components. c) Normalized change in T_c as a function of the anisotropic strain ϵ_{B2g}. Dotted lines are second order polynomial fits. d) Quadratic coefficient α (left) and elastoresistivity coefficient $-2m_{66}$ just above T_c (right) as a function of composition. Dotted lines are guides to the eye.

All of the data presented in this section can be unified in a single ϵ_{disp}-T phase diagram which is shown in Figure 3.2e. This diagram demonstrates that the applied strain generates a dome shaped phase boundary within which the sample is a bulk superconductor, while outside the transport and thermodynamic signatures of superconductivity are eliminated and linear Ohmic electrical transport is recovered. Importantly, the zero-resistivity criterion for T_c closely follows the thermodynamic criterion determined from the magnetic susceptibility. Furthermore, extrapolation of the phase boundary to zero temperature implies that strains on the order of 0.5% tune a superconductor to metal quantum phase transition.

3.2 Optimally and Overdoped Compositions

The efficiency with which T_c is suppressed by uniaxial stress enhancing nematic order in the underdoped sample is consistent with the hypothesis that nematic fluctuations have a role in the superconducting pairing and thus in the determination of T_c. However, because this

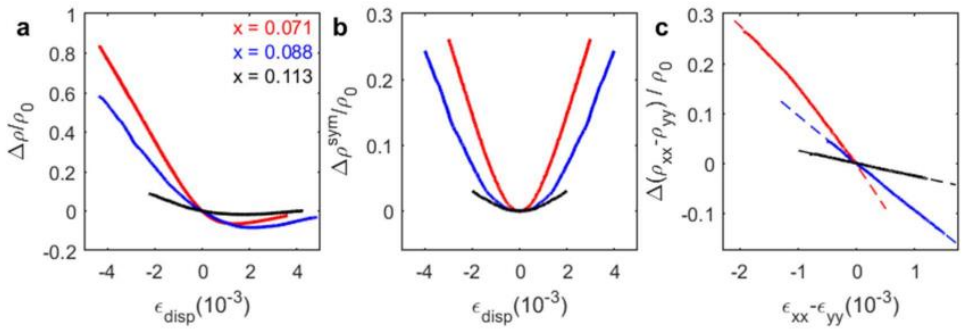

Figure 3.7. Elastoresistivity of the optimal and overdoped compositions at T = 27K. a) Normalized strain-induced change of the resistivity. b) Normalized change of the average in-plane resistivity. c) Resistivity anisotropy induced by anisotropic strain. Dotted lines are polynomial fits which allow for extraction of the elastoresistivity coefficient $-2m_{66}$.

composition hosts static magnetic order, a suppression of nematic fluctuations is not the only effect expected to be induced by anisotropic strain. Both neutron scattering and NMR measurements under uniaxial stress have shown that the magnetic transition temperature is enhanced by strain increasing the orthorhombic distortion. Indeed, by measuring the resistivity temperature dependence under strain (Figure 3.5a-d), it is observed that the resistive signature of the magnetic phase transition, and thus the transition temperature T_N, is enhanced by strain. This occurs simultaneously with a smearing out of the nematic transition and an enhancement of the nematic order parameter measured by the strain induced resistivity anisotropy.

This strengthening of magnetic order presumably is accompanied by an increase in the number of gapped carriers, leaving less available for superconductivity. Furthermore, enhancing magnetic order in the ordered phase will lead to a suppression of the stripe-type spin fluctuations (Figure 3.5e) which are also likely involved in the superconducting pairing, and we cannot disentangle the contributions of simultaneously weakening spin and nematic fluctuations. These two facts prevent any definite attribution of the observed suppression of superconductivity to the strength of nematic fluctuations.

The situation is different, however, if we consider optimally or overdoped samples. In this case there is no static magnetic or nematic order for all temperatures, although neutron and NMR show that strongly temperature dependent stripe-type spin fluctuations are still present. In contrast to the underdoped case, now that we are in the magnetically disordered phase, anisotropic strain is expected to increase the strength of the spin fluctuations (Figure 3.5e) while nematic fluctuations will still be suppressed because we are applying the conjugate field. In this

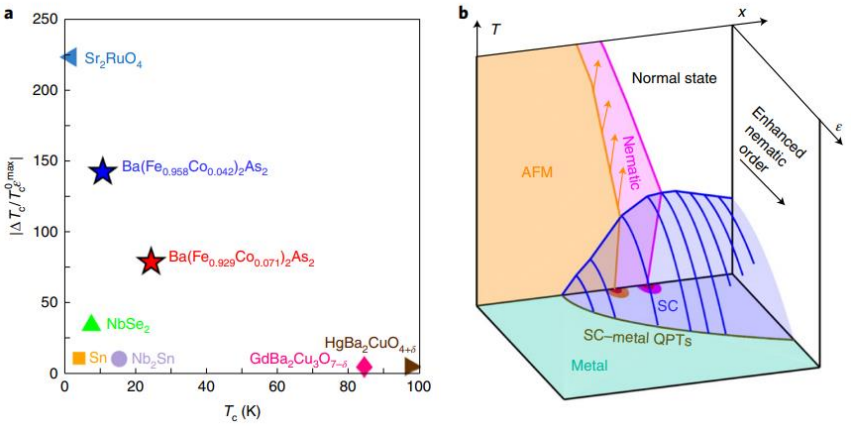

Figure 3.8. Strain tunability of T_c. a) Strain-sensitivity of superconductivity for a variety of compounds. The vertical axis is the maximum achievable change in T_c by lattice deformation normalized by strain and the zero-strain T_c. b) Schematic doping-strain-temperature phase diagram for $Ba(Fe_{1-x}Co_x)_2As_2$. The electronic nematic phase is shown in magenta and ends in a putative QCP beneath the superconducting dome (blue region). Antiferromagnetism is shown in orange and is enhanced by anisotropic strain (orange arrows) and also possibly ends in a QCP. At a fixed doping, symmetry breaking strain enhancing the nematic phase efficiently suppresses T_c, generating another superconducting dome tuned by strain instead of doping. These strain-tuned domes result in a metallic ground state (green region) and generate a line of superconductor to metal quantum phase transitions (green line).

case, any observed changes in T_c as a function of uniaxial stress cannot be attributed to an enhancement of magnetic order.

In Figure 3.6a I show the resistivity as a function of temperature under uniaxial stress for a near-optimally doped (x = 0.072) and two overdoped (x = 0.088, x = 0.113) compositions. Remarkably, the superconducting transition of the optimally doped sample is drastically suppressed by both tensile and compressive strain, and for the highest value of compressive strain ~ -1% the resistivity only becomes zero near T = 5K, a fivefold reduction from the zero-strain T_c ~ 25K. For the x = 0.088 sample, the response is reduced in magnitude but still symmetric for positive and negative strain, while for the x = 0.113 sample the symmetric behavior disappears, with compressive (tensile) strain increasing (decreasing) T_c.

As described in Chapter 1, for the D_{4h} point group of these samples, uniaxial stress along [110] induces both symmetry-breaking ($\epsilon_{B2g} = {}^1/_2\,(\epsilon_{xx} - \epsilon_{yy})$) and symmetry-preserving ($\epsilon_{A1g,\,1} = {}^1/_2\,(\epsilon_{xx} + \epsilon_{yy})$, $\epsilon_{A1g,\,2} = \epsilon_{zz}$) components of strain. The superconducting T_c is a scalar and thus must be even under all rotations and reflections. By symmetry, we then have the following dependence of T_c on strain to lowest order:

$$T_c(\epsilon) = T_c^0(1 + \beta\epsilon_{A1g} - {}^1/_2\,\alpha\epsilon_{B2g}^2) \qquad (3.1)$$

In Figure 3.6b I show the extracted T_c (defined by onset of non-zero resistivity) plotted versus the distinct symmetry components of strain (see Chapter 2 for details), demonstrating a strong doping dependence in which the large quadratic response of the optimal doping which indicates that the response is dominated by ϵ_{B2g} crosses over to a primarily linear response in the overdoped region of the phase diagram. The linear response in the overdoped indicates that the response is now dominated by ϵ_{A1g}; in Chapter 4, I will investigate how this response to the non-symmetry breaking strain evolves across the superconducting dome. Here, by normalizing by the zero-strain T_c^0, plotting T_c versus the purely antisymmetric ϵ_{B2g}, and fitting a second order polynomial (Figure 3.6c), I extract the coefficient α which is plotted as a function of doping in Figure 3.6d which clearly shows a rapid increase of the sensitivity of superconductivity to ϵ_{B2g} on approach to optimal doping. On symmetry grounds, α should be directly proportional to the square of the nematic susceptibility $-2m_{66}$ which is measured by elastoresistivity measurements just above T_c (Figure 3.7). In Figure 3.6d I show that α does in fact exhibit a stronger doping dependence compared to $-2m_{66}$.

3.3 Discussion and Summary

The extreme sensitivity of T_c to ϵ_{B2g} near optimal doping is quite remarkable. Importantly, no signature of inducing static antiferromagnetic order is observed as a function of strain; the resistance just above T_c (Figure 3.7) evolves smoothly as a function of strain with no sharp feature indicating any phase transition. As discussed in the previous section, the fact that we remain in the magnetically disordered state implies a strengthening of spin fluctuations as a function of strain, which one might expect to lead to a higher T_c given that the spin fluctuations are the most likely candidate for the superconducting "glue" leading to Cooper pair formation. In fact, an observed quadratic increase of the average in-plane resistivity (Figure 3.7b) as a function of applied strain is consistent with an increased scattering from strengthened spin fluctuation in the normal state above T_c. However, a drastic suppression of T_c is still observed, providing evidence that the nematic fluctuations may be the essential ingredient for generating a high T_c. These conclusions are strengthened even further by a recent paper in which the authors investigated the evolution of nematic fluctuations as a function of strain directly using Raman spectroscopy[117] and found that the suppression of nematic fluctuations they observe agrees well with our published suppression of the superconducting T_c.

From a materials perspective and independent of the microscopic mechanism responsible for this behavior, the results presented in this chapter demonstrate an unprecedented tunability of a bulk superconducting material via lattice deformation. This mechanical control of switching superconductivity off and on by pulling and squishing on the material in symmetry-specific way could have potential utility in technological applications for superconductivity. To emphasize the uniqueness of the iron pnictides in this regard, in Figure 3.8a I show a compilation of the strain sensitivity of T_c for a broad group of both conventional and unconventional superconductors.

The dimensionless quantity that is being plotted is the maximum achievable change of T_c normalized by the zero-strain value as well as by the amount of applied strain required to induce the change. This quantity is ~ 100 in the underdoped and optimally doped $Ba(Fe_{1-x}Co_x)_2As_2$ samples, implying a 100% change of T_c with strains ~ 1%, which are both experimentally achievable as well as below the fracture limit of these materials. Additionally, these values are much larger than any other superconductor for which there is data available in the literature, with the exception of Sr_2RuO_4 where superconductivity is strongly affected by strain-induced changes of the proximity to a Van Hove singularity. However, Sr_2RuO_4 has a low transition temperature of T_c^0 ~ 1.5K and thus the unnormalized strain sensitivity is much lower than the iron pnictides. Additionally, in Sr_2RuO_4 T_c increases under strain which precludes realization of a superconductor to metal transition that is possible in the underdoped $Ba(Fe_{1-x}Co_x)_2As_2$.

The essential conclusions of this chapter are well illustrated in the form of a schematic composition-strain-temperature (x-ϵ-T) three-dimensional phase diagram that can be inferred from the experimental results which is shown in Figure 3.8b. For a broad range of composition in the underdoped and optimally doped regions of the phase diagram near the composition-tuned quantum critical point, the anisotropic component of applied strain which enhances the broken symmetry and suppresses nematic fluctuations efficiently suppresses superconductivity. This manifests as strain generating a "superconducting dome" in the ϵ-T plane and implies a line of superconductor to metal quantum phase transitions on extrapolation to zero temperature. Lastly, the magnitude of this effect decreases as you move to compositions further and further away from the region of the QCP.

As an outlook to future work, this demonstration that we can tune a superconductor to metal quantum phase transition in a bulk sample provides a platform for studying this type of

transition with a precise tuning parameter, as well as allowing for thermodynamic measurements which are not possible in the typical systems in which superconductor-metal or insulator QPTS are found, namely two-dimensional thin films or flakes. To further elucidate the relevant contributions of nematic and magnetic fluctuations, this work also motivates measurements of the electronic structure and magnetic fluctuation spectrum in the normal state above the superconducting dome as a function of strain and correlating the behavior with the observed changes to superconductivity. Lastly, a natural question is to determine to what extent the behavior observed here is a general phenomenon in the Fe-based superconductors, such as the hole and isovalent substituted iron pnictides or the iron chalcogenides where nematic order occurs in the absence of long-range magnetic order[58].

To summarize this chapter, I have presented electrical transport, magnetic susceptibility, and x-ray diffraction measurements as a function of uniaxial stress along $[110]_{tet}$ in $Ba(Fe_{1-x}Co_x)_2As_2$ which demonstrate that structural distortions enhancing electronic nematic order and suppressing its fluctuations are extremely antagonistic to superconductivity and allow a remarkable tunability of T_c. This is especially true in the underdoped case where a strain tuned superconductor to metal quantum phase transition is observed, as well as in compositions in the disordered phase near the nematic quantum critical point. I have argued that this phenomenology is consistent with nematic fluctuations playing an important role in the superconducting pairing mechanism. The next chapter will probe the effect on superconductivity of strains in different symmetry channels orthogonal to nematic order.

4. Quantum Critical Origin of Iron Pnictide Superconductivity

4.1 Introduction and Motivation

The previous chapter was concerned with the effects on superconductivity of uniaxial stress inducing strain components directly enhancing nematic order. In this chapter, I present electrical transport measurements of $Ba(Fe_{1-x}Co_x)_2As_2$ as a function of uniaxial stress along the [100] (or equivalently [010]) crystallographic direction which induces strains in symmetry channels *orthogonal* to the electronic nematic order. I will show that the dependence of the superconducting critical temperature T_c on composition and A_{1g} symmetry strains exhibits scaling behavior which is strong evidence for the scenario in which the superconducting dome follows the location of a quantum critical point, and thus is driven by quantum critical fluctuations. These results will also reveal that the superconductivity in $Ba(Fe_{1-x}Co_x)_2As_2$ is extremely tunable by A_{1g} strain in the heavily overdoped region of the phase diagram. The results presented in this chapter are currently in preparation to be published.

As discussed in Chapter 1, a ubiquitous feature of unconventional superconductivity is the presence of multiple intertwined broken symmetry states of matter. The most salient feature of this commonality is a shared phase diagram in which an ordered phase is tuned to zero temperature and a superconducting dome is generated around a putative quantum critical point. In spite of this generic phenomenology, central questions remain concerning the extent to which quantum criticality drives unconventional and high T_c superconducting pairing. The Fe-based superconductors demonstrate a unique versatility in that this common phase diagram can be induced by a range of qualitatively different tuning parameters, namely pressure, isovalent chemical substitution, and electron/hole carrier doping. Given that these tuning parameters naively affect microscopic features such as the Fermi surface, local crystal field environment, and magnetic fluctuation spectrum in different ways, an important question is to determine to what extent these are equivalent tuning parameters with respect to superconductivity and understanding the implications this has for understanding the connection between superconductivity and quantum critical fluctuations. In particular, a direct experimental demonstration of this connection has been lacking thus far.

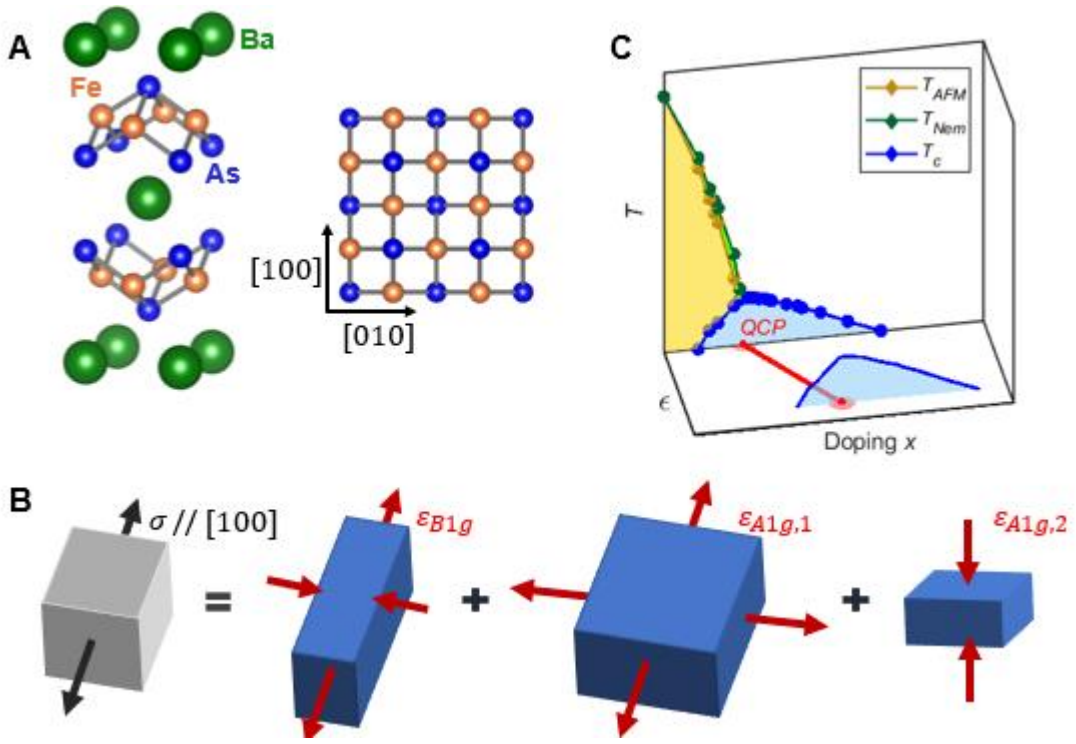

Figure 4.1. A) Crystal structure of $Ba(Fe_{1-x}Co_x)_2As_2$ B) Irreducible strain components induced by uniaxial stress along the [100] crystallographic direction C) Hypothesis demonstrated through a temperature (T), composition (x), and strains orthogonal to nematic order (ϵ) phase diagram. The superconducting dome follows the location of a quantum critical point (QCP) tuned by strain.

The mere presence of quantum criticality in the iron pnictides is supported by a number of experimental works. For example, doping dependence of the nematic transition temperature by elastoresistivity and the magnetic transition temperature by NMR measurements of the magnetic fluctuations show that T_s, $T_N \rightarrow 0$ K near optimal doping, suggestive of both nematic and magnetic quantum critical points. In the isovalent-substituted P-Ba122, electrical transport measurements show signatures of the "strange metal" phase within a quantum critical-like fan, such as linear-in-temperature resistivity and anomalous field and temperature dependence of the Hall resistivity[95,96]. As discussed in Section 1.4.4, quantum oscillation, specific heat, and penetration depth measurements also have shown that the effective mass of the conduction quasiparticles is enhanced on approach to the QCP, consistent with the quantum critical expectation that the critical slowing down induces a vanishing of the effective Fermi energy scale.

Another hallmark of quantum critical behavior is power-law scaling dependence of thermodynamic quantities on different non-thermal tuning parameters. On approach to the QCP,

the correlation lengths and times diverge, and the microscopic differences between different tuning parameters become unimportant. Instead, the behavior is determined by a single parameter g which tells the material how far it is away from the QCP. Recently, Worasaran et al[106]. investigated the dependence of the nematic transition temperature T_s on composition and strain in symmetry channels orthogonal to nematic order (ϵ_{B1g} and ϵ_{A1g}) and found that close enough to the putative nematic QCP, the data could all be described by a single power law. This is highly indicative of the presence nematic quantum criticality and the associated quantum critical fluctuations, and furthermore the region of these fluctuations is coincident with the range of underdoped compositions over which the material is superconducting. This is in line with theoretical and experimental considerations suggesting that nematic fluctuations enhance the superconducting pairing strength and T_c[97,98,118].

One way to view the results of Worasaran et al. is that the location of the QCP as a function of composition is shifted with the application of strain. In this work we investigate how the superconductivity responds to these types of structural changes. We find that ϵ_{A1g} and x are remarkably equivalent tuning parameters for superconductivity, exhibiting a scaling relationship that holds over a wide range of doping extending from optimal doping near the top of the dome deep into the overdoped region. This provides direct evidence that the superconducting dome follows the location of a quantum critical point beneath the dome (Figure 4.1C), and thus that the presence of superconductivity is driven by the presence of quantum critical fluctuations.

4.2 Doping Dependence of the Superconducting Transition for [100] Uniaxial Stress

As discussed in Chapters 1 and 2, $Ba(Fe_{1-x}Co_x)_2As_2$ crystalizes in the space group *I4/mmm* with FeAs planes separated by Ba spacer ions and has tetragonal D_{4h} symmetry (Figure 4.1A). For uniaxial stress applied either [100] or [010], which is the relevant configuration for this work, strains along all three principal axes will be induced with a magnitude determined by the relevant Poisson ratio. For the D_{4h} point group, these strains can be organized into irreducible components as follows (Figure 4.1B):

$$\epsilon_{B1g} = \frac{1}{2}\left(\epsilon_{xx} - \epsilon_{yy}\right) = \frac{1}{2}(1 + \nu_{ab})\epsilon_{xx} \qquad (4.1)$$

$$\epsilon_{A1g,1} = \frac{1}{2}\left(\epsilon_{xx} + \epsilon_{yy}\right) = \frac{1}{2}(1 - \nu_{ab})\epsilon_{xx} \qquad (4.2)$$

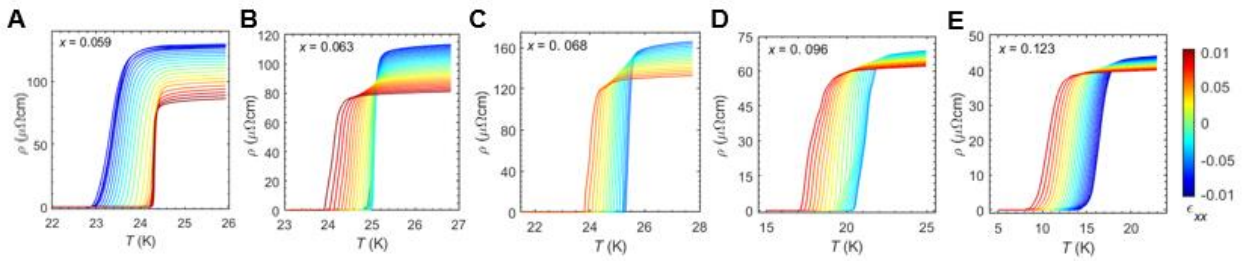

Figure 4.2. Superconducting transition with σ // [100] for five representative dopings of $Ba(Fe_{1-x}Co_x)_2As_2$. Value of applied strain is given by the color bar.

$$\epsilon_{A1g,2} = \epsilon_{zz} = -\nu_{ac}\epsilon_{xx} \qquad (4.3)$$

Here we have written the components in terms of the strain along the applied stress direction (ϵ_{xx}) which is the variable we measure experimentally, and the in-plane and out-of-plane Poisson ratios. ϵ_{B1g} is a symmetry breaking strain that distorts the square lattice and leads to inequivalent *a* and *b* lattice constants, while $\epsilon_{A1g,1}$ and $\epsilon_{A1g,2}$ are both symmetry preserving strains, the former of which induces isotropic in-plane compression or expansion, and the latter induces strain purely along the [001] (*c* lattice) direction. The superconducting T_c is a scalar quantity and thus must belong to the trivial A_{1g} irrep, which then dictates by symmetry the following dependence of T_c on strain to lowest order:

$$T_c(\epsilon) = T_c^0\left(1 + b_1\epsilon_{A1g,1} + b_2\epsilon_{A1g,2} + a\epsilon_{B1g}^2\right) = T_c^0(1 + \beta_{A1g}\epsilon_{xx} + \alpha_{B1g}\epsilon_{xx}^2) \quad (4.4)$$

Here T_c^0 is the freestanding transition temperature and β_{A1g} and α_{B1g} parametrize the dimensionless linear and quadratic response to the measured strain ϵ_{xx}:

$$\beta_{A1g} = \frac{1}{2}b_1(1 - \nu_{ab}) - b_2\nu_{ac} \qquad \alpha_{B1g} = \frac{1}{4}a(1 + \nu_{ab})^2 \quad (4.5)$$

This work is concerned with the behavior of β_{A1g}, which contains the combined effects of both $\epsilon_{A1g,1}$ and $\epsilon_{A1g,2}$. In principle, a doping dependence of elastic constants and thus of ν_{ij} would cause the ratio of these components to vary as a function of composition. However, we have calculated ν_{ij} just above the superconducting dome from published elastic constant data[114] and found that the relevant ν_{ij} are relatively constant (Chapter 2), ensuring that β_{A1g} is measuring the response to an equivalent tuning parameter for all of the compositions relevant in this work (see Chapter 2 for details on uniaxial stress device).

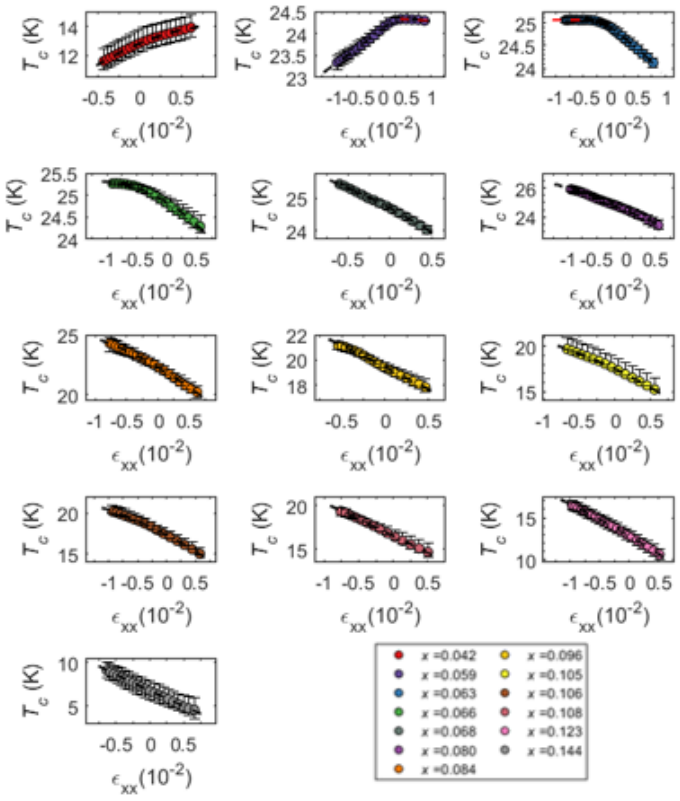

Figure 4.3. T_c versus ϵ_{xx} for a dense grid of compositions across the superconducting dome of $Ba(Fe_{1-x}Co_x)_2As_2$. T_c is defined by the 50% normal state resistivity criterion, and the upper and lower error bars are defined by the 75% and 25% criterion respectively. Black dotted lines are second order polynomial fits. Red dotted lines in the panels for x = 0.059 and 0.063 mark the region of nonlinearity discussed in the text that is excluded from the fits.

We begin by presenting resistivity measurements through the superconducting transition as a function of temperature and uniaxial stress along [100] for five representative dopings. This data is shown in Figure 4.2 where the color of each curve corresponds to the measured value of ϵ_{xx} indicated by the color bar. We can see that the applied strain has a systematic effect on the superconducting transition. Notably, the transition remains sharp with minimal increased broadening as a function of increasing strain which is in sharp contrast to the effect of stress along [110] (Chapter 3) which was shown to drastically alter the character of the transition. We also observe a clear doping dependence; the effect of strain on T_c changes sign between the compositions x = 0.059 and x = 0.063 (Figure 4.2A, B) and the relative change of T_c is larger in the overdoped compositions (Figure 4.2C) compared to the dopings near the top of the dome (Figure 4.2E).

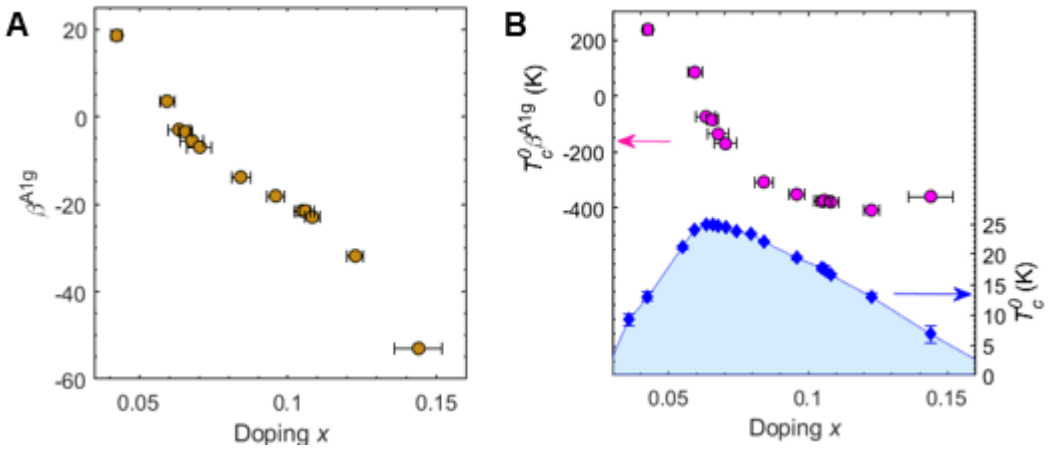

Figure 4.4. Evolution of the strain sensitivity of T_c to ϵ_{xx} A) Dimensionless linear response of T_c to the symmetry preserving A_{1g} strain (β_{A1g}) as a function of composition x. Horizontal error bars are given by the composition uncertainty as described in Chapter 2, and vertical error bars given by the 95% confidence interval of the polynomial fits in Figure 4.3 are smaller than the marker size. B) Dimensionful linear response of T_c to the symmetry preserving A_{1g} strain ($T_c^0\beta_{A1g}$) as a function of composition x (upper, left axis). Error bars are the same as in (A). Zero-strain superconducting dome as a function of composition x (lower, right axis).

We then can repeat these measurements for a dense grid of compositions and track this evolution more quantitatively and systematically as a function of doping by extracting T_c which we define as the temperature where ρ reaches 50% of its normal state value. In Figure 4.3 I show the extracted T_c as a function of ϵ_{xx} for a broad range of compositions across the superconducting dome. Here the error bars are defined by the 25% and 75% normal state resistivity criterion. Except for the three dopings closest to the top of the dome (x = 0.059, 0.063, 0.066) which show extreme nonlinear behavior over a limited range of strain (marked in red in Figure 4.3), the T_c vs ϵ_{xx} data are primarily linear with slight curvature, indicating that the response is dominated by ϵ_{A1g}. We will return to the interpretation of the nonlinear behavior near the edge of the dome, but here we point out the sharpness of this nonlinearity; for example, the x = 0.063 sample has $\frac{dT_c}{d\epsilon_{xx}} \sim -0.74\,K/\%$ for positive strain which develops into an extremely flat T_c vs ϵ_{xx} dependence with T_c = 25.07 K over an extended range of compressive strain (-0.008 < ϵ_{xx} < -0.004) with $\left|\frac{dT_c}{d\epsilon_{xx}}\right| < 0.0025\,K/\%$.

By fitting a second order polynomial to each of these data, I extract the coefficient β_{A1g} as a function of doping which is plotted in Figure 4.4A. β_{A1g} evolves smoothly and monotonically as a function of composition and we see a quantitative confirmation of the trends described above, with β_{A1g} taking on positive values for underdoped samples, crossing zero near x = 0.06,

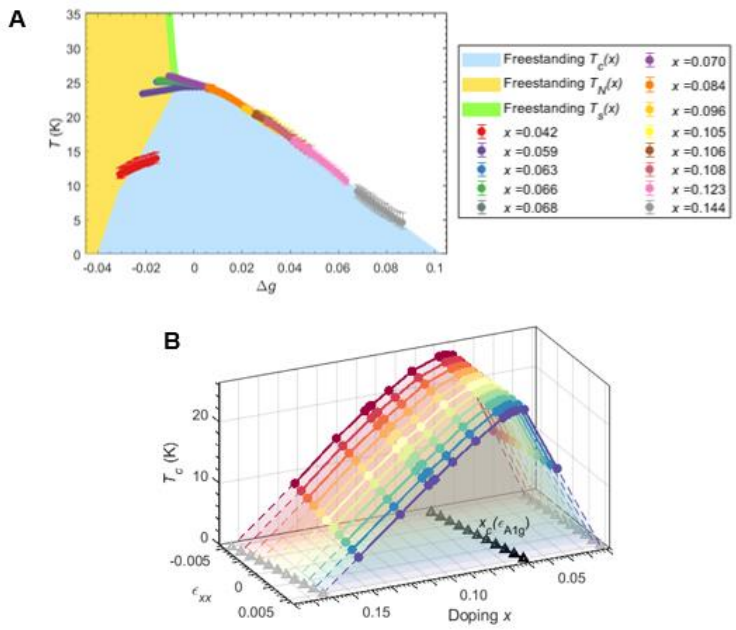

Figure 4.5. x-ϵ_{A1g} scaling and quantum critical origin of superconductivity in $Ba(Fe_{1-x}Co_x)_2As_2$ (A) T_c plotted as a function of the parameter determining proximity to the quantum critical point, $\Delta g = x - x_c^0 - a\epsilon_{A1g}$, with $x_c^0 = 0.067$ and $a = 1.45$. These data are superimposed on the zero-strain phase diagram showing the phase boundaries of nematicity (green), antiferromagnetism (yellow), and superconductivity (blue). (B) Superconducting dome as a function of x and T for different amounts of applied strain ϵ_{xx}. Dotted lines are an extrapolation of the dome to zero temperatures, with the gray arrows marking the movement of the dome boundaries as a function of applied strain. Black arrows mark the quantity $x_c(\epsilon_{A1g}) = x_c^0 - a\epsilon_{A1g}$.

and becoming negative for overdoped samples with an increasing magnitude as a function of increasing x. β_{A1g} is the dimensionless linear response of T_c to ϵ_{A1g}; we can also consider the dimensionful version $\frac{dT_c}{d\epsilon_{A1g}} = \beta_{A1g}T_c^0$ which is shown in Figure 4.4B (upper, left axis) along with the zero-strain superconducting dome $T_c^0(x)$ (right, lower axis). $\beta_{A1g}T_c^0$ varies rapidly and changes sign across the top the dome, and then becomes relatively constant over a region of x where T_c^0 vs x is linear. This behavior suggests that $\frac{dT_c}{d\epsilon_{A1g}}$ is somehow tracking the shape of the superconducting dome as a function of composition.

5.3. Quantum Critical Scaling

How can we understand this behavior and how does it connect back to quantum critical behavior? As x and ϵ_{A1g} are both non-symmetry breaking parameters, we can write the strain derivative of T_c as follows:

$$\beta_{A1g}T_c^0 = \frac{dT_c}{d\epsilon_{A1g}} = \frac{\partial T_c}{\partial \epsilon_{A1g}} + \frac{\partial T_c^0}{\partial x}\frac{\partial x}{\partial \epsilon_{A1g}} \quad (4.6)$$

Here the first term $\frac{\partial T_c}{\partial \epsilon_{A1g}}$ is an intrinsic strain effect, while the second term represents an equivalent tuning between *x* and ϵ_{A1g}. If quantum critical scaling is at play, then we would expect that composition *x* and ϵ_{A1g} act equivalently, both serving to tune the proximity to the quantum critical point. In this situation we would expect that the intrinsic term is negligible, and that the partial derivative $\frac{\partial x}{\partial \epsilon_{A1g}}$, which in general is a function of *x* and ϵ_{A1g}, is just equal to a constant ($\frac{dx}{d\epsilon_{A1g}} = a$):

$$\beta_{A1g} T_c^0 = \frac{dT_c}{d\epsilon_{A1g}} = a \frac{\partial T_c^0}{\partial x} \quad (4.7)$$

These simplifications are consistent with the evolution of the quantity $\beta_{A1g} T_c^0$ described above, as in this case it is simply proportional to $\frac{dT_c^0}{dx}$, the slope of the zero-strain $T_c^0(x)$ curve and $\frac{dx}{d\epsilon_{A1g}}$ measures the relative strength of *x* and ϵ_{A1g} as tuning parameters. If Equation 4.7 is valid, then T_c can be written as a single function of a single parameter Δg that determines to the quantum critical point:

$$T_c\left(x, \epsilon_{A1g}\right) = f(\Delta g) \quad (4.8)$$

$$\Delta g = x - x_c(\epsilon_{A1g}) = x - x_c^0 - a\epsilon_{A1g} \quad (4.9)$$

Equation 4.8 implies then all of the data in Figure 4.3 should collapse onto a single curve when plotted as a function of Δg. Furthermore, that curve should trace out the zero-strain superconducting dome $T_c^0(x, 0)$. In Figure 4.5A we show that such a scaling is observed for a broad range of compositions from the top of the dome near optimal doping deep into the heavily overdoped region, with a value of a = 1.45 and x_c^0 = 0.067.

Strikingly, the entire $T_c^0(x)$ dome in the optimally and overdoped regions is reproduced through strain tuning. Put another way, to achieve a different value of T_c, we can either measure a different composition, or we can apply ϵ_{A1g} to a given composition, and these two processes show a remarkable quantitative equivalence over a large region of the phase diagram. The scaling relation is observed to break down for the underdoped samples (*x* = 0.042 and 0.059), which is expected because these compositions are orthorhombic and thus uniaxial stress along

[100] no longer induces strains of the same symmetry as tetragonal samples. We also observe the scaling start to break down at the edge of the dome near $\Delta g \sim 0$, which is where the extreme nonlinear behavior in T_c versus ϵ_{xx} was observed and is likely due to inducing nematic order through ϵ_{A1g} tuning.

The ϵ_{A1g} considered here is a very specific combination of $\epsilon_{A1g,1}$ and $\epsilon_{A1g,2}$ (Equation 4.5); for $\pm 1\%$ of applied ϵ_{xx}, we have $\pm 0.41\%$ $\epsilon_{A1g,1}$ and $\mp 0.30\%$ $\epsilon_{A1g,2}$. The fact that T_c depends purely on Δg over such a broad range of doping and an arbitrary cut through $\epsilon_{A1g,1}/\epsilon_{A1g,2}$ parameter space is strong evidence that T_c is controlled only by proximity to the critical doping $x_c(\epsilon_{A1g})$. The most likely candidate for this critical doping is the NQCP beneath the dome, in which case the $\epsilon_{A1g} - x$ equivalence naturally follows as a consequence of critical scaling on approach to the QCP. We can visualize our data in an alternative way by plotting $T_c(x)$ for different amounts of fixed ϵ_{xx} (Figure 4.5B) which demonstrates that the superconducting dome closely tracks the location of $x_c(\epsilon_{A1g})$,providing evidence for the scenario in which the superconducting dome is born from the quantum fluctuations of the QCP.

5.4 Discussion and Summary

We now put these results in context with the previous literature. The value of a is 1.45, implying that 1.45% compressive (tensile) strain is equivalent to a 1% decrease (increase) of composition x. The sign of a is consistent with previous reports that compressive strain increases both T_s and T_N and thus shifts the quantum critical point to higher compositions.

It has been observed previously that there are strong correlations between superconductivity and structural parameters in the Fe-based superconductors[119–125]. The most robust correlations across different families of compounds are observed for the anion height above the Fe layer (d_{anion}) and the As-Fe-As bond angle (γ) where superconductivity appears to be optimized for d_{anion} = 1.38 Å and the regular tetrahedron structure with γ = 109.47°. For the hole-doped compound $Ba_{1-x}K_xFe_2As_2$ where the phase diagram is tuned by replacement of the spacer ion, structural parameters evolve similarly for doping and pressure which both generate a similar superconducting dome. For $Ba(Fe_{1-x}Co_x)_2As_2$, both thermal expansion measurements and doping and pressure dependence of T_c have suggested an equivalence between hydrostatic (1.3 GPa per % Co) or uniaxial pressure (-1.4 GPa // a and 0.66 GPa // c per % Co) with respect to

superconductivity. However, in contrast to $Ba_{1-x}K_xFe_2As_2$, the evolution of the structure is remarkably different for pressure and doping[126]. The results we show here help understand this, as they show that what matters is just the location of the parameter tuned quantum critical point, and not specific structural details.

Together with previous results for σ // [110] and independent of possible connections to quantum criticality, these measurements demonstrate that the superconductivity in $Ba(Fe_{1-x}Co_x)_2As_2$ across the entire dome is remarkably tunable by strains in different symmetry channels. Depending on the composition of the sample, experimentally accessible strains of either A_{1g} or B_{2g} symmetry allow one to achieve a wide range of T_c in a single sample. We would like to emphasize the large ϵ_{A1g} sensitivity that is observed in the heavily overdoped samples. For example, the $x = 0.144$ composition has $\beta_{A1g} \sim -50$ implying the T_c can be increased or decreased by 50% with strains on the order of 1%. This raises the prospect of tuning a superconductor to metal (SMT) phase transition as a function of ϵ_{A1g} in an even more overdoped sample near where superconductivity disappears as a function composition. It would be interesting to compare such a transition to the SMT transition tuned by anisotropic strain that is found in underdoped samples (Chapter 3).

A natural question is to determine to what extent this behavior applies more generally to other Fe-based superconductors. For example, the isovalent substituted pnictide $BaFe(As_{1-x}P_x)_2$ is a much cleaner system with more robust signatures of quantum critical behavior in the normal state. It would be illuminating to track the evolution of those behaviors as a function of strain and compare that evolution to the movement of the superconducting dome. Another natural choice are the Fe-chalcogenides, such as $FeSe_{1-x}S_x$ where a nematic quantum critical point exists without being accompanied by long-range magnetic order and its associated quantum critical point[58]. Although this study was in the single material $Ba(Fe_{1-x}Co_x)_2As_2$, this concept and methodology of shifting a quantum critical point using applied strain or some other tuning parameter and observing how superconductivity evolves can be applied very generally and may shed light on other unconventional superconductors, such as the cuprates or heavy fermion materials.

To summarize this chapter, I have presented electrical transport measurements as a function of uniaxial stress along $[100]_{tet}$ in $Ba(Fe_{1-x}Co_x)_2As_2$ which demonstrate that the

symmetry preserving structural distortion ϵ_{A1g} exhibits a scaling relation with composition x with respect to the superconducting T_c, and this scaling relationship holds over a wide region of the superconducting dome. I argued that this behavior provides evidence for the scenario where the formation of superconductivity is driven by the presence of a quantum critical point and the associated quantum critical fluctuations.

5. Elasto-Hall Effect

5.1 Introduction and Motivation

In contrast to the previous two chapters which focused on understanding the effects of strain on superconductivity and its relation to the proximate symmetry breaking phases, in this chapter I will demonstrate one implication of the fact that strain tunes the fluctuating magnetism in the normal state. In particular, I will present measurements of the resistivity and Hall coefficient as a function of uniaxial stress in $Ba(Fe_{1-x}Co_x)_2As_2$ which reveal a new transport coefficient, namely the response of the in-plane Hall coefficient R_H to anisotropic strain ϵ_{B2g} (the "Elasto-Hall" effect). I will show that this effect is large and strongly temperature dependent on approach to the magnetic phase boundary, and I will argue that this is a transport signature of strain induced enhancement of interband scattering off of spin fluctuations associated with the ordered magnetic phase.

Very generally, measurements of the electrical transport coefficients of a material are an essential basic characterization and allow one to learn a great deal about the physics happening within the material. In particular, anomalous behavior of these coefficients often signals a coupling between the conduction quasiparticles and some underlying form of collective order or fluctuations. One example is the anomalous hall effect[127] in ferromagnets, where in the ordered phase a spontaneous Hall voltage develops proportional to the magnetization. Another example is the strange metal phenomenology observed in many strongly correlated materials, where the scattering rate seems to saturate a "Planckian bound" and possibly reflects scattering from an accumulation of low energy bosonic fluctuations associated with a quantum critical point.

In the Fe-based superconductors, a particularly interesting set of transport coefficients are those of the elastoresistivity tensor which describe the strain induced changes of the resistivity tensor. The observed divergence[47] of the coefficient $2m_{66}$ proves that the nematic transition is an electronically driven phase transition, and elastoresistivity measurements have been employed to study almost every family of Fe-based superconductor, probing nematic quantum criticality[51,128], orbital selective physics[129], and XY nematic behavior[130].

Although the elastoresistivity coefficients corresponding to the diagonal components of the resistivity tensor (ρ_{xx}, ρ_{yy}) have been extensively studied, the response of the Hall resistivity

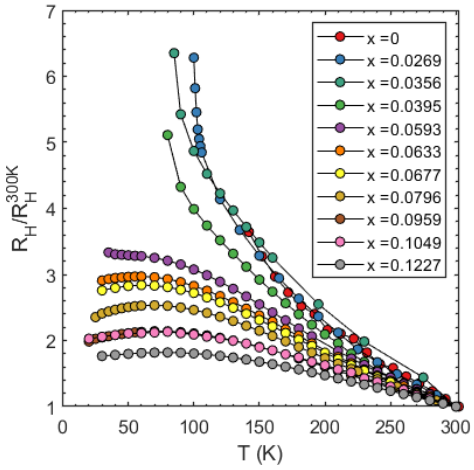

Figure 5.1 Zero-strain temperature dependence of the Hall coefficient $R_{H,}$ normalized by the room temperature value, in $Ba(Fe_{1-x}Co_x)_2As_2$. For compositions with magnetic and nematic phase transitions, only the data above the phase transitions are shown.

to applied strain has remained uninvestigated. Furthermore, there is motivation to better understand the Hall response in Fe-based superconductors, because even for zero applied strain, it shows anomalous behavior in that it is strongly temperature dependent and becomes large in magnitude at low temperature (Figure 5.1 and previous measurements[131,132]), behavior that is difficult to reconcile within standard interpretations of the Hall coefficient, even taking into account the multi-band nature of the Fermi surfaces of Fe-based superconductors. Such anomalous temperature dependence of the Hall effect has also been observed in other unconventional superconductors such as the heavy fermions[133], cuprates[134], and other Fe-based superconductors[95,96] In this chapter, we will study the elasto-Hall response and use it to shed light on the underlying mechanisms at play here.

5.2. Elasto-Hall Phenomenology

We first begin with results on an underdoped composition (x = 0.027) which in some sense is a model nematic system in that it demonstrates Curie-Weiss divergence of nematic susceptibility and has well separated nematic/structural and antiferromagnetic transitions at T_S = 103K and T_N = 97K respectively. These can be seen in the temperature dependence of the resistivity as well as the Hall coefficient in Figure 5.2b. Figure 5.2c shows the Hall resistivity as a function of magnetic field under different strain states at a temperature of T = 115K above the

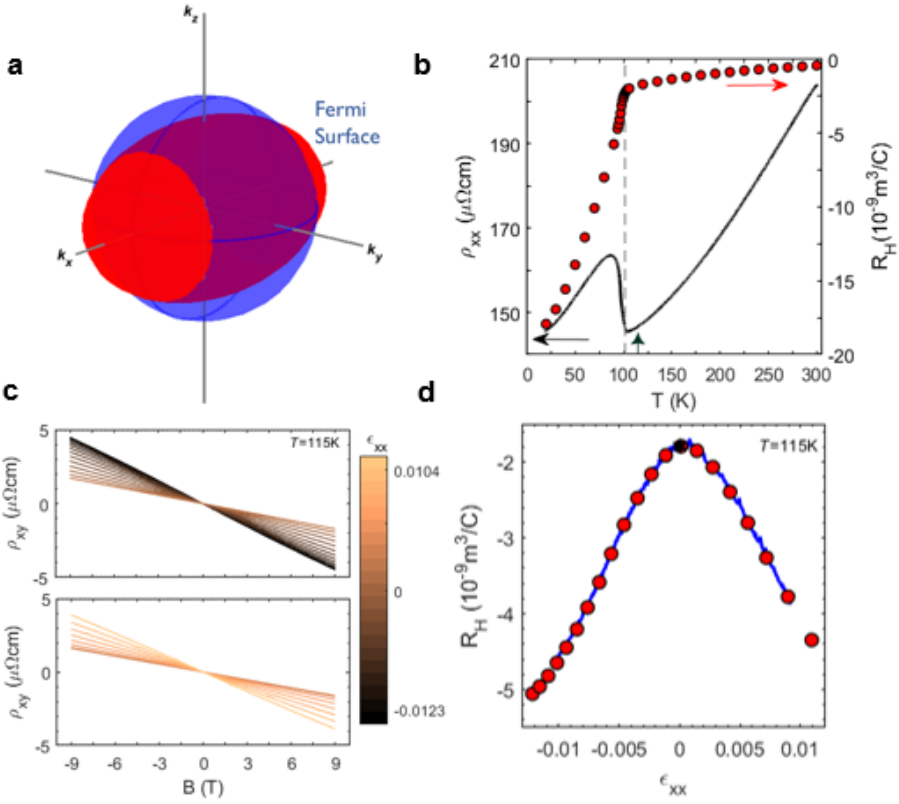

Figure 5.2. Introduction to elasto-Hall effect in the x = 0.027 composition. a) Schematic effect of volume preserving symmetry breaking B_{2g} strain on a simple metal with a spherical Fermi surface. Blue is the freestanding Fermi surface while red is the Fermi surface after strain has been applied. b) Freestanding resistivity (black, left axis) and Hall coefficient (red, right axis) as a function of temperature. The gray dashed line marks the nematic transition temperature, and the black arrow indicates the temperature where the data in panels (c) and (d) were taken. c) Hall resistivity as a function of magnetic field for different amounts of applied strain. (d) Hall coefficient as a function of applied strain. Red circles are extracted from the slope of the data in (c). Blue line is data using the fixed field method described in the text. Black star is the freestanding value of the Hall coefficient at T = 115K.

zero-strain nematic and magnetic transitions. It can be seen that the response is linear in field, which allows unambiguous determination of the Hall coefficient via $\rho_{xy} = R_H B$, and that the applied strain modulates the size of the Hall resistivity. Figure 5.2d shows the extracted R_H as a function of applied strain; R_H vs ε_{xx} demonstrates a striking nonlinear behavior with both compressive and tensile strain increasing the magnitude of R_H. This effect is not small; just 1% of applied compressive or tensile strain increases the magnitude of R_H by more than a factor of 100%.

We can understand this response more clearly through some symmetry considerations. In the tetragonal phase, uniaxial stress along [110] induces strain in both the B_{2g} and A_{1g} symmetry channels. As R_H is an isotropic quantity in-plane, it depends linearly on A_{1g} strains but can only

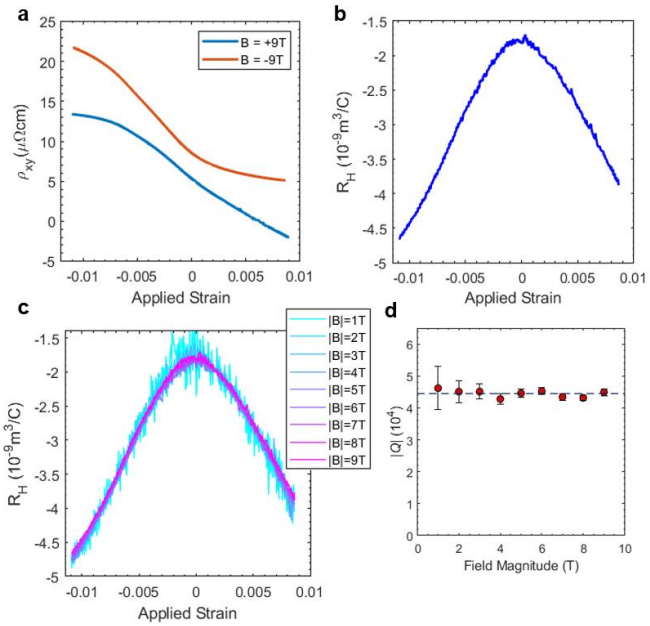

Figure 5.3. Fixed field measurement of R_H at T = 115K for x = 0.027. (a) Hall resistivity ρ_{xy} as a function of applied strain for positive and negative field (b) R_H as a function of applied strain calculated by anti-symmetrizing the data in (a) (c) R_H as a function of applied strain for different values of applied magnetic field (d) Quadratic coefficient Q^{RH} as a function of magnetic field magnitude. Error bars are given by the 95% confidence interval of the polynomial fit to the data in (c). Blue dashed line shows that Q^{RH} is independent of the applied field value.

depend quadratically on B_{2g} strains to lowest order. In principle, R_H can also depend quadratically on A_{1g} strains, but we will show in section 5.4 that this response is negligible:

$$\Delta R_H \Big/ R_H^0 = m_{A1g}^{R_H}\epsilon_{A1g} + m_{B2g,B2g}^{R_H}\epsilon_{B2g}^2 + m_{A1g,A1g}^{R_H}\epsilon_{A1g}^2 \quad (5.1)$$

$$= \frac{1}{2}m_{A1g}^{R_H}\alpha(1-\nu_{110})\epsilon_{xx} + \frac{1}{4}m_{B2g,B2g}^{R_H}\alpha^2(1+\nu_{110})^2\epsilon_{xx}^2 + \frac{1}{4}m_{B2g,B2g}^{R_H}\alpha^2(1+\nu_{110})^2\epsilon_{xx}^2$$

Thus, the quadratic response we observe can be attributed to the B_{2g} quadratic coefficient which takes the form:

$$Q^{R_H} = \frac{1}{4}m_{B2g,B2g}^{R_H}\alpha^2(1+\nu_{110})^2 \quad (5.2)$$

It is instructive to consider what one might expect for the strain-induced changes of R_H for a simple metal with a spherical Fermi surface (Figure 5.2a). Because ϵ_{B2g} is a volume-preserving distortion, we expect it to change the shape of the Fermi surface, but to preserve its volume, and since R_H is simply related to the carrier density which is in turn proportional to the Fermi surface volume, we expect ϵ_{B2g} to have little effect on R_H in sharp contrast to the behavior we observe here. The Fe-based superconductors are not simple metals with spherical Fermi

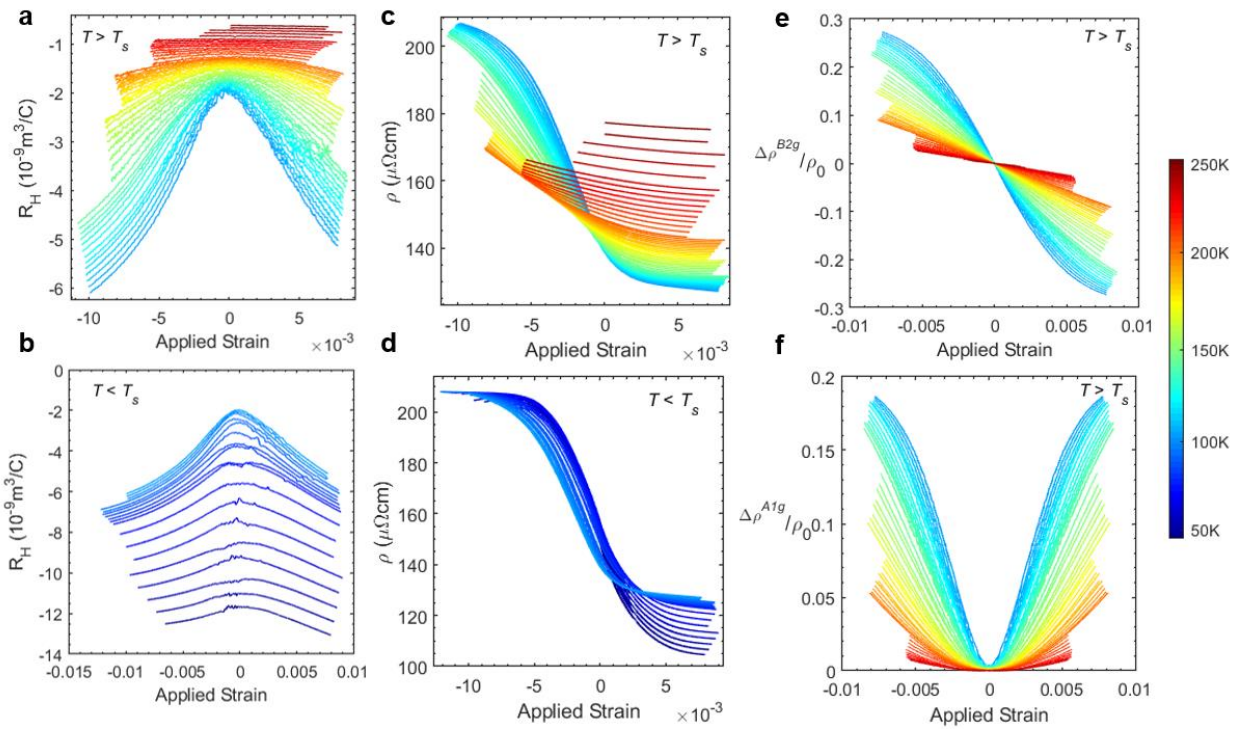

Figure 5.4 Temperature dependence of elastoresistivity and elasto-Hall in the x = 0.027 composition. Hall coefficient above (a) and below (b) the nematic transition as a function of applied strain. Resistivity above (c) and below (d) the nematic transition as a function of applied strain. Antisymmetric (e) and symmetric (f) components of the resistivity as a function of strain above the nematic transition. In all panels the temperature is given by the color bar.

surfaces and have a quasi-2D multi-sheet Fermi surface, but the strain evolution that we observe is difficult to understand within standard paradigms of calculating the Hall coefficient, such as the multi-band relaxation time approximation of Boltzmann transport. This is similar to the zero-strain temperature dependence, and I will argue below that these two anomalous effects have a common origin.

An alternative way to collect these data is to fix magnetic field and temperature and sweep the strain applied to the sample and measure ρ_{xy} for both positive and negative field and anti-symmetrize (Figure 5.3). This results in the blue trace in Figure 5.2d which agrees well with the fixed strain data and the free-standing (zero strain) value of R_H (black star). The linearity of R_H implies that this procedure produces the same R_H regardless of the field chosen (see Figure 5.3). This measurement protocol is much more efficient which will allow us to easily study the temperature dependence of this behavior.

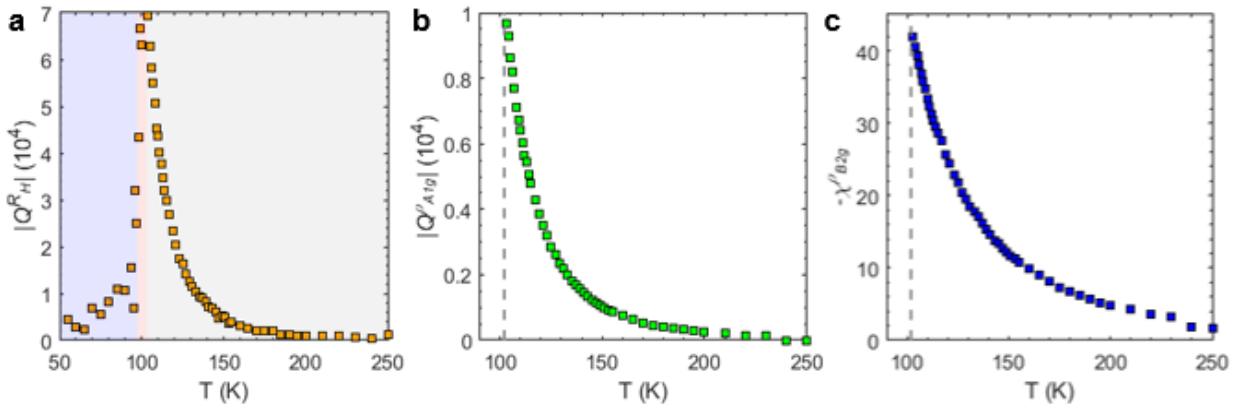

Figure 5.5. Elasto-Hall and elastoresistivity coefficients temperature dependence for the x = 0.027 composition. (a) Q^{RH} versus temperature. The gray, red, and green regions indicate the normal state, nematic phase, and antiferromagnetic phase respectively. (b) $Q^{\rho A1g}$ and (c) $\chi^{\rho B2g}$ versus temperature. Gray dotted line marks the nematic transition temperature.

5.3 Divergence of Elasto-Hall in Underdoped Compositions

Figure 5.4a-b shows R_H as a function of applied strain using the fixed field method ($|B|$ = 9T) for different fixed temperatures given by the color bar, for temperatures above (a) and below (b) the nematic transition temperature. The elasto-Hall response is strongly temperature dependent, with the nonlinearity growing as the temperature is lowered towards the nematic/magnetic transition temperatures. Below those transitions, the response begins to diminish and develops a flatter region for low values of strain.

The six-point contact configuration allows us to measure two other elastoresistivity coefficients, which can be extracted from the ρ_{xx} versus ϵ_{xx} curves according to the following symmetry considerations. The isotropic and anisotropic components of the in-plane resistivity by symmetry have the following dependence on the irreducible strain components:

$$\frac{\Delta\rho^{A1g}}{\rho_0} = \frac{\Delta\rho_{xx}+\Delta\rho_{yy}}{\rho_0} = m_{A1g}^{A1g}\epsilon_{A1g} + m_{B2g,B2g}^{A1g}\epsilon_{B2g}^2 + m_{A1g,A1g}^{A1g}\epsilon_{A1g}^2 \quad (5.3)$$

$$\frac{\Delta\rho^{B2g}}{\rho_0} = \frac{\Delta\rho_{xx}-\Delta\rho_{yy}}{\rho_0} = m_{B2g}^{B2g}\epsilon_{B2g} \quad (5.4)$$

Previous elasto-resistivity experiments[135] have demonstrated that the first and third terms in the first equation are negligible. In this case, adding these two equations gives:

$$\frac{\Delta\rho_{xx}}{\rho_0} = m_{B2g}^{B2g}\epsilon_{B2g} + m_{B2g,B2g}^{A1g}\epsilon_{B2g}^2 \quad (5.5)$$

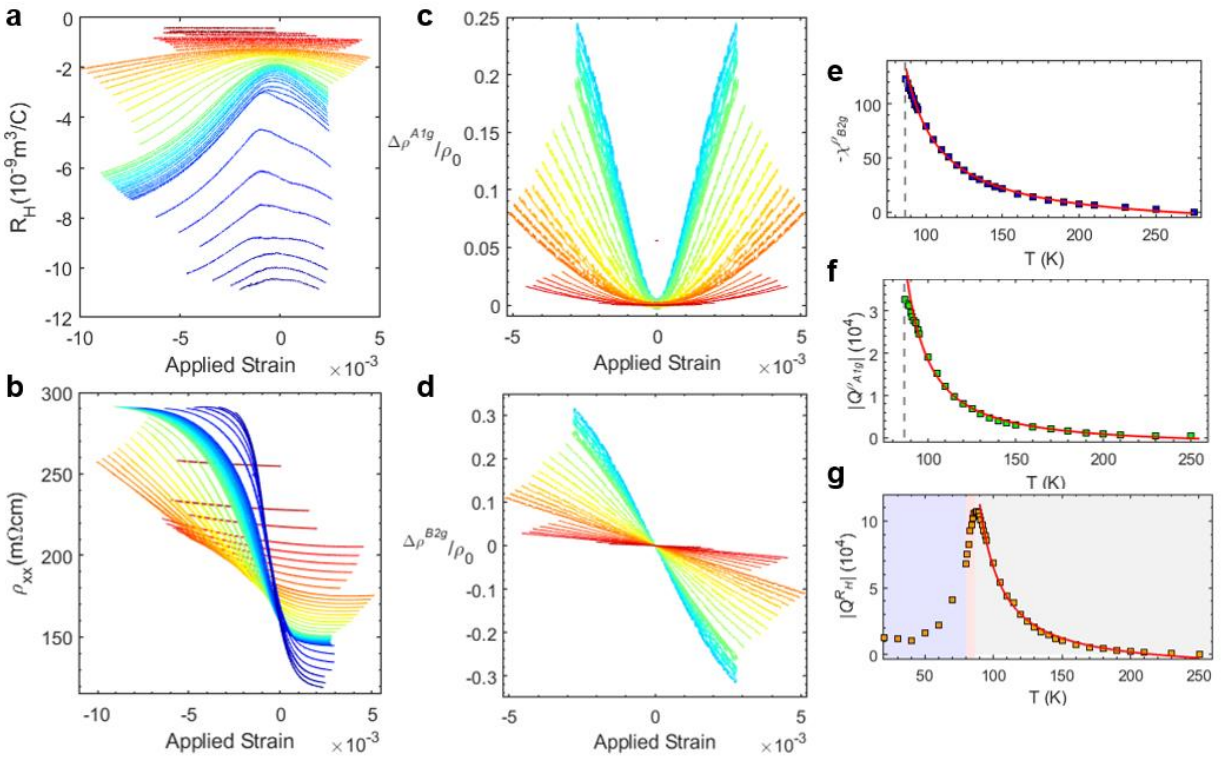

Figure 5.6. Elasto-Hall effect and elastoresistivity in the x = 0.036 composition. Hall coefficient (a) and resistivity (b) as a function of applied strain. Symmetric (c) and antisymmetric (d) components of the resistivity as a function of strain above the nematic transition. In all panels the temperature is given by the color bar. (e) $\chi^{\rho B2g}$, (f) $Q^{\rho A1g}$ and (g) Q^{RH} versus temperature. The gray dotted line in (e+f) marks the nematic transition temperature. The gray, red, and green regions in (g) indicate the normal state, nematic phase, and antiferromagnetic phase respectively. Solid red lines are guides to the eye.

$$= \frac{1}{2} m_{B2g}^{B2g} \alpha (1 + \nu_{110}) \epsilon_{xx} + \frac{1}{4} \alpha^2 (1 + \nu_{110})^2 m_{B2g,B2g}^{A1g} \epsilon_{xx}^2 \quad (5.6)$$

From this expression we then see that we can isolate these two contributions by simply measuring the resistivity in the direction of the applied strain (ρ_{xx}), and then symmetrizing and anti-symmetrizing the data about zero strain. These two contributions are parametrized by the two coefficients:

$$\chi^{\rho_{B2g}} = \frac{1}{2} m_{B2g}^{B2g} \alpha (1 + \nu_{110}) \quad (5.7)$$

$$Q^{\rho_{A1g}} = \frac{1}{4} \alpha^2 (1 + \nu_{110})^2 m_{B2g,B2g}^{A1g} \quad (5.8)$$

Figure 5.4c and d show the resistivity in the direction of applied stress as a function of applied strain at different fixed temperatures above (c) and below (d) the nematic transition. Similar to the elasto-Hall, we observe strong temperature dependence and the development of

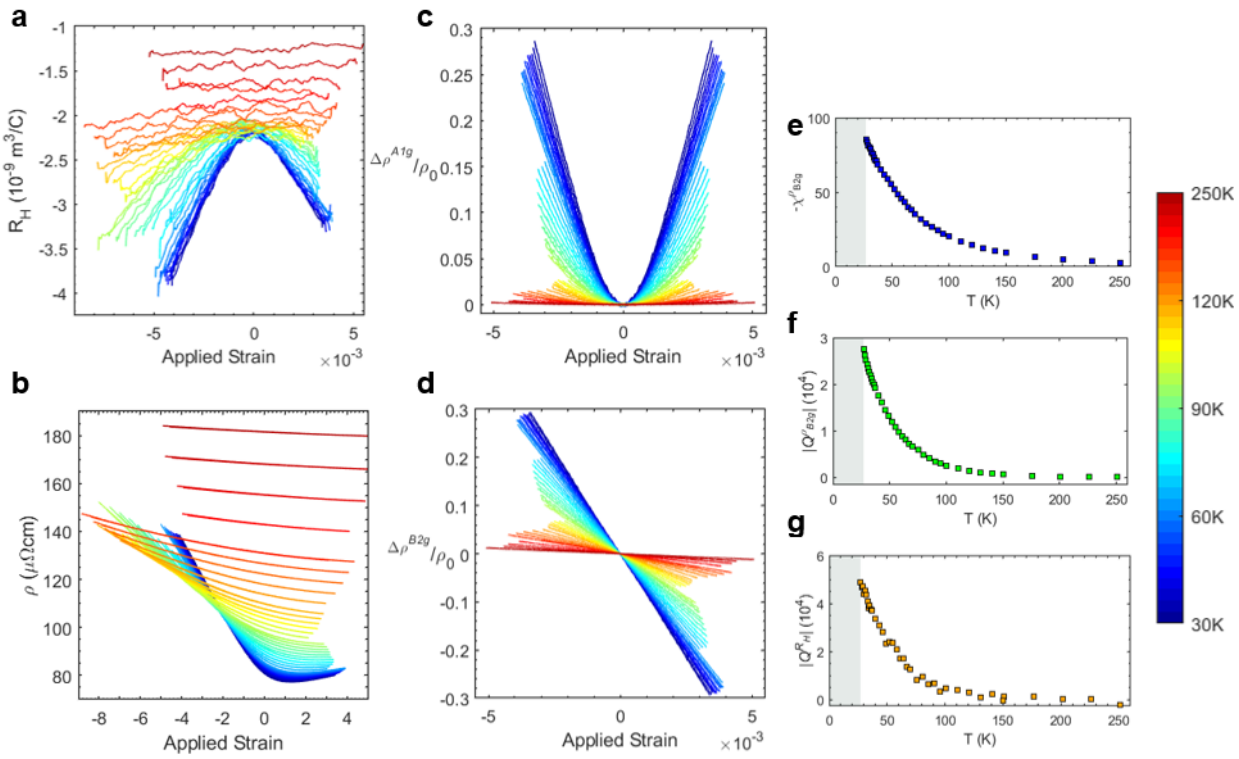

Figure 5.7. Elasto-Hall effect and elastoresistivity in the x = 0.068 composition. Hall coefficient (a) and resistivity (b) as a function of applied strain. Symmetric (c) and antisymmetric (d) components of the resistivity as a function of strain above the nematic transition. In all panels the temperature is given by the color bar. (e) $\chi^{\rho B2g}$, (f) $Q^{\rho A1g}$ and (g) Q^{RH} versus temperature. The gray region indicates the superconducting state.

non-linearity at low temperatures. Below T_s, the response becomes dominated by the intrinsic resistivity anisotropy of the nematic phase, with uniaxial stress acting to align the domains and fully develop the anisotropy. This corresponds to the flattened regions below T_s in the elasto-Hall response. Above the nematic transition, using the symmetry decomposition justified above, we can isolate the two components ρ^{A1g} and ρ^{B2g} which are plotted in Figure 5.4e and f respectively. The increasing magnitude of the linear response of ρ^{B2g} to ϵ_{B2g} reflects the divergent nematic susceptibility to which m_{B2g}^{B2g} and thus $\chi^{\rho_{B2g}}$ is directly proportional. The increasing magnitude of the quadratic response of ρ^{A1g} to ϵ_{B2g} has been reported previously[136] and was interpreted as a symmetry allowed term with a divergence that reflected a sensitivity of the isotropic electronic properties to the nematic fluctuations.

Using linear fits of the low strain data in Figure 5.4e and quadratic fits to the low strain data in Figures 5.4a and 5.4f, we can extract the temperature dependence of the coefficients

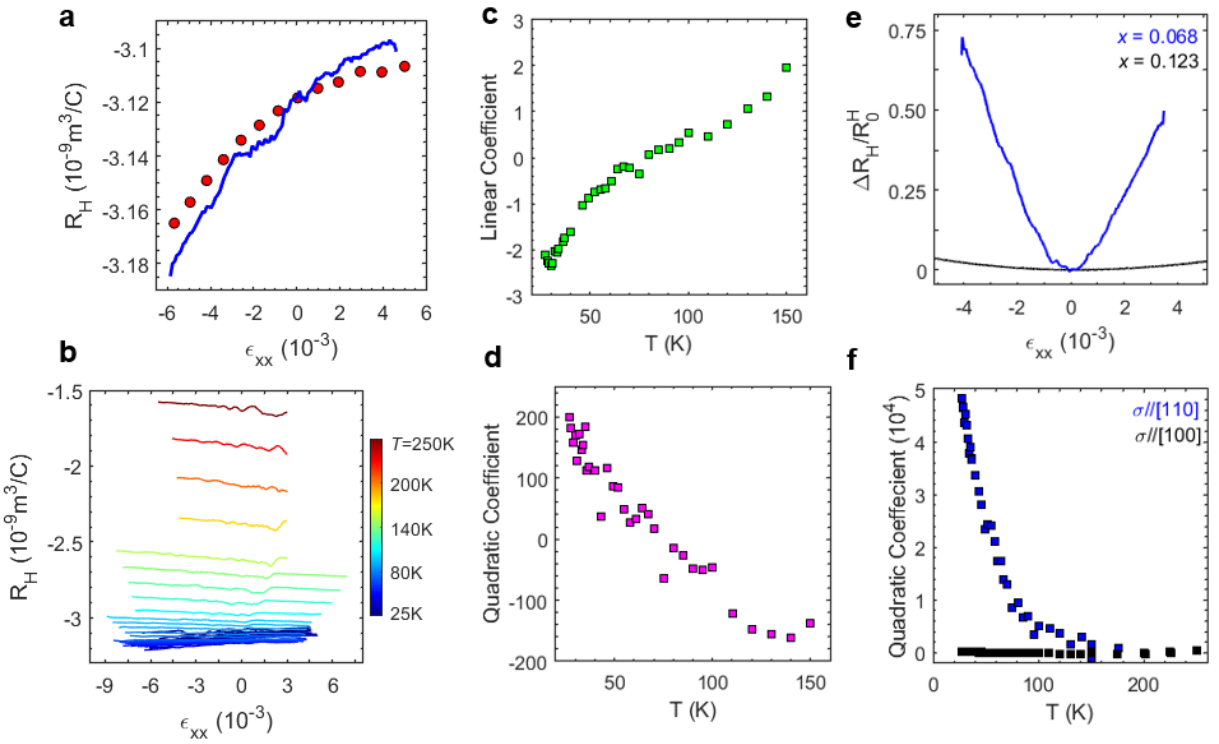

Figure 5.8. Elasto-Hall effect for uniaxial stress along [100] in the x = 0.068 composition. (a) Hall coefficient as a function of applied strain at T = 30K. Red circles are measured using fixed strain and variable field. Blue line is measured using fixed field and variable strain. (b) Temperature dependence of the elasto-Hall response (c) Linear and (d) quadratic coefficients extracted from second order polynomial fits to the data in (b). (e) Comparison of elasto-Hall response for stress along [100] and stress along [110] at T = 30K. (f) Comparison of the temperature dependence of the quadratic elasto-Hall coefficient for stress along [100] and stress along [110].

$\chi^{\rho B2g}$, $Q^{\rho A1g}$, and Q^{RH} which are shown in Figure 5.5. We see that all three of these quantities exhibit diverging behavior towards the magnetic/nematic transitions and take on values that are large in magnitude near those transitions: $\chi^{\rho B2g} \sim$ -42, $Q^{\rho A1g} \sim$ 30,000, and $Q^{RH} \sim$ -70,000. Another underdoped sample with larger amounts of cobalt (x = 0.034) exhibits very similar behavior, with the temperature dependence shifted down due to the lower phase transition critical temperatures (Figure 5.6).

5.4. Optimal and Overdoped Compositions and σ // [100]

All of the measurements presented so far have been on compositions with static nematic and magnetic order developing at some non-zero temperature. I now will investigate the elasto-Hall response in optimally and overdoped samples with x = 0.068 and x = 0.123 where no such phase transitions are present. Figure 5.7a shows the temperature dependence of the elasto-Hall

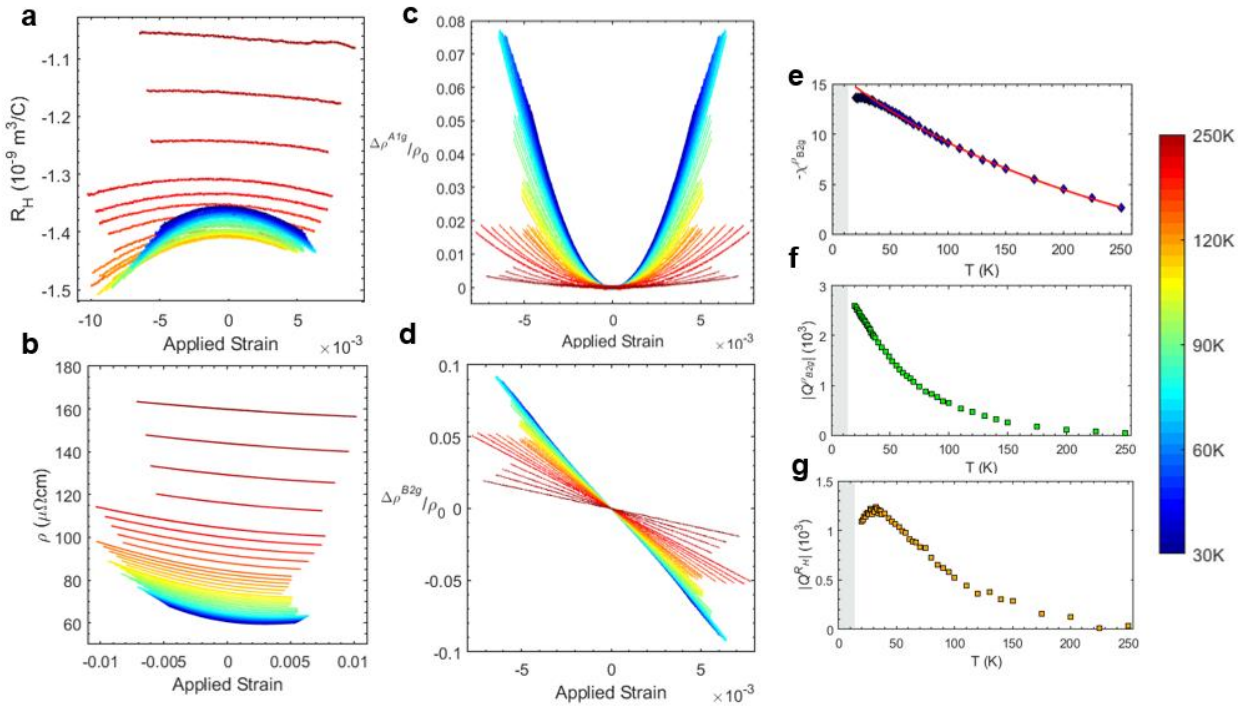

Figure 5.9. Elasto-Hall effect in an overdoped composition x = 0.123. Hall coefficient (a) and resistivity (b) as a function of applied strain. Symmetric (c) and antisymmetric (d) components of the resistivity as a function of strain above the nematic transition. In all panels the temperature is given by the color bar. (e) $\chi^{\rho B2g}$, (f) $Q^{\rho A1g}$ and (g) Q^{RH} versus temperature. The gray region indicates the superconducting state.

response for the optimally doped composition above the superconducting transition. We observe that the response is still strongly temperature dependent, with a large non-linearity present at low temperatures. As before, this is accompanied by strongly temperature dependent elastoresistivity (Figure 5.7b) that can again be decomposed into the strain symmetric and antisymmetric components corresponding to ρ^{A1g} and ρ^{B2g} (Figure 5.7c-d). Using the same fitting procedure as the previous section, I extract the coefficients $\chi^{\rho B2g}$, $Q^{\rho A1g}$, and Q^{RH} which are all found to show diverging behavior towards zero temperature, although this divergence is cut off by the superconducting transition. Again, all three of these quantities are large at low temperature ($\chi^{\rho B2g}$ ~ -90, $Q^{\rho A1g}$ ~ 10,000, and Q^{RH} ~ -70,000).

We can also measure the elasto-Hall response for uniaxial stress along [100], which induces A_{1g} and B_{1g} strains. This data for the optimally doped composition is shown in Figure 5.8. We observe that the response is no longer dominated by quadratic behavior, but instead is primarily linear which implies the sensitivity to A_{1g} strain is the dominant effect. This effect is small (order 1) and has a weak temperature dependence (Figure 5.8c) and switches sign near T = 80K. The quadratic response (Figure 5.8d) is orders of magnitude smaller than for stress along

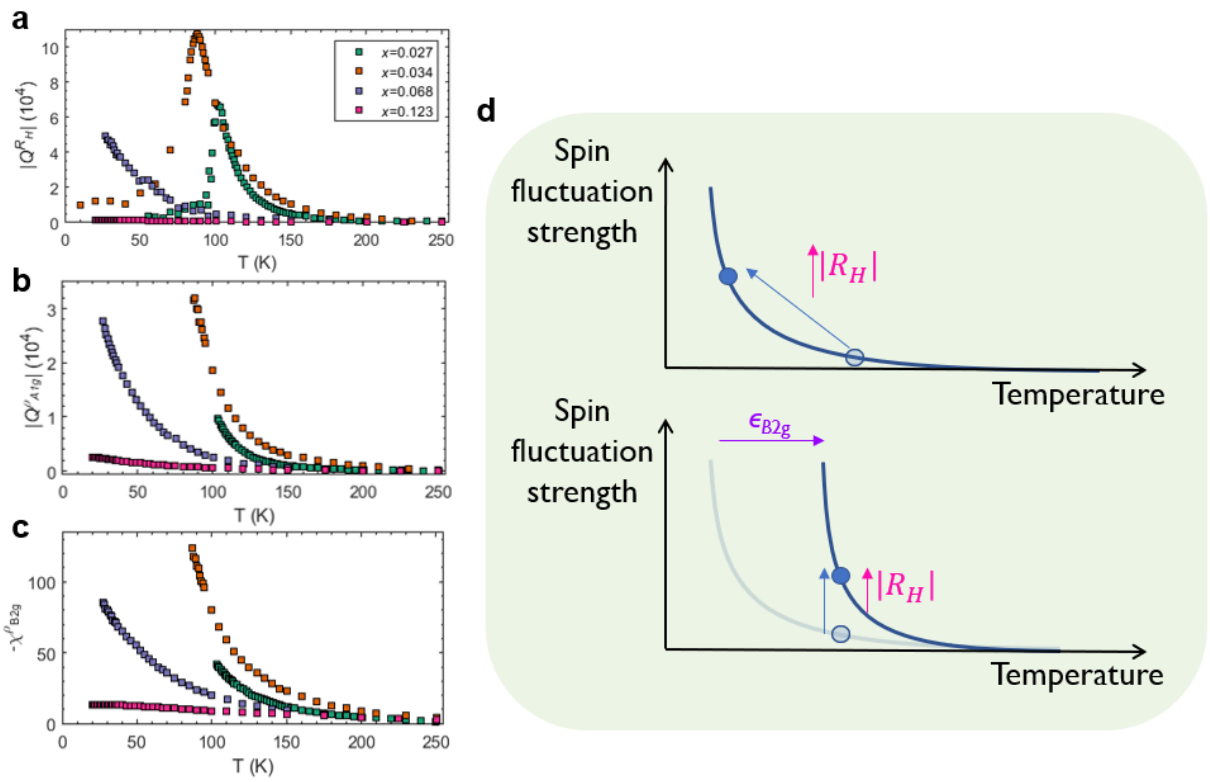

Figure 5.10. Elasto-Hall effect and spin fluctuations. Compilation of the doping and temperature dependence for the three elasto-transport coefficients (a) Q^{RH}, (b) $Q^{\rho A1g}$, and (c) $\chi^{\rho B2g}$. (d) Effect of temperature and strain on the spin fluctuation strength (blue). Spin fluctuations can be enhanced either by lowering the temperature (upper graph) or applying B_{2g} strain at a fixed temperature (upper graph).

[110] (Figure 5.8e-f), which confirms that the non-linear elasto-Hall response is indeed a response to the symmetry breaking B_{2g} strain, and not a quadratic response to the symmetry preserving A_{1g} strain. For the overdoped composition (x = 0.123) (Figure 5.9), the elasto-Hall response is still dominated by the quadratic response to ϵ_{B2g} (Figure 5.9a), and exhibits some temperature dependence, but the magnitude is more than an order of magnitude smaller than the optimally doped composition. This is similarly true for both the elastoresistivity coefficients corresponding to ρ^{A1g} and ρ^{B2g} (Figure 5.9c-g).

5.5 Strain-Induced Enhancement of Spin Fluctuations

How can we understand the phenomenology laid out in the previous five sections? The underlying mechanism must have the three following features (Figure 5.10a-c):

1. sensitive to ϵ_{B2g}
2. strongly temperature dependent
3. only present near but outside the magnetic phase boundary

I now appeal to a number of theoretical works[137–139] that predict an enhancement of the Hall coefficient in systems with multi-band Fermi surfaces and interband interactions due to spin fluctuations, such as the Fe-based superconductors. These works find that these interband interactions cause a breakdown of the relaxation time approximation (RTA) in Boltzmann transport calculations, and that this causes the Hall coefficient to be greatly enhanced in magnitude compared to the naïve expectation of the RTA. Furthermore, they predict that this effect is strongly temperature dependent due to the temperature dependence of the spin fluctuations, which they describe within a marginal Fermi liquid framework.

The basic idea of these theory proposals is that because the spin susceptibility which governs the scattering is highly peaked in momentum near the ordering wave vector, there are "hot" (high scattering) and "cold" (low scattering) regions of the Fermi surface; the hot regions are those parts of the Fermi surface that are connected by translation through the ordering wave vector. This "hot spot" concept has also been employed to the cuprates, and in that case these hot regions are short-circuited by the cold regions of the Fermi surface. The situation is different for the Fe-based superconductors because of the multi-band nature; the anisotropy of the forward scattering induced by the spin fluctuations compensates the shorter lifetimes at the hot spots, preventing them from being short-circuited and allowing them to contribute to transport.

The effect of these hot spots turns out to strongly alter the vector mean free paths and effective relaxation times of the conduction quasiparticles. In particular, it causes the vector mean free paths of both the hole and electron carriers to point in the same direction and is decided by the majority carriers, which are the electrons in the case of electron doped Fe-based superconductors like $Ba(Fe_{1-x}Co_x)_2As_2$. This mechanism which in some sense causes the holes to behave like electrons then results in an increased magnitude of the Hall coefficient.

We have already referenced the fact that strain in the B_{2g} symmetry channel enhances spin fluctuations outside of the magnetic phase, which has been measured directly by NMR measurements under uniaxial stress[140]. This fact along with the theoretical proposals described above then allows us to understand the elasto-Hall phenomenology described in this chapter as a transport signature of a strain-induced enhancement of interband scattering from spin fluctuations. This is consistent with the three points listed at the beginning of this section: the strain tuning of the fluctuations is only expected to be sensitive $\epsilon_{B2g,}$ the strong temperature

dependence we observe is because the spin fluctuations are diverging towards the antiferromagnetic ordering temperature, and the effect is still present for optimal doping where strong temperature dependent spin fluctuations are still observed by NMR but becomes much smaller for the overdoped where those fluctuations are much weaker[76].

This framework also sheds light on the zero-strain behavior of the Hall coefficient shown in Figure 5.1. This is because there are two different ways we can enhance the strength of spin fluctuations; at a fixed temperature, we can apply strain which gives the elasto-Hall effect, or at a fixed strain (such as zero) we can lower the temperature (Figure 5.10d). In both cases we observe an enhancement of the Hall coefficient consistent with our interpretation laid out above.

5.6. Summary

In this chapter, I have presented electrical transport measurements as a function of uniaxial stress and temperature which investigate a new elastoresistivity coefficient, the response of the in-plane Hall coefficient to applied strains (elasto-Hall effect). This effect is found to be large and strongly temperature dependent for uniaxial stress along [110] inducing B_{2g} strain above the nematic and antiferromagnetic transition for underdoped samples, and at all temperatures above the superconducting transition for the optimally doped sample. The response is much weaker for uniaxial stress along [100] and for an overdoped sample far away from the magnetic phase boundary. I argued that all of the data presented in this chapter point towards a strain induced enhancement of interband scattering from spin fluctuations as the origin of the elasto-Hall effect, and that this also helps explain the zero-strain anomalous temperature dependence of the Hall effect in this material.

6. Summary and Outlook

Understanding unconventional and high temperature superconductivity has proven to be an extremely difficult problem both theoretically and experimentally. One reason for this is the intertwined nature of the phase diagrams of these materials, where proximate symmetry breaking phases compete with superconductivity, but the fluctuations of those phases feed into the superconducting pairing mechanisms. An additional complication is the presence of quantum critical points and low energy quantum fluctuations coupled to the conduction quasiparticles. Finally, the superconducting pairing mechanism likely involves the electrons themselves as the degrees of freedom leading to pairing. All of these factors make for an extremely complicated system that is difficult to study both theoretically and experimentally.

Many of the commonly accepted beliefs about unconventional superconductivity have been based on relatively circumstantial evidence, such as the common phenomenology of superconducting domes centered near putative quantum critical points. In this thesis, I have shown that using applied strains of different symmetries, we are able to give direct experimental demonstrations of the relationships between superconductivity and the other symmetry breaking phases (nematicity, magnetism) in an Fe-based superconductor $Ba(Fe_{1-x}Co_x)_2As_2$. In Chapter 3 I showed that strain enhancing nematic order is extremely efficient in suppressing superconductivity, providing evidence that nematic fluctuations are a key ingredient in the superconducting pairing. In Chapter 4, I demonstrated that strain with symmetry orthogonal to nematic order exhibits a scaling relationship with composition, demonstrating that the formation of the superconducting dome is truly driven by the presence of a quantum critical point. Together, these two chapters also show that the superconductivity in $Ba(Fe_{1-x}Co_x)_2As_2$ is remarkably tunable by strain of different symmetries depending on the location in the phase diagram. In the underdoped region, B_{2g} strain tunes a superconductor to metal quantum phase transition, and for overdoped samples T_c is largely tunable by A_{1g} strain. I have also showed how strain tunes the fluctuating magnetism in the normal state outside of the superconducting state; in Chapter 5, I described a new strongly temperature dependent transport coefficient (the elasto-Hall effect) which I argued is a transport signature of strain induced enhancement of scattering from spin fluctuations.

As an outlook to future work, in Chapter 3 I showed that underdoped $Ba(Fe_{1-x}Co_x)_2As_2$ with uniaxial stress along [110] provides a platform for studying a superconductor to metal transition in a bulk three-dimensional material. This could allow for previously inaccessible probes of such a transition, such as thermodynamic measurements like heat capacity or scanning probe measurements. These measurements may also be able to shed light on smeared nature of the SC transition under large amounts of stress, which appears to be an intrinsic phenomenon, and may be related to the anomalous metal state[141] found in many two-dimensional superconducting systems. Furthermore, the large A_{1g} strain sensitivity in heavily overdoped samples found in Chapter 4 implies that another strain tuned superconductor to metal quantum phase transition should be realizable on the overdoped side of the phase diagram.

The wealth of information gained through observing the effects of strain on superconductivity in this material highly motivate similar measurements on other Fe-based superconductors. For example, given that the logic of the argument in Chapter 3 hinges on the separate and distinct ways that strain tunes both the nematic and magnetic fluctuations, it is crucial to investigate the strain dependence of T_c in other systems, such as the iron chalcogenide $FeSe_{1-x}S_x$ where there is a putative nematic quantum critical point without nearby long-range magnetism. For the quantum critical superconductivity discussed in Chapter 4, the isovalent-substituted compound $BaFe_2(As_{1-x}P_x)_2$ is a natural candidate as it is a much cleaner system with more robust signatures of quantum criticality in the normal state. This may, for example, allow one to track the evolution of the quantum critical fan simultaneously with the movement of the superconducting dome as the location of the quantum critical point is tuned by strain.

The methodology and interpretation of the elasto-Hall effect laid out in Chapter 5 have the potential to lead to wide variety of future investigation. A more detailed set of measurements as a function of temperature and composition could allow one to map out how the spin fluctuations and their coupling to the conduction electrons evolves across the phase diagram. Additionally, these measurements could be applied to other families of Fe-based superconductors; given the knowledge gained and successes from studying the nematic fluctuations via elastoresistivity measurements in many different families, a similar thorough investigation of the elasto-Hall effect is likely to be proven fruitful. These measurements may also allow us to illuminate an explicit microscopic connection between the nematic and spin

fluctuations. Lastly, the elasto-Hall effect and the underlying spin fluctuations responsible may be intimately connected to the strange metal phenomenology found in many correlated quantum materials.

Finally, it is natural to ask how all of these phenomena apply more generally, even outside of Fe-based superconductivity. The measurements in this thesis demonstrate the importance of nematic fluctuations and quantum criticality for the high temperature unconventional superconductivity in this representative Fe-based superconductor, but to what extent are those ingredients necessary more broadly? In Chapter 4, I showed that the presence of a quantum critical point drives the superconducting dome in $Ba(Fe_{1-x}Co_x)_2As_2$. This conceptual framework and methodology of moving the quantum critical point with an external tuning parameter and observing how superconductivity responds could be applied to any material system, such as the cuprates and heavy fermion superconductors.

Bibliography

1. Basov, D. N., Averitt, R. D. & Hsieh, D. Towards properties on demand in quantum materials. *Nat. Mater.* **16**, 1077–1088 (2017).

2. Keimer, B. & Moore, J. E. The physics of quantum materials. *Nat. Phys.* **13**, 1045–1055 (2017).

3. Giustino, F. *et al.* The 2021 quantum materials roadmap. *J. Phys. Mater.* **3**, (2020).

4. Anderson, P. W. More Is Different. *Science* **177**, 393–396 (1972).

5. Monthoux, P., Pines, D. & Lonzarich, G. G. Superconductivity without phonons. *Nature* **450**, 1177–1182 (2007).

6. Scalapino, D. J. A common thread: The pairing interaction for unconventional superconductors. *Rev. Mod. Phys.* **84**, 1383–1417 (2012).

7. Norman, M. R. The challenge of unconventional superconductivity. *Science* **332**, 196–200 (2011).

8. Fradkin, E., Kivelson, S. A. & Tranquada, J. M. Colloquium : Theory of intertwined orders in high temperature superconductors. *Rev. Mod. Phys.* **87**, 457–482 (2015).

9. Greene, R. L., Mandal, P. R., Poniatowski, N. R. & Sarkar, T. The Strange Metal State of the Electron-Doped Cuprates. *Annu. Rev. Condens. Matter Phys.* **11**, 213–229 (2020).

10. Hartnoll, S. A. Theory of universal incoherent metallic transport. *Nat. Phys.* **11**, 54–61 (2015).

11. Hartnoll, S. A. & Mackenzie, A. P. Planckian Dissipation in Metals. *arXiv: 2107.07802* (2021).

12. Fradkin, E. & Kivelson, S. A. Ineluctable complexity. *Nat. Phys.* **8**, 864–866 (2012).

13. Fernandes, R. M. *et al.* Iron pnictides and chalcogenides: a new paradigm for superconductivity. *Nature* **601**, 35–44 (2022).

14. Paglione, J. & Greene, R. L. High-temperature superconductivity in iron-based materials. *Nat. Phys.* **6**, 645–658 (2010).

15. Chen, X., Dai, P., Feng, D., Xiang, T. & Zhang, F. C. Iron-based high transition temperature superconductors. *National Science Review* **1**, 371–395 (2014).

16. Stewart, G. R. Superconductivity in iron compounds. *Rev. Mod. Phys.* **83**, 1589–1652 (2011).

17. Abrikosov, A. A. *Fundamentals of the Theory of Metals*. (Dover Publications, Inc., 1988).

18. Tinkham, M. *Introduction to Superconductivity*. (Dover Publications, Inc., 1996).

19. Schneider, T. & Singer, J. M. *Phase Transition Approach to High Temperature Superconductivity*. *Phase*

Transition Approach to High Temperature Superconductivity (Imperial College Press, 2000).

20. Ginzburg, V. L. & Landau, L. D. On the Theory of Superconductivity. *Sov. Phys. JETP* **20**, 1064 (1950).

21. Bardeen, J., Cooper, L. N. & Schrieffer, J. R. Theory of superconductivity. *Phys. Rev.* **108**, (1957).

22. Gor'kov, L. P. Microscopic derivation of the Ginzburg-Landau equations in the theory of superconductivity. *Sov. Phys. JETP* **36**, 1364–1367 (1959).

23. Mcmillan, W. L. Transition Temperature of Strong-Coupled Superconductors. *Phys. Rev.* **167**, (1968).

24. Choi, H. J., Roundy, D., Sun, H., Cohen, M. L. & Louie, S. G. The origin of the anomalous superconducting properties of MgB_2. *Nature* **418**, 758–760 (2002).

25. Pickard, C. J., Errea, I. & Eremets, M. I. Superconducting Hydrides Under Pressure. *Annu. Rev. Condens. Matter Phys.* **11**, 57–76 (2019).

26. Bednorz, J. G. & Muller, K. A. Possible high T_c superconductivity in the Ba-La-Cu-O system. *Zeitschrift fir Phys. B Condens. Matter* **64**, 189–193 (1986).

27. Sun, G., Wong, K., Xu, B. & Lu, D. T_c enhancement of $HgBa_2Ca_2Cu_30_8$ by T1 substitution. *Phys. Lett. A* **192**, 122–124 (1994).

28. Tsuei, C. C. *et al.* Pairing Symmetry and Flux Quantization in a Tricrystal Superconducting Ring of $YBa_2Cu_30_{7-\delta}$. *Phys. Rev. Lett.* **73**, 593–596 (1994).

29. Kamihara, Y., Watanabe, T., Hirano, M. & Hosono, H. Iron-Based Layered Superconductor $La(O_{1-x}F_x)FeAs$ ($x = 0.05-0.12$) with $T_c = 26$ K. *J. Am. Chem. Soc.* **130**, 3296–3297 (2008).

30. Fink, J. *et al.* Electronic structure studies of $BaFe_2As_2$ by angle-resolved photoemission spectroscopy. *Phys. Rev. B* **79**, 155118 (2009).

31. Analytis, J. G. *et al.* Quantum oscillations in the parent pnictide $BaFe_2As_2$: Itinerant electrons in the reconstructed state. *Phys. Rev. B* **80**, 064507 (2009).

32. Mazin, I. I., Johannes, M. D., Boeri, L., Koepernik, K. & Singh, D. J. Problems with reconciling density functional theory calculations with experiment in ferropnictides. *Phys. Rev. B* **78**, 085104 (2008).

33. De' Medici, L. Hund's coupling and its key role in tuning multiorbital correlations. *Phys. Rev. B* **83**, 205112 (2011).

34. Georges, A., Medici, L. de' & Mravlje, J. Strong Correlations from Hund's Coupling. *Annu. Rev. Condens. Matter Phys.* **4**, 137–178 (2013).

35. de' Medici, L. Hund's Metals Explained. in *The Physics of Correlated insulators, Metals and Superconductors Modeling and Simulation* (ed. E. Pavarini, E. Koch, R. Scalettar, R. M.) (2017).

36. Haule, K. & Kotliar, G. Coherence–incoherence crossover in the normal state of iron oxypnictides and importance of Hund's rule coupling. *New J. Phys.* **11**, 025021 (2009).

37. Nakajima, M. *et al.* Normal-state charge dynamics in doped $BaFe_2As_2$: Roles of doping and necessary ingredients for superconductivity. *Sci. Rep.* **4**, 5873 (2015).

38. De Medici, L., Giovannetti, G. & Capone, M. Selective Mott physics as a key to iron superconductors. *Phys. Rev. Lett.* **112**, (2014).

39. Huang, J. *et al.* Correlation-driven electronic reconstruction in $FeTe_{1-x}Se_x$. *Commun. Phys.* **5**, 29 (2022).

40. Mazin, I. I., Singh, D. J., Johannes, M. D. & Du, M. H. Unconventional Superconductivity with a Sign Reversal in the Order Parameter of $LaFeAsO_{1-x}F_x$. *Phys. Rev. Lett.* **101**, 057003 (2008).

41. Dai, P., Hu, J. & Dagotto, E. Magnetism and its microscopic origin in iron-based high-temperature superconductors. *Nat. Phys.* **8**, 709–718 (2012).

42. Bascones, E., Valenzuela, B. & Calderón, M. J. Magnetic interactions in iron superconductors: A review. *Comptes Rendus Phys.* **17**, 36–59 (2016).

43. Fradkin, E., Kivelson, S. A., Lawler, M. J., Eisenstein, J. P. & Mackenzie, A. P. Nematic Fermi Fluids in Condensed Matter Physics. *Annu. Rev. Condens. Matter Phys.* **1**, 153–178 (2010).

44. Prozorov, R. *et al.* Intrinsic pinning on structural domains in underdoped single crystals of $Ba(Fe_{1-x}Co_x)_2As_2$. *Phys. Rev. B* **80**, 174517 (2009).

45. Chu, J.-H. *et al.* In-plane resistivity anisotropy in an underdoped iron arsenide superconductor. *Science* **329**, 824–826 (2010).

46. Ruff, J. P. C. *et al.* Susceptibility Anisotropy in an Iron Arsenide Superconductor Revealed by X-Ray Diffraction in Pulsed Magnetic Fields. *Phys. Rev. Lett.* **109**, 027004 (2012).

47. Chu, J.-H., Kuo, H.-H., Analytis, J. G. & Fisher, I. R. Divergent nematic susceptibility in an iron arsenide superconductor. *Science* **337**, 710–712 (2012).

48. Ikeda, M. S. *et al.* Elastocaloric signature of nematic fluctuations. *Proc. Natl. Acad. Sci.* **118**, (2021).

49. Böhmer, A. E. & Meingast, C. Electronic nematic susceptibility of iron-based superconductors. *Comptes Rendus Physique* **17**, 90–112 (2016).

50. Gallais, Y. & Paul, I. Charge nematicity and electronic Raman scattering in iron-based superconductors Nématicité de charge et diffusion Raman électronique dans les supraconducteurs au fer. *Physique* **17**, 113–139 (2016).

51. Kuo, H.-H., Chu, J.-H., Palmstrom, J. C., Kivelson, S. A. & Fisher, I. R. Ubiquitous signatures of nematic

quantum criticality in optimally doped Fe-based superconductors. *Science* **352**, 958–962 (2016).

52. Sanchez, J. J. *et al.* The transport–structural correspondence across the nematic phase transition probed by elasto X-ray diffraction. *Nat. Mater.* **20**, 1519–1524 (2021).

53. Sanchez, J. J., Malinowski, P., Kim, J.-W., Ryan, P. & Chu, J.-H. Quantitative relationship between structural orthorhombicity, shear modulus, and heat capacity anomaly of the nematic transition in iron-based superconductors. *Phys. Rev. B* **105**, 064513 (2022).

54. Shapiro, M. C., Hlobil, P., Hristov, A. T., Maharaj, A. V & Fisher, I. R. Symmetry constraints on the elastoresistivity tensor. *Phys. Rev. B* **92**, 235147 (2015).

55. Fernandes, R. M., Chubukov, A. V & Schmalian, J. What drives nematic order in iron-based superconductors? *Nat. Phys.* **10**, 97–104 (2014).

56. Fernandes, R. M., Orth, P. P. & Schmalian, J. Intertwined Vestigial Order in Quantum Materials: Nematicity and Beyond. *Annu. Rev. Condens. Matter Phys. is* **10**, 133–54 (2019).

57. Fernandes, R. M., Böhmer, A. E., Meingast, C. & Schmalian, J. Scaling between magnetic and lattice fluctuations in iron pnictide superconductors. *Phys. Rev. Lett.* **111**, (2013).

58. Hosoi, S. *et al.* Nematic quantum critical point without magnetism in $FeSe_{1-x}S_x$ superconductors. *Proc. Natl. Acad. Sci. U. S. A.* **113**, 8139–8143 (2016).

59. Auvray, N. *et al.* Nematic fluctuations in the cuprate superconductor $Bi_2Sr_2CaCu_2O_{8+\delta}$. *Nat. Commun.* **10**, 5209 (2019).

60. Sato, Y. *et al.* Thermodynamic evidence for a nematic phase transition at the onset of the pseudogap in $YBa_2Cu_3O_y$. *Nat. Phys.* **13**, 1074–1078 (2017).

61. Du, R. R. *et al.* Strongly anisotropic transport in higher two-dimensional Landau levels. *Solid State Commun.* **109**, 389–394 (1999).

62. Lilly, M. P., Cooper, K. B., Eisenstein, J. P., Pfeiffer, L. N. & West, K. W. Evidence for an Anisotropic State of Two-Dimensional Electrons in High Landau Levels. *Phys. Rev. Lett.* **82**, (1999).

63. Borzi, R. A. *et al.* Formation of a nematic fluid at high fields in $Sr_3Ru_2O_7$. *Science* **315**, 214–217 (2007).

64. Cao, Y. *et al.* Nematicity and competing orders in superconducting magic-angle graphene. *Science* **372**, 264–271 (2021).

65. Nie, L. *et al.* Charge-density-wave-driven electronic nematicity in a kagome superconductor. *Nature* **604**, 59 (2022).

66. Zhi-An, R. *et al.* Superconductivity at 55 K in Iron-Based F-Doped Layered Quaternary Compound

$Sm[O_{1-x}F_x]FeAs$. *Chinese Phys. Lett.* **25**, 2215 (2008).

67. Nandi, S. *et al.* Anomalous Suppression of the Orthorhombic Lattice Distortion in Superconducting $Ba(Fe_{1-x}Co_x)_2As_2$ Single Crystals. *Phys. Rev. Lett.* **104**, 057006 (2010).

68. Pratt, D. K. *et al.* Coexistence of competing antiferromagnetic and superconducting phases in the underdoped $Ba(Fe_{0.953}Co_{0.047})_2As_2$ compound using X-ray and neutron scattering techniques. *Phys. Rev. Lett.* **103**, (2009).

69. Ning, F. *et al.* 59 Co and 75 As NMR Investigation of Electron-Doped High T_c Superconductor $BaFe_{1.8}Co_{0.2}As_2$ (T_c = 22 K). *J. Phys. Soc. Japan* **77**, 103705 (2008).

70. Kuroki, K. *et al.* Unconventional Pairing Originating from the Disconnected Fermi Surfaces of Superconducting $LaFeAsO_{1-x}F_x$. *Phys. Rev. Lett.* **101**, 087004 (2008).

71. Wang, F. & Lee, D.-H. The Electron-Pairing Mechanism of Iron-Based Superconductors. *Science* **332**, (2011).

72. Kuroki, K. & Arita, R. Possible high- T_c superconductivity mediated by antiferromagnetic spin fluctuations in systems with Fermi surface pockets. *Phys. Rev. B* **64**, 024501 (2001).

73. Chubukov, A. Pairing Mechanism in Fe-Based Superconductors. *Annu. Rev. Condens. Matter Phys.* **3**, 57–92 (2012).

74. Korshunov, M. M., Togushova, Y. N. & Dolgov, O. V. Gap symmetry and structure of Fe-based superconductors. *Rep. Prog. Phys* **74**, 124508 (2011).

75. Inosov, D. S. *et al.* Normal-state spin dynamics and temperature-dependent spin-resonance energy in optimally doped $BaFe_{1.85}Co_{0.15}As_2$. *Nat. Phys.* **6**, 178–181 (2010).

76. Ning, F. L. *et al.* Contrasting Spin Dynamics between Underdoped and Overdoped $Ba(Fe_{1-x}Co_x)_2As_2$. *Phys. Rev. Lett.* **104**, (2010).

77. Tanatar, M. A. *et al.* Doping Dependence of Heat Transport in the Iron-Arsenide Superconductor $Ba(Fe_{1-x}Co_x)_2As_2$: From Isotropic to a Strongly k-Dependent Gap Structure. *Phys. Rev. Lett.* **104**, 067002 (2010).

78. Luan, L. *et al.* Local Measurement of the Superfluid Density in the Pnictide Superconductor $Ba(Fe_{1-x}Co_x)_2As_2$ Across the Superconducting Dome. *Phys. Rev. Lett.* **106**, 067001 (2011).

79. Reid, J.-P. *et al.* Nodes in the gap structure of the iron arsenide superconductor $Ba(Fe_{1-x}Co_x)_2As_2$ from c-axis heat transport measurements. *Phys. Rev. B* **82**, 064501 (2010).

80. Mu, G. *et al.* Evidence for line nodes in the energy gap of the overdoped $Ba(Fe_{1-x}Co_x)_2As_2$ from low temperature specific heat measurements. *Phys. Rev. B* **84**, 054505 (2011).

81. Terashima, K. *et al.* Fermi surface nesting induced strong pairing in iron-based superconductors. *Proc. Natl. Acad. Sci. U. S. A.* **106**, 7330–7333 (2009).

82. Mansart, B. *et al.* Opening of the superconducting gap in the hole pockets of $Ba(Fe_{1-x}Co_x)_2As_2$ as seen via angle-resolved photoelectron spectroscopy. *Phys. Rev. B* **85**, 144508 (2012).

83. Sachdev, S. & Keimer, B. Quantum criticality. *Phys. Today* **64**, 29 (2011).

84. Shibauchi, T., Carrington, A. & Matsuda, Y. A Quantum Critical Point Lying Beneath the Superconducting Dome in Iron Pnictides. *Annu. Rev. Condens. Matter Phys* **5**, 113–135 (2014).

85. Coleman, P. & Schofield, A. J. Quantum criticality. *Nature* **433**, 226–229 (2005).

86. Fernandes, R. M., Maiti, S., Wölfle, P. & Chubukov, A. V. How Many Quantum Phase Transitions Exist Inside the Superconducting Dome of the Iron Pnictides? *Phys. Rev. Lett.* **111**, 057001 (2013).

87. Shibauchi, T., Carrington, A. & Matsuda, Y. A Quantum Critical Point Lying Beneath the Superconducting Dome in Iron Pnictides. *Annu. Rev. Condens. Matter Phys* **5**, 113–135 (2014).

88. Shishido, H. *et al.* Evolution of the Fermi Surface of $BaFe_2(As_{1-x}P_x)_2$ on Entering the Superconducting Dome. *Phys. Rev. Lett.* **104**, 057008 (2010).

89. Walmsley, P. *et al.* Quasiparticle Mass Enhancement Close to the Quantum Critical Point in $BaFe_2(As_{1-x}P_x)_2$. *Phys. Rev. Lett.* **110**, 257002 (2013).

90. Moir, C. M. *et al.* Multi-band mass enhancement towards critical doping in a pnictide superconductor. *npj Quantum Mater.* **4**, 8 (2019).

91. Hashimoto, K. *et al.* A sharp peak of the zero-temperature penetration depth at optimal composition in $BaFe_2(As_{1-x}P_x)_2$. *Science* **336**, 1554–1557 (2012).

92. Grissonnanche, G. *et al.* Linear-in temperature resistivity from an isotropic Planckian scattering rate. *Nature* **595**, (2021).

93. Giraldo-Gallo, P. *et al.* Scale-invariant magnetoresistance in a cuprate superconductor. *Science* **361**, 479–481 (2018).

94. Ayres, J. *et al.* Incoherent transport across the strange-metal regime of overdoped cuprates. *Nature* **595**, 661 (2021).

95. Hayes, I. M. *et al.* Superconductivity and quantum criticality linked by the Hall effect in a strange metal. *Nat. Phys.* **17**, 58–62 (2021).

96. Kasahara, S. *et al.* Evolution from non-Fermi- to Fermi-liquid transport via isovalent doping in $BaFe_2(As_{1-x}P_x)_2$ superconductors. *Phys. Rev. B* **81**, 184519 (2010).

97. Lederer, S., Schattner, Y., Berg, E. & Kivelson, S. A. Enhancement of Superconductivity near a Nematic Quantum Critical Point. *Phys. Rev. Lett.* **114**, 097001 (2015).

98. Lederer, S., Schattner, Y., Berg, E. & Kivelson, S. A. Superconductivity and non-Fermi liquid behavior near a nematic quantum critical point. *Proc. Natl. Acad. Sci.* **114**, 4905–4910 (2017).

99. Paul, I. & Garst, M. Lattice Effects on Nematic Quantum Criticality in Metals. *Phys. Rev. Lett.* **118**, 227601 (2017).

100. Lax, M. *Symmetry Principles in Solid State and Molecular Physics*. (Dover Publications, Inc., 1974).

101. He, M. *et al.* Dichotomy between in-plane magnetic susceptibility and resistivity anisotropies in extremely strained $BaFe_2As_2$. *Nat. Commun.* **8**, 504 (2017).

102. Yi, M. *et al.* Symmetry-breaking orbital anisotropy observed for detwinned $Ba(Fe_{1-x}Co_x)_2As_2$ above the spin density wave transition. *Proc. Natl. Acad. Sci.* **108**, 6878–6883 (2011).

103. Sanchez, J. J. *et al.* Strongly anisotropic antiferromagnetic coupling in $EuFe_2As_2$ revealed by stress detwinning. *Phys. Rev. B* **104**, 104413 (2021).

104. Ikeda, M. S. *et al.* Symmetric and antisymmetric strain as continuous tuning parameters for electronic nematic order. *Phys. Rev. B* **98**, 245133 (2018).

105. Hristov, A. T., Ikeda, M. S., Palmstrom, J. C., Walmsley, P. & Fisher, I. R. Elastoresistive and elastocaloric anomalies at magnetic and electronic-nematic critical points. *Phys. Rev. B* **99**, 100101 (2019).

106. Worasaran, T. *et al.* Nematic quantum criticality in an Fe-based superconductor revealed by strain-tuning. *Science* **372**, 973–977 (2021).

107. Kissikov, T. *et al.* Uniaxial strain control of spin-polarization in multicomponent nematic order of $BaFe_2As_2$. *Nat. Commun.* **9**, 1058 (2018).

108. Cano, A. & Paul, I. Effect of uniaxial pressure on the magnetostructural transitions of iron arsenide superconductors. *Phys. Rev. B* **85**, 155133 (2012).

109. Sefat, A. S. *et al.* Superconductivity at 22 K in Co-doped $BaFe_2As_2$ crystals. *Phys. Rev. Lett.* **101**, (2008).

110. Chu, J.-H., Analytis, J. G., Kucharczyk, C. & Fisher, I. R. Determination of the phase diagram of the electron-doped superconductor $Ba(Fe_{1-x}Co_x)_2As_2$. *Phys. Rev. B* **79**, 014506 (2009).

111. Ni, N. *et al.* Effects of Co substitution on thermodynamic and transport properties and anisotropic H_{c2} in $Ba(Fe_{1-x}Co_x)_2As_2$ single crystals. *Phys. Rev. B* **78**, 214515 (2008).

112. Hicks, C. W., Barber, M. E., Edkins, S. D., Brodsky, D. O. & Mackenzie, A. P. Piezoelectric-based apparatus for strain tuning. *Rev. Sci. Instrum.* **85**, 065003 (2014).

113. Malinowski, P. *et al.* Suppression of superconductivity by anisotropic strain near a nematic quantum critical point. *Nat. Phys.* **16**, 1189–1193 (2020).

114. Fujii, C. *et al.* Anisotropic Grüneisen parameter and diverse order parameter fluctuations in iron-based superconductor $Ba(Fe_{1-x}Co_x)_2As_2$. *J. Phys. Soc. Japan* **87**, 074710 (2018).

115. Eckberg, C. *et al.* Sixfold enhancement of superconductivity in a tunable electronic nematic system. *Nat. Phys.* **16**, 346–350 (2020).

116. Hicks, C. W. *et al.* Strong increase of T_c of Sr_2RuO_4 under both tensile and compressive strain. *Science* **344**, 283–285 (2014).

117. Philippe, J.-C. *et al.* Nematic fluctuations mediated superconductivity revealed by anisotropic strain in $Ba(Fe_{1-x}Co_x)_2As_2$. *arXiv: 2204.12213* (2022). doi:10.48550/arxiv.2204.12213

118. Eckberg, C. *et al.* Sixfold enhancement of superconductivity in a tunable electronic nematic system. *Nat. Phys.* **16**, 346–350 (2020).

119. Konzen, L. M. N. & Sefat, A. S. Lattice parameters guide superconductivity in iron-arsenides. *J. Phys. Condens. Matter* **29**, 083001 (2017).

120. Meingast, C. *et al.* Thermal Expansion and Grüneisen Parameters of $Ba(Fe_{1-x}Co_x)_2As_2$: A Thermodynamic Quest for Quantum Criticality. *Phys. Rev. Lett.* **108**, 177004 (2012).

121. Kimber, S. A. J. *et al.* Similarities between structural distortions under pressure and chemical doping in superconducting $BaFe_2As_2$. *Nat. Mater.* **8**, 471–475 (2009).

122. Chen, X., Dai, P., Feng, D., Xiang, T. & Zhang, F.-C. Iron-based high transition temperature superconductors. *Natl. Sci. Rev.* **1**, 371–395 (2014).

123. Drotziger, S. *et al.* Pressure versus Concentration Tuning of the Superconductivity in $Ba(Fe_{1-x}Co_x)_2As_2$. *J. Phys. Soc. Japan* **79**, 124705 (2010).

124. Klintberg, L. E. *et al.* Chemical pressure and physical pressure in $BaFe_2(As_{1-x}P_x)_2$. *J. Phys. Soc. Japan* **79**, 1–4 (2010).

125. Kang, J. H. *et al.* Superconductivity in undoped $BaFe_2As_2$ by tetrahedral geometry design. *Proc. Natl. Acad. Sci.* **117**, 21170–21174 (2020).

126. Drotziger, S. *et al.* Pressure versus concentration tuning of the superconductivity in $Ba(Fe_{1-x}Co_x)_2As_2$. *J. Phys. Soc. Japan* **79**, (2010).

127. Nagaosa, N., Sinova, J., Onoda, S., MacDonald, A. H. & Ong, N. P. Anomalous Hall effect. *Rev. Mod. Phys.* **82**, 1539–1592 (2010).

128. Palmstrom, J. C. *et al.* Comparison of temperature and doping dependence of elastoresistivity near a putative nematic quantum critical point. *Nat. Commun.* **13**, 1011 (2022).

129. Jiang, Q. *et al.* Nematic fluctuations in an orbital selective superconductor $Fe_{1+y}Te_{1-x}Se_x$. *arXiv:2006.15887* (2020).

130. Ishida, K. *et al.* Novel electronic nematicity in heavily hole-doped iron pnictide superconductors. *Proc. Natl. Acad. Sci.* **117**, 6424–6429 (2020).

131. Brouet, V. *et al.* Large Temperature Dependence of the Number of Carriers in Co-Doped $BaFe_2As_2$. *Phys. Rev. Lett.* **110**, 167002 (2013).

132. Rullier-Albenque, F., Colson, D., Forget, A. & Alloul, H. Hall effect and resistivity study of the magnetic transition, carrier content, and fermi-liquid behavior in $Ba(Fe_{1-x}Co_x)_2As_2$. *Phys. Rev. Lett.* **103**, 057001 (2009).

133. Hadzic-Leroux, M. *et al.* Hall Effect in Heavy-Fermion Systems. *Europhys. Lett.* **1**, 579–584 (1986).

134. Balakirev, F. F. *et al.* Signature of optimal doping in Hall-effect measurements on a high-temperature superconductor. *Nature* **424**, 912–915 (2003).

135. Palmstrom, J. C., Hristov, A. T., Kivelson, S. A., Chu, J.-H. & Fisher, I. R. Critical divergence of the symmetric (A_{1g}) nonlinear elastoresistance near the nematic transition in an iron-based superconductor. *Phys. Rev. B* **96**, 205133 (2017).

136. Palmstrom, J. C., Hristov, A. T., Kivelson, S. A., Chu, J. H. & Fisher, I. R. Critical divergence of the symmetric (A1g) nonlinear elastoresistance near the nematic transition in an iron-based superconductor. *Phys. Rev. B* **96**, (2017).

137. Breitkreiz, M., Brydon, P. M. R. & Timm, C. Transport in multiband systems with hot spots on the Fermi surface: Forward-scattering corrections. *Phys. Rev. B* **89**, 245106 (2014).

138. Fanfarillo, L., Cappelluti, E., Castellani, C. & Benfatto, L. Unconventional hall effect in pnictides from interband interactions. *Phys. Rev. Lett.* **109**, (2012).

139. Breitkreiz, M., Brydon, P. M. R. & Timm, C. Transport anomalies due to anisotropic interband scattering. *Phys. Rev. B* **88**, 85103 (2013).

140. Kissikov, T. *et al.* Uniaxial strain control of spin-polarization in multicomponent nematic order of $BaFe_2As_2$. *Nat. Commun.* **9**, 1058 (2018).

141. Kapitulnik, A., Kivelson, S. A. & Spivak, B. Colloquium: Anomalous metals: Failed superconductors. *Rev. Mod. Phys.* **91**, 011002 (2019).